Final Reports

DoE Award No: DE-FE00028992

Engineering Metal Oxide Nanomaterials for Fiber Optical Sensor Platforms

Submitted
December 13, 2020

PI: Kevin P. Chen, email: pec9@pitt.edu, telephone: 412-624-9675, fax: 412-624-8003
Department of Electrical and Computer Engineering
University of Pittsburgh
1238 Benedum Hall, 3700 O'Hara Street
Pittsburgh, PA 15261

Project Period: 10/1/2016-9/30/2020
Report Submission Date: 12/13/2020

This report is submitted by Principal Investigator: Kevin P. Chen

Signature of Submitting Official: _____

Name of Submitting Official: Kevin P. Chen

Objectives

In this research program, the recipient will explore nano-engineered metal oxides, a class of important sensory materials, for fiber optic chemical sensing for high-temperature energy applications using both silica and sapphire fibers as sensing platforms.

Objective I: A scalable nanofabrication method will be developed to engineer refractive indices, surface areas, and chemical specificities of a wide range of transition metal oxides and their dopant variants for fiber optical chemical sensing in high temperatures (400-900ºC).

Objective II: Functional metal oxide sensory materials with proper refractive indices and chemical sensitivities will be integrated on both silica fiber and sapphire fiber platforms. Their responsivities to various fuel gas and fuel gas mixtures will be thoroughly studied in high temperatures (400-900ºC).

Objective III: Using distributed fiber sensing schemes such as Rayleigh backscattering Optical Frequency Domain Reflectometry (R-OFDR) or fiber Bragg grating (FBG) arrays, the recipient will develop a unique distributed fiber optical chemical sensing technique to probe energy chemistry at high temperatures with high spatial resolution of 1-cm or better (e.g. H_2 consumption profiles in fuel cells). Using the same distributed fiber sensing scheme, various metal oxides will be integrated on one fiber for real-time multi-species gas measurements in high temperatures (400-900ºC).

This final report documents allproject accomplishments with the project goals and objectives listed above for the reporting period.

Summary of Accomplishments

This project has generated siginficant amounts of scientific knowledge and intellectual properties. These include four US patents (two awarded and two in the final stage of litigation) This grant also support research works disseminated through 10 journal papers published in top scientific journals and over 20 referred conference papers.

Patents Supported by this grant

1. Kevin Peng Chen, Zsolt Poole, Michael Buric, and Paul Ohodnicki, "**Fiber optical sensors employing a metal oxide material**", US Patent 10,457,596 (2019).
2. Kevin Peng Chen, Aidong Yan, Michael Buric, and Paul Ohodnicki, "**Method of making a distributed optical fiber sensor having enhanced Rayleigh scattering and enhanced temperature stability and monitoring systems employing same**," US Patent 10,670,802 (2020).
3. (Pending) Kevin Peng Chen, Zsolt Poole, Michael Buric, and Paul Ohodnicki, "**Fiber optical sensors employing a metal oxide material**", US Patent pending Continue-in-Part (2020).
4. (Pending) Kevin Peng Chen, Aidong Yan, Michael Buric, and Paul Ohodnicki, "**Method of making a distributed optical fiber sensor having enhanced Rayleigh scattering and enhanced temperature stability and monitoring systems employing same**," US Divisional Patent Application 16/807.232 (2020).

Journal papers supported by this grant

1. M. A. S. Zaghloul, J. H. Mason, M. Wang, M. Buric, Z. Peng, S. Lee, P. R. Ohodnicki, H. Abernathy, and K. P. Chen, "**High Spatial Resolution Temperature Profile Measurements of Solid-Oxide Fuel Cells**," Applied Energy, under 2nd review (2020).
2. Y. Yang, M. Wang, Z. Yu, Q. Yu, and K. P. Chen, "**Multiplexable intrinsic Fabry-Pérot interferometers inscribed by femtosecond laser for vibration measurement in high temperature environments**," Sensor and Actuator A, to be published.
3. R. Cao, H. Ding, K.-J. Kim, Z. Peng, J. Wu, J. T. Culp, P. R. Ohodnicki, E. Beckman, and K. P. Chen, "**Metal-organic Framework Functionalized Polymer Coating for Fiber Optical Methane Sensors**," Sensor and Actuator B, DOI: 10.1016/j.snb.2020.128627 (2020).
4. M. Wang, Y. Yang, S. Huang, J. Wu, K. Zhao, Y. Li, Z. Peng, R. Zou, H. Lan, P. R. Ohodnicki, P. Lu, M. P. Buric, B. Liu, Q. Yu, and K. P. Chen, "**Multiplexable high-temperature stable and low-loss intrinsic Fabry-Perot in-fiber sensors through nanograting engineering**," Opt. Express 28, 20225-20235 (2020).
5. Y. Yang, J. Wu, M. Wang, Q. Wang, Q. X. Yu, and K. P. Chen, "**Fast demodulation of fiber Bragg grating wavelength from low-resolution spectral measurements using Buneman Frequency Estimation**," Journal of Lightwave Technology, DOI: 10.1109/JLT.2020.2998614 (2020).
6. M. Wang, K. Zhao, S. Huang, J. Wu, P. Lu, P. R. Ohodnicki, M.-J. Li, S. J. Mihailov, and K. P. Chen, "**Reel-to-Reel Fabrication of In-fiber Low-Loss and High-Temperature Stable Rayleigh**

Scattering Centers for Distributed Sensing," IEEE Sensor Journal, DOI: 10.1109/JSEN.2020.2995606 (2020).

7. R. Cao, Y. Yang, M. Wang, X. Yi, J. Wu, S. Huang, and K. P. Chen, "**Multiplexable Intrinsic Fabry-Perot Interferometric Fiber Sensors for Multipoint Hydrogen Gas Monitoring,**" Opt. Lett., vol. 45, 11, pp. 3163-63 (2020).

8. R. Cao, J. Wu, G. Liang, P. R. Ohodnicki and K. P. Chen, "**Functionalized PdAu Alloy on Nanocones Fabricated on Optical Fibers for Hydrogen Sensing**," in IEEE Sensors Journal. (2019) doi: 10.1109/JSEN.2019.2950505

9. A. Yan, S. Huang, S. Li, R. Chen, P. Ohodnicki, M. Buric, S. Lee, M-J. Li, and K. P. Chen, "**Distributed Optical Fiber Sensors with Ultrafast Laser Enhanced Rayleigh Backscattering Profiles for Real-time Monitoring of Solid Oxide Fuel Cell Operations**," Scientific Reports, DOI: 10.1038/s41598-017-09934-3, (2017).

Detailed Technical Reports:

Distributed fiber optic sensing is a potentially powerful technique to measure the spatial temperature profile of an operating SOFC system. Being well-suited for harsh environment sensing applications, fiber optic sensors have been widely used for high-temperature measurements. Distributed sensing schemes such as Rayleigh-scattering Optical Frequency Domain Reflectometry (OFDR) can perform distributed temperature sensing using unmodified single-mode optical fiber to achieve <1-cm spatial resolution. One of the key challenges of distributed sensing using the Rayleigh backscattering is the weak Rayleigh-backscattering intensity exhibited by conventional optical fibers. The weak Rayleigh backscattering is hardly a surprise, given that telecommunications optical fibers are designed for low-losses, including low Rayleigh-scattering losses. To address this challenge, several approaches have been attempted to increase Rayleigh scattering in single-mode fibers[6,7]. The enhanced Rayleigh scattering profiles result in larger scattering signals at the detector(s) and better spectral correlation quality between the measured high-temperature Rayleigh profile and the reference room-temperature Rayleigh profile. This in turn improves the fidelity of the distributed measurement as well as the useful range of temperatures over which the sensor-fiber can operate effectively. However, even though Rayleigh scattering enhancement may be used to effectively extend the operational temperature and fiber longevity, eventually environmental effects will overcome the stability of the measurement during extended periods of high-temperature operation (>700ºC). At the highest operating temperatures, the same fiber core structural non-uniformities that give rise to the intrinsic Rayleigh scattering undergoes permanent changes[8]. These changes will eventually compromise sensitivity and reliability of the distributed measurements, although the use of the types of scattering enhancement modifications described here may delay or mitigate the effects of such degradation, yielding a new regime of measurement capability.

In this project, we propose to use femtosecond ultrafast laser irradiation to produce enhanced Rayleigh scattering profiles in optical fibers that are stable at high temperatures. The ultrafast laser is known to be a useful tool to produce fiber Bragg grating (FBG) point-sensors with superior temperature stability compared to FBGs produced by UV lasers[9]. In contrast to the laser-fabrication of Bragg gratings, this paper presents a far simpler manufacturing scheme to produce distributed fiber sensors using 300–nJ laser pulses. The resultant enhanced fibers can perform distributed temperature sensing with 5-mm spatial resolution at 800ºC in highly reactive fuel gas (hydrogen) stream. Using this powerful sensing tool, we demonstrate distributed temperature measurement in an operating SOFC-system. Information gathered by this fiber sensor tool can now be compared with simulation results to aid in SOFC system design, and ultimately improve the operational efficiency and longevity of the SOFC system.

Experiments and Results

To enhance the Rayleigh backscattering profile in optical fibers, a Coherent femtosecond laser system is used to irradiate optical fiber. The ultrafast laser system consists of a Coherent MIRA-D Ti:sapphire seed oscillator and a RegA 9000 regenerative amplifier operated at 800 nm with a repetition rate of 250 kHz. The pulse width was adjusted to 300-fs. The schematic of the experimental setup is presented in Fig. 1. The laser beam from the RegA9000 is spatially shaped by a pair of cylindrical lenses before being focused into the fiber core using an 80× microscope objective. The fiber being irradiated is also connected to a commercial OFDR interrogator

(LUNA OBR4600). The Rayleigh backscattering profiles were monitored by the interrogator during the laser irradiation process. The optical fiber-samples were mounted on a computer-controlled air-bearing motion stage (AEROTECH ABL2002). The laser was operated with a continuous pulse-train while the fiber was translated over 20-cm longitudinally. The backscattering profile was optimized by varying the translation speed of the motion stage from 0.1 mm/s to 1 mm/s.

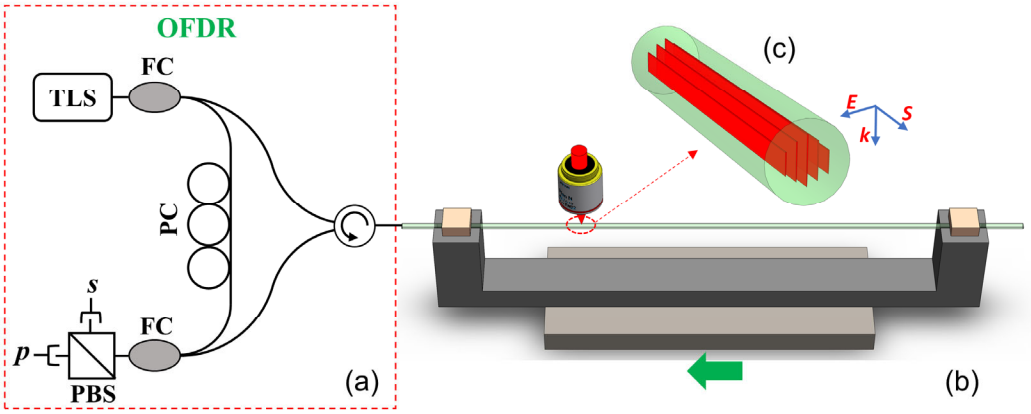

Figure 1. Schematic sketch of the Rayleigh Enhancement setup. (a) OFDR system (LUNA OBR 4600 with internal components [10]: TLS: tunable laser source, FC: Fiber Coupler PC: polarization controller, PBS: polarizing beam splitter). (b) Schematic sketch of the ultrafast laser irradiation on optical fibers. (c) Nanograting formed in fiber core during laser irradiation with S: The direction of laser scanning, E: The direction of the electrical field. *k*: nanograting orientation and the direction of light propagation.

Fig. 2 shows the enhanced Rayleigh backscattering profiles produced in 17-cm long sections of fiber using the ultrafast laser direct writing scheme. The on-target pulse energy was set at 300-nJ, which was determined to be slightly above the threshold pulse energy required to enhance the Rayleigh backscattering. The fiber translation speeds were 0.1 mm/s (Fig. 2a), 0.5 mm/s (Fig. 2b), and 1mm/s (Fig. 2c), respectively. An increase in the Rayleigh backscattering amplitude of 40-45 dB was obtained with laser irradiation for all of the chosen writing speeds. The ultrafast laser irradiation did not yield Rayleigh scattering enhancements when the laser writing speed exceeded 2 mm/s. The laser irradiation also introduced significant optical propagation losses in the irradiated fiber-samples; which is characterized by the slope of the Rayleigh-enhanced region. At 300-nJ pulse energy, the average propagation losses in the irradiation sections are 0.41 dB/cm, 0.30 dB/cm and 0.15 dB/cm, respectively. Therefore, a scanning speed of 1mm/s was the optimal processing condition that minimized the insertion loss of the irradiated sensor-segment.

After testing, the irradiated sensor segments were cleaved and imaged using a Scanning Electron Microscope (SEM - Zeiss Sigma 500 VP). This observation reveals the telltale signs of the mechanism behind the laser-induced Rayleigh enhancements. Fig. 2(d)-(f) show the SEM cross-section images of the fiber core regions after the laser irradiation was performed at scanning speeds of 0.1 mm/s, 0.5 mm/s, and 1 mm/s, respectively. It is clear that the ultrafast laser enhancement of the Rayleigh profile is closely linked to the formation of laser-induced nano-gratings inside the fiber core. These nanogratings were only observed in fibers which exhibited enhanced Rayleigh back-scattering after processing. As previous researchers have reported, the volume of laser-induced nanogratings in silica depends on the number of

laser pulses and the total pulse energy deposited into the focal volume [11,12]. This is also confirmed in Fig. 2(d)-(f) with slower fiber translation speed leading to larger nanograting volumes at the same pulse-repetition rate and energy. Periodicities of the nanogratings are measured to be around 500 nm (Fig. 2d) or 250 nm (Fig. 2e-f), which is consistent with wavelength (500-nm) or half wavelength (250-nm) of the ultrafast laser in silica [11,13-15]. The height and width of the nanogratings depends on the laser energy deposited into the focal volume, which is also determined by the laser scanning speed. The width of the nanograting plane is measured to be less than 10 nm, and the length is approximately 4 μm at 0.1 mm/s fiber translation speed. The length of the grating is reduced to less than 1 μm with the scanning speed of 1 mm/s. It appears that the volume of the induced nanograting is directly correlated with the increase in propagation loss shown in Fig. 2.

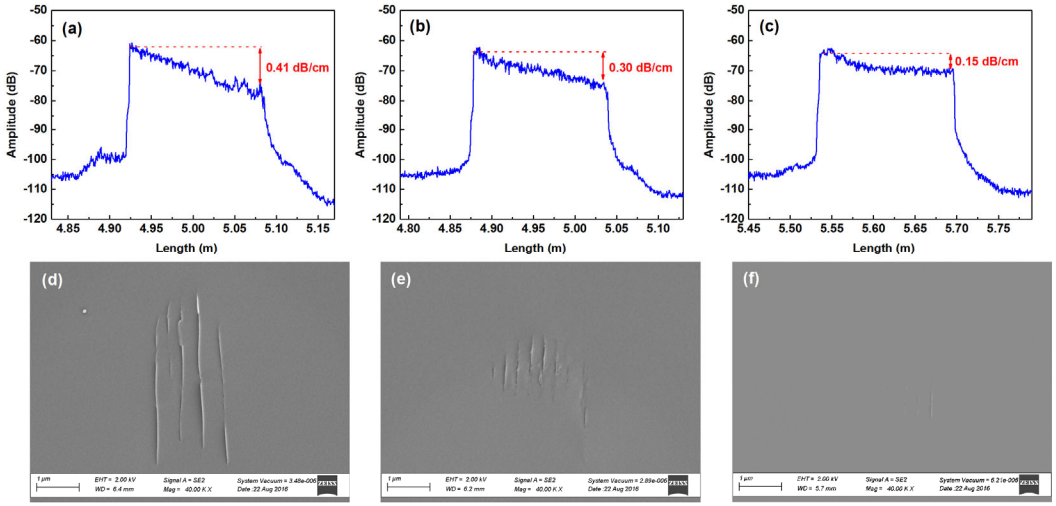

Figure 2. Laser-induced Rayleigh scattering enhancement and the formation of nanogratings. (a)-(c) Ultrafast laser-enhanced Rayleigh backscattering profiles and (d)-(f) scanning electron microscope (SEM) images of the cross-sectional morphologies of nanogratings formed at scanning speed of 0.1 mm/s, 0.5 mm/s and 1 mm/s, respectively.

To determine the thermal stability of the laser-enhanced Rayleigh scattering profiles at high temperatures in highly reactive fuel gas environments, the laser irradiated fibers were first annealed in a tube furnace at 800ºC. The tube furnace is flushed with H_2 balanced with N_2. Two calibrated mass flow controllers were used to control the concentrations of H_2 up to 10% in the gas mixture. During the annealing process, the temperature of the furnace was first ramped up from room temperature to 800ºC in air and held at temperature for 4 hours before switching to 10% H_2. The Rayleigh backscattering profile was monitored to determine the fiber sensor resilience while 10% H_2 was applied for 4 hours before switching back to air. The scattering profiles measured during the testing are presented in Fig. 3(a). The initial annealing process in N_2 at 800ºC yielded only a small decrease in the Rayleigh scattering profile. The small initial scattering decrease stabilizes in the first 10 minutes of annealing. The subsequent exposure to 10% H_2 did produce a small variation in the induced scattering which increased the intensity nearest the down-stream end of the irradiated section. This change is permanent in both 10% H_2 and N_2 atmosphere as shown in Figure 3(a). Since this scattering-increase occurs at latter portion of the laser irradiated section, this lowers the propagation loss in the fiber from 0.14 dB/cm to less than 0.1 dB/cm. The scattering increase in hydrogen can only happen rapidly when temperature is higher than 700ºC. This process occurs quickly, and the profile stabilized within 10 minutes of the application of H_2. When

switching back to nitrogen or air after annealing in H_2, no significant change in scattering was observed as shown in Fig. 3(a); indicating that the increase of scattering due to hydrogen at high temperatures is permanent.

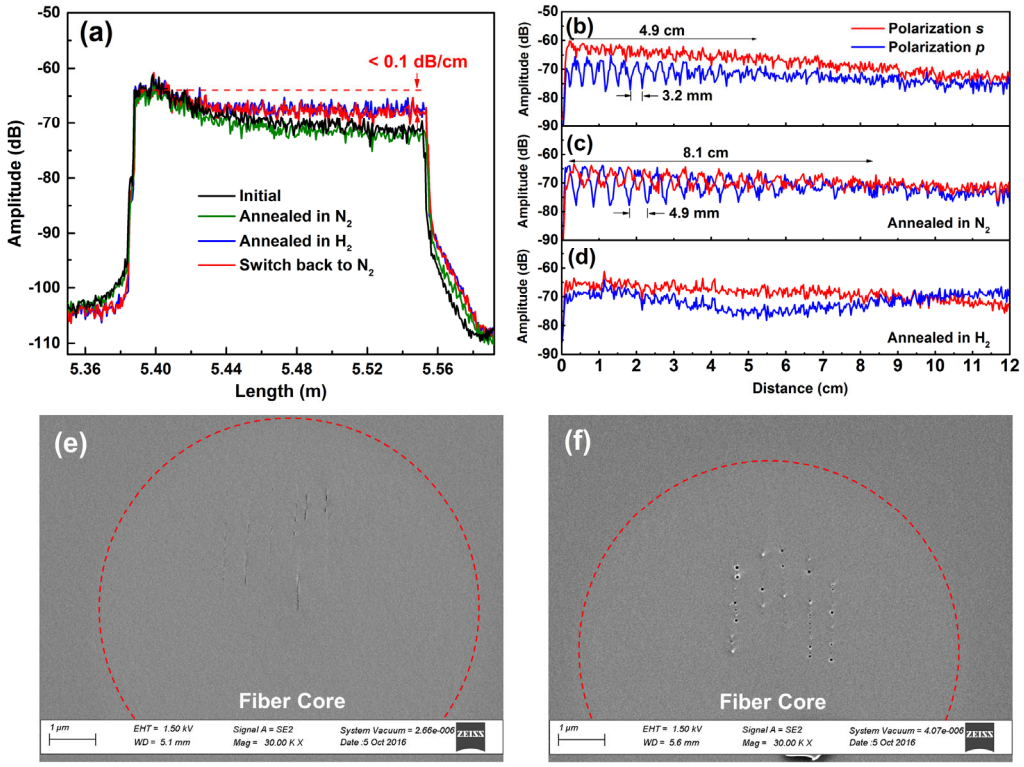

Figure 3: Anneal process at 800°C in N_2 and 10% H_2. (a) Rayleigh scattering amplitude measured during annealing in N_2, and 10% H_2 (balanced with 90% N_2), (b)-(d) scattering signal amplitude of the s and p polarization states emitted by the irradiated fiber before and after high temperature annealing in N_2 and 10% H_2 respectively, (e)-(f) SEM images of nanogratings morphology changes occurring after annealing in N_2 and 10% H_2, respectively.

In this work, the birefringence of the irradiated fibers was measured and correlated to the thermal annealing process using the OFDR instrument in order to shed light on stability of the laser-induced Rayleigh scattering and its degradation mechanisms. Given that nanogratings formed in the fiber cores are structurally asymmetric, they induce birefringence in negative uniaxial structures[15,16]. The slow and fast optical axes of the induced gratings were aligned parallel and perpendicular to the nanoplanes, respectively [17]. Figure 3(b)-(d) shows the Rayleigh backscattering signal demodulated into *s*- and *p*-polarizations by the OFDRs internal polarizing beam splitter. [18]. The irradiated fiber produces scattering along both the fast and the slow axes of the fiber, which is not necessarily aligned with polarization states demodulated by the polarizing beam splitter in the OFDR instrument. This results in birefringence beating as shown in Figure 3(b)-(d) for both *s*- and *p*- polarization states. The fading of the beating fringes over the length of the irradiated section is caused by diminishing coherence of the two polarization modes as the spatial difference between the two modes exceeds the resolution limit of the instrument[18]. The effective beating length of 3.2 mm was measured for the irradiated fiber at the laser scanning speed of 1mm/s as shown in Figure 3(b) at 1.5-μm wavelength. The magnitude of the effective index difference (i.e. modal birefringence Δn) can be quantified by $\Delta n = \lambda / L_b = 4.8 \times 10^{-4}$, which

agrees with birefringence in type II-IR gratings fabricated by ultrafast lasers in silica[19]. After annealing at 800ºC in N_2 for 4 hours, the beating length increased and settled to 4.9 mm. This corresponds to a slight reduction of the modal birefringence to 3.2×10^{-4} as shown in Figure 3(c). In sharp contrast, exposure in 10% H_2 at 800ºC quickly reduced the birefringence to $<10^{-6}$ as shown in Fig. 3(d). To determine the origin of this decay in birefringence, SEM photos of the nanogratings in samples annealed in air and H_2 are reported in Fig. 3(e) and (f). As shown in Fig. 3(e), part of the nanoplanes has morphed into several discontinuous shorter segments after annealing in air, which results in a slight decrease in the birefringence. However, for the fiber samples annealed with hydrogen, the nanograting planes evolve into a series of nanopores with diameters less than 50 nm. A possible reason for this pore formation is that the nanograting features in silica are more likely to be densified during exposure to hydrogen at high temperatures[20]. As a result, birefringence from the nanogratings was almost erased after hydrogen exposure.

Application of Robust Distributed Sensor for High-T Environments

To further characterize the induced Rayleigh scattering stability, the annealed fibers were used as temperature sensors over a wide range of applied temperatures. Temperature changes are measured by the OFDR system by cross-correlating the Rayleigh backscattering profile at a known temperature with the Rayleigh backscattering profile after heating. This cross correlation yields a spectral shift value plotted over the length of the test-section which may be further fitted to the temperature using a calibration curve intrinsic to the fiber material. After the initial thermal annealing in 10% hydrogen at 800ºC for 10 minutes, the Rayleigh scattering enhancement becomes significantly more stable. Figure 4(a) shows the scattering profiles measured using the annealed fibers from 24ºC to 800ºC in a 10% H_2 atmosphere. No significant scattering amplitude changes were observed as compared to the post-annealed fiber.

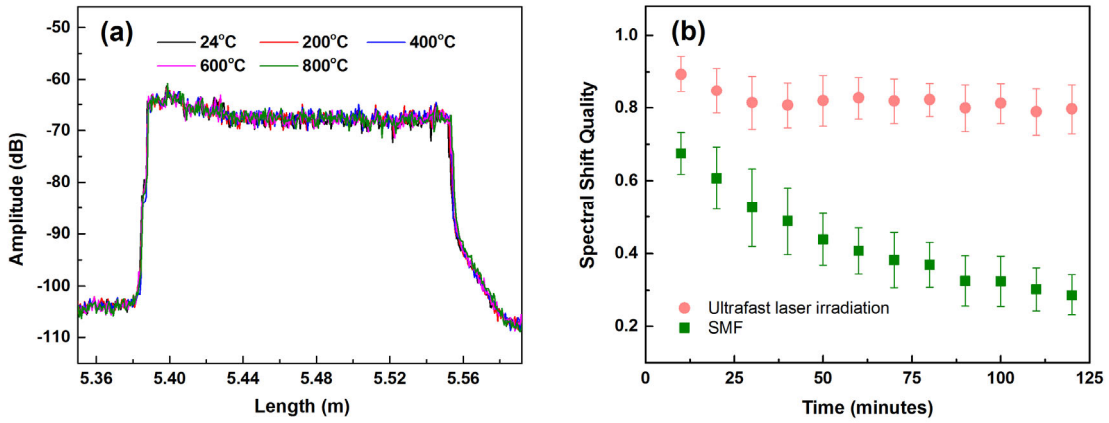

Figure 4: Thermal stability of laser-induced Rayleigh scatter. (a) Thermal stability of scattering features after an annealing process in 10% hydrogen at 800ºC for 10 minutes and (b) comparison of the spectral shift quality vs time at 800ºC for fiber irradiated by the ultrafast laser and un-irradiated standard fiber.

Fig. 4(b) shows the comparison of the spectral shift quality between the laser-irradiated fiber and a normal single-mode fiber (Corning SMF-28) at 800ºC. The spectral shift quality is a measure of the strength of correlation between the backscattering profiles in measurement and reference spectra. The parameter is defined as the maximum value of cross-correlation between the measurement and reference

spectra normalized by the maximum of the reference spectrum autocorrelation. The reference spectrum was recorded at 800ºC. A spectral shift quality of 1.0 indicates that there is a perfect match between reference and measurement spectra. The shift quality will decrease when the scattering signal becomes significantly different from the reference signal. Results shows that the spectral shift quality at T = 800ºC under 10% hydrogen decreased from 1 to less than 0.3 within 2 hours for Corning SMF-28 fiber, while the spectral shift quality in the fiber with the enhanced scattering profile remained above 0.8 for the same time period. When the irradiated fiber was tested more than 20 hours under the same conditions, the value of the spectral shift quality remained above 0.75. This result shows that distributed temperature measurement can be performed with high fidelity at high temperature over a long period of time; even in a highly reactive hydrogen environment.

The temperature dependence of the spectral shift in the irradiated fiber was characterized over the temperature range from 24ºC to 800ºC. Fig. 5(a) shows the spectral shift versus temperature change for the ultrafast laser-irradiated fiber. There appears to be a change in slope at approximately T = 300ºC. Two linear temperature/spectral shift coefficients are obtained in those two respective temperature regimes. Between 23ºC and 300ºC, the temperature change linearly depends on the spectral shift with a slope of $-\partial T/\partial \nu \sim 0.6697$ ºC/GHz. While above 300ºC, the coefficient changes to ~ 0.5264 ºC/GHz. This thermal-optic coefficient change is caused by the phase transition change in silica around 300ºC [21]. The formation of nanogratings also results in a significant increase in the spectral-shift quality for distributed temperature measurement over a wide temperature range. This is shown in the inset of Fig. 5(a). When the Rayleigh profile at 23ºC was taken as the reference, and the temperature was then increased to 800ºC; the spectral shift quality remained above 0.3, which is significantly higher than the threshold spectral-shift quality required for reliable temperature measurement (0.15).

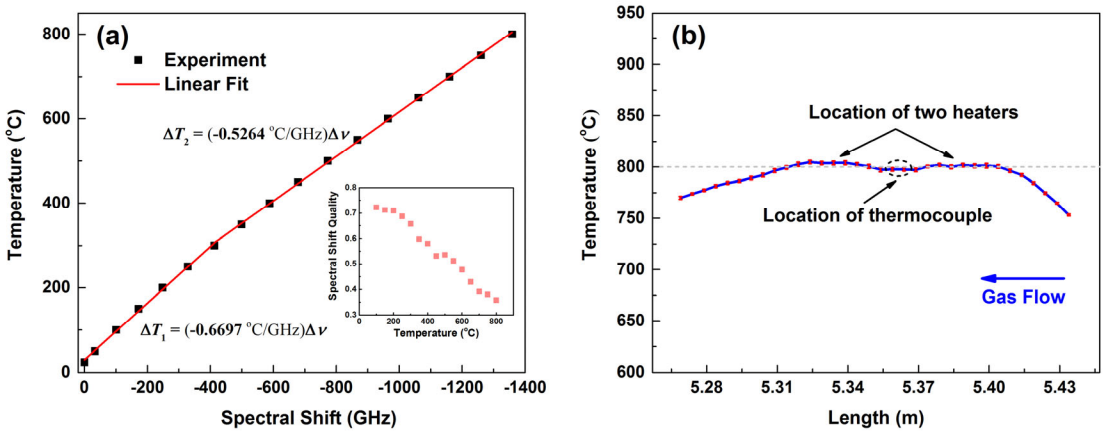

Figure 5: (a) Rayleigh spectral shift measured by OFDR at different applied temperatures for fibers with enhanced Rayleigh scattering profile. The inset shows the spectral shift quality vs. temperature. (b) Temperature profile of a furnace measured by the distributed fiber sensors with enhanced Rayleigh scattering profile. The furnace temperature was set at 800ºC. The error bar was obtained by 8 different measurements for each with a cooling cycle to room temperature.

To study the reliability of temperature measurements over a wide range, the Rayleigh enhanced irradiated fiber was tested using a tube furnace. Fig. 5(b) shows the temperature measurement repeatability using Rayleigh-enhanced fiber. The furnace temperature was monitored and controlled by a single thermocouple placed in the center section of the furnace as denoted in the figure. The furnace was

heated up by two heaters, which were placed 3.5-cm from the thermocouple location on either side of the center of the furnace. The spatially resolved temperature profile of the furnace at the set temperature of 800ºC is shown in Fig. 5(b) with a spatial resolution of 0.5 cm. The reference spectra was taken at 23ºC at the beginning of the measurements. Eight separate measurements were taken. After each measurement, the furnace was cooled to room temperature and reheated to 800ºC for subsequent measurement. The error bars presented in Fig. 5(b) show a standard deviation less than 4ºC, which highlights the measurement reliability. The measurement also reveals that the heater locations have slightly higher temperatures than the location of thermocouple which was regulating the temperature. In the experiment, 20 sccm of 10% hydrogen flows from one side of the furnace's quartz tube to the other. As a result of the high thermal conductivity of hydrogen gas, larger temperature gradients were observed from the gas injection side (right side in the figure). These fine details of the temperature profile revealed by the distributed fiber sensors highlight the excellent temperature measurement capability which is useful for both the design and control of energy systems.

Fuel Cell Test: The thermally-stable distributed fiber-optic sensors demonstrated in this paper provide a powerful tool to perform in-vivo measurements and to understand the operation of high-temperature SOFCs. The fuel cell tests described here were performed at the U.S. Department of Energy's National Energy Technology Laboratory fuel-cell testing facility (Morgantown, WV). This test-facility was designed for assessing the performance of kw-level SOFC distributed power generation systems. A single commercial planar fuel cell (ASC5, Fuel Cell Materials, Lewis Center, OH) was used for the test. This type of anode-supported fuel cell has a yttria-stabilized zirconia (YSZ) electrolyte, a Ni-YSZ anode, and a $La_{1-x}Sr_xCo_{1-y}Fe_yO_{3-d}$ (LSCF) cathode. The anode support is 5 cm x 5 cm, and the cathode active area is 4 cm x 4 cm.

Figure 6(a)-(b) shows the photograph and schematic of the SOFC in a counter-flow configuration. Hydrogen fuel flows from the inlet to the outlet across a series of parallel fuel channels, while air flows in parallel channels in the opposite direction on the other side of the cell. The distance from the inlet to outlet is 8 cm and the length of the electrolyte region is 5 cm. In order to probe the temperature change at different electric loads, fiber sensors were placed in the anode channel and cathode channel respectively, as shown in Figure 6(a) and (b). Before installing fiber sensors, the fuel cell assembly was heated up to 860ºC to form a gas-tight seal using glass-ceramic sealant. The completed cell was then aged at 750ºC for 6 h to reduce the anode material under 100% H_2. After checking the normality of fuel cell operation, the assembly was brought down to room temperature and fiber sensors were inserted into the cell through nickel tubes which provided access to the cell-body and encased the fiber-sensor outside the cell-body. Both ends of the tubes positioned outside of the furnace were sealed with silicone putty where the fiber entered or exited the assembly. Prior to the operation, the sensor-embedded fuel cell was heated externally to ~ 720ºC, which is confirmed by both point thermocouple devices and the distributed fiber sensors. The distributed temperature profile of the cell was continuously monitored and compared with the reference during heating. Once the SOFC reached operational temperature, 500 sccm of 100% hydrogen was injected into the anode and 500 sccm of air was also injected into the cathode. When pure hydrogen was introduced at the anode, the temperature around the fuel gas inlet increased dramatically as shown in Figure 6(c)-(f). At the anode side, the temperature around the fuel inlet increase up to 55ºC above ambient. The temperature peaks near the border area of the electrolyte area. This is caused primarily by high thermal conductivity of hydrogen fuel. The electrolyte has significant influence on the temperature profile on the cathode side, where the temperature rise was much lower at about 25ºC. The temperature variation induced under different electric loads was also measured with load-current ranging from 0 A to 3 A. The current loading resulted in a slight temperature increase near the center section of

the fuel cell. At a 3-A current, the temperature increase on both anode and cathode sides was about 5ºC. While this reaction-induced temperature profile change might not be a significant issue for a single SOFC operating with external applied heating, the cumulative induced temperature effects on stacked self-heated fuel cell assemblies should be carefully studied. The fuel-gas induced temperature changes inside the fuel cell depend strongly on the flow rate of hydrogen and its concentration. We note anecdotally that a mixture of 4% H_2 does not exhibit significant convective heating effects on the SOFC assembly, while a 10% mixture induces readily observable convective effects. Given that the convective impacts of fuel gas streams on temperature profiles at the anode and cathode are significantly different, designing and implementing an optimal temperature control scheme will require modelling of the thermal characteristics of the SOFC assembly, along with the thermal and chemical properties of the cell materials and applied gases. The distributed fiber sensor demonstrated in this paper provides a new and valuable tool to measure the constantly-evolving SOFC temperature profile, which will lead us towards optimizing the efficiency and longevity of SOFC-based energy systems in the future.

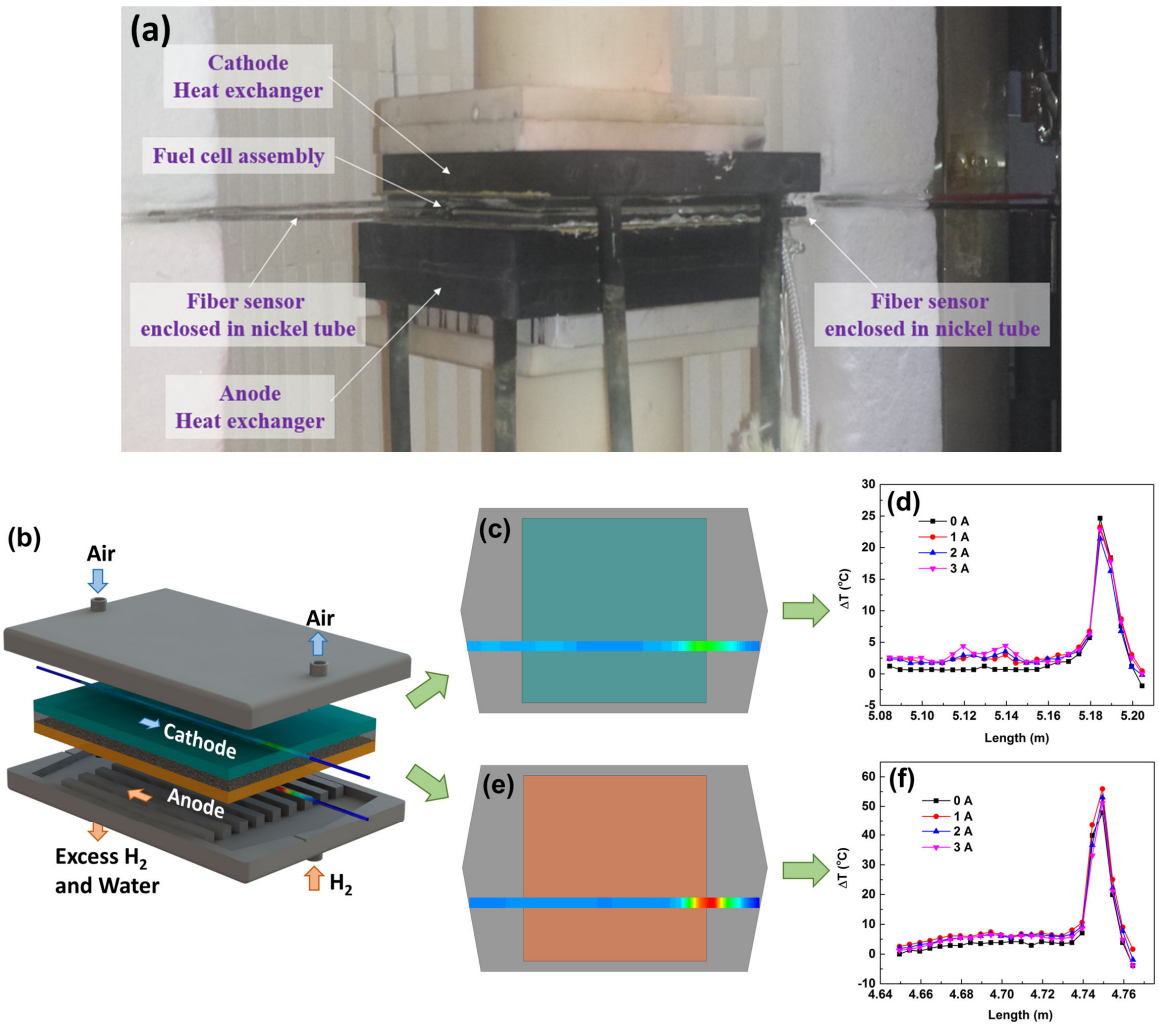

Figure 6. Temperature variation change of the cathode and anode in the solid oxide fuel cell at different current load. (a) Photograph of a fuel cell with an inserted fiber sensor, (b) schematic of the

solid-oxide fuel cell. Distributed temperature measurements in cathode (b-c) and anode (e-f) at current 0 A, 1 A, 2 A, 3 A respectively with 100% hydrogen fuel.

In the previous studies, we have developed and demonstrated distributed fiber sensors for high spatial resolution temperature measurement inside fuel cells with 5-mm spatial resolution. Although this type of sensor can gain high spatial resolution measurement data, the interrogation system used in this type of sensors are very expensive. To address this issue, Pitt researcher teamed up with researcher from Corning Inc and National Research Council to fabricate high-temperature stable fiber Bragg grating sensors in low-cost hydrogen resisting fibers, which can be interrogated by a low-cost interrogation system. The detail technical reports is described below:

Random-hole-clad pure silica optical fibers (RHC) [23-25] are a different class of microstructured fibers where thousands of non-periodic gas filled voids or bubbles are incorporated into the cladding region. In RHC fiber, guidance of light results from a lowering of the average effective index of the cladding material as seen by the guided core mode due to the presence of the randomly distributed sub-micron diameter holes [25-27]. **Because of the pure silica nature of this fiber, it is a strong candidate for fiber platforms for harsh environment sensing in the oil and gas as well as the nuclear energy sectors where standard Ge-doped silica fibers suffer from losses due to hydrogen darkening [6] or radiation induced attenuation [28].**

Femtosecond laser inscribed fiber Bragg gratings (fs-FBGs) are an effective sensing technology within harsh environments [29]. The inscription approach has been applied to a number of optical fiber types where traditional grating inscription techniques based on photosensitivity to ultraviolet radiation cannot be applied [30]. This is especially true for type II-IR grating inscription in pure silica core optical fibers such as fluorine-doped clad silica fibers [31] as well as microstructure and photonic crystal fibers [32] for high-temperature applications.

At high temperatures up to 1000 °C, type II-IR gratings in standard optical fibers show good stability with regards to the grating reflectivity or induced index modulation Δn, as well as in the stability of the grating Bragg resonance wavelength λ_B. However above 1050 °C, the λ_B is seen to drift with time. It was proposed that this drifting maybe due to either thermal relaxation of residual stresses or dopant migration which alters the effective index of the fiber core [35]. Recently Bragg gratings were written by an ablation process in suspended core pure silica fibers with a femtosecond laser [40]. These gratings demonstrated high temperature operation up to 1300 °C for short time periods (5 minutes) without significant variation in λ_B or Δn. It is possible then that microstructured fibers comprising a single material, ie. pure silica, will have better stability at high temperatures.

During this period, Type II-IR gratings are written into a specialized pure silica nano-engineered fiber [25, 41] with femtosecond pulse duration near-infrared radiation and a phase mask. The fiber used in this experiment is a RHC fiber manufactured by Corning, which can be made at costs close to that of standard telecom fibers. The cross-section of the fiber is shown in Fig. 7. The fiber has a pure silica core with an ~ 10-μm diameter. The optical confinement is provided by the annulus of randomly distributed air-holes having a diameter of 45-μm. The sizes of the air holes vary randomly from 100 nm to 500 nm in diameter.

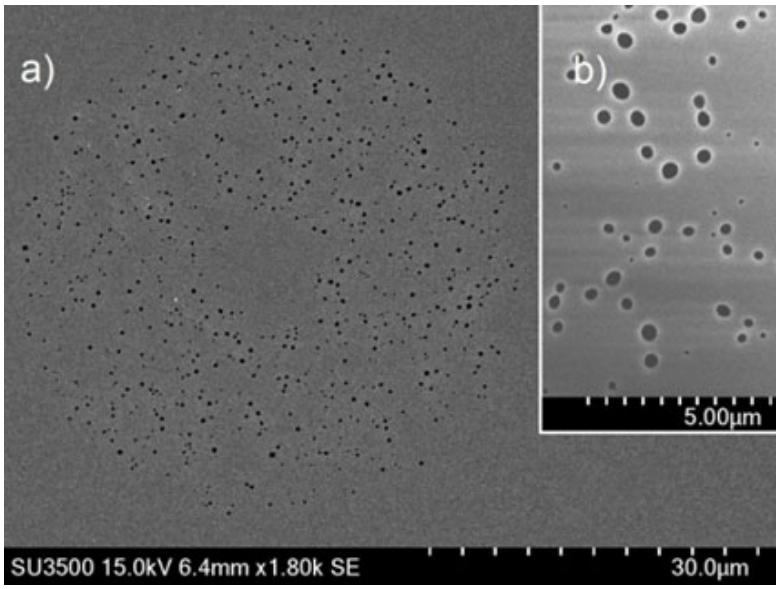

Fig. 7. a) Scanning electron micrograph of the cleaved end face of the core and cladding region of the nano-engineered random hole clad pure silica fiber; b) magnified image of sub-micron diameter holes. Full scales are 30 and 5 µm respectively.

A schematic of the set up used to induce the Bragg grating in the RHC fiber is shown in Fig. 8. A Ti:sapphire regenerative amplifier operating at a central wave-length of 800 nm was used. The fs-beam diameter was ~7 mm at the 1/e2 level. The FWHM transform-limited width of the pulses was ~80 fs, as measured using non-collinear auto-correlation. The linearly polarized laser pulses were focused into the fiber core using a 12 mm focal length plano-convex acylindrical lens (AL) after passing through a phase mask (M) having either a 3.17 µm or 1.07 µm pitch. The fiber was positioned approximately 400 µm away from the 1.07 µm pitch phase mask and 1 mm from the 3.17 µm pitch mask respectively, along the beam propagation direction (see Fig. 8). The AL was dithered ±10 µm at 0.1 Hz with a piezo actuator to scan the beam about the fiber core. Pulses with 900 µJ energies at a repetition rate of 5 Hz were used during the inscription

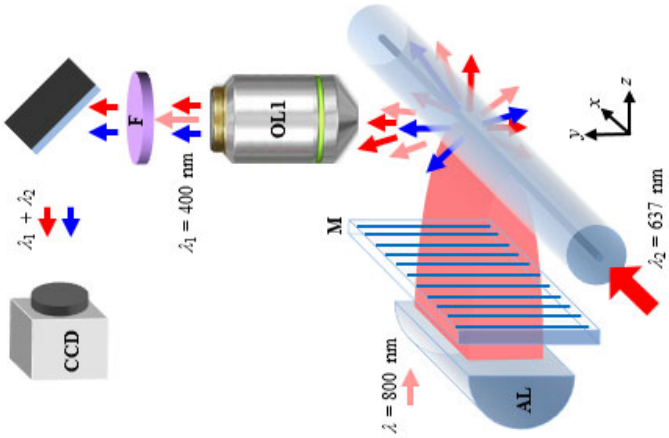

Fig. 8. A schematic of the nonlinear microscopy/dark field microscopy setup used to adjust the FBG inscription process.

Similar to standard PCF, the presence of random holes in the cladding results in significant scattering of the incident laser field used to inscribe the grating. By using a tight focusing geometry and utilizing the technique of nonlinear photoluminescent microscopy as shown in Fig. 8 [42], gratings could be inscribed in the fiber under certain conditions. Inscription of gratings with the 1.07 μm pitched phase mask were challenging as excess scattering of incident laser light in the cladding prevented sufficient laser energy to be transmitted through the fiber for alignment purposes. This excess scattering is likely the result of two issues. Firstly, the 1.07 μm pitched mask, when irradiated with 800 nm radiation, produces ±1 diffracted orders with angles of 48.3° with respect to the normal of the phase mask [31]. The diffracted orders then have an increased path length through the random-hole-cladding by a factor of 1.5 as compared to a beam travelling along the optical axis of the laser. Secondly with the fiber placed 400 μm from the phase mask and with a transform limited pulse duration of 80 fs, pure two beam interference occurs [43]. The resultant fringe pattern of the interference field is half the pitch of the mask meaning each high intensity fringe is a quarter of the mask pitch wide or on the order of the diameter of the random holes resulting in high Mie scattering of the interference fringe [44]. With careful patience a 99% reflecting grating was inscribed (see Fig 9 a). The Bragg resonance λ_B of the grating is 1540.9 nm with a ghost cladding mode at 1538.7 nm. For a fundamental pitch grating, $\lambda_B = 2n_{eff}\Lambda_G$ where n_{eff} is the effective index seen by the guided mode propagating along the fiber and Λ_G is the pitch of the Bragg grating. From the above equation, the n_{eff} of the fiber is then 1.441.

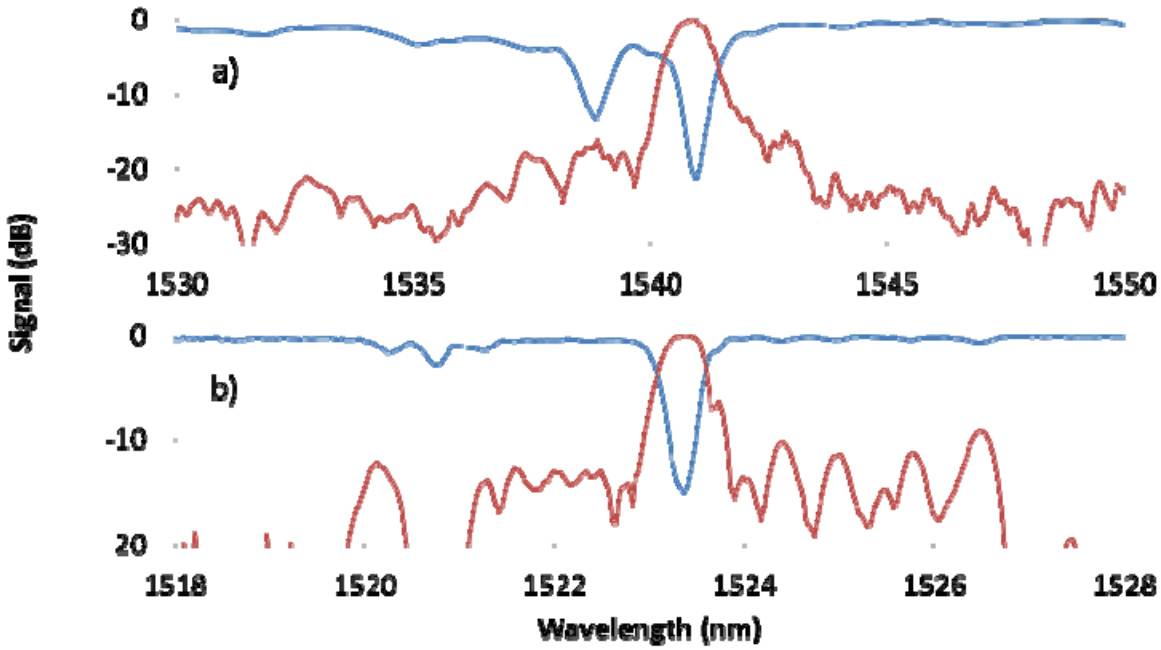

Fig. 9. Transmission (blue) and reflection (red) spectra of FBGs inscribed in the random hole fiber with a) a 1.07 μm pitched phase mask and b) a 3.17 μm pitched phase mask.

To lessen the impact of the scattering effects, the grating inscription was attempted with the larger pitched 3.17 μm period mask which would produce a higher order Bragg resonance in the telecom band. As a result of the phase mask to fiber proximity of 1 mm and temporal broadening of the pulse due to its propagation through the scattering medium of the cladding [44], the interference field pattern at the fiber cladding had a periodicity which was the same as the mask, which would result in a sixth order Bragg resonance. The resulting high intensity fringe was at least a factor of two larger than the largest bubble. The diffracted angles of the ±1 orders from the 3.17 μm mask are much smaller as compared to the 1.07

μm mask (14.4° vs 48.3°) resulting in a significant minimization of the optical path through the random hole cladding. The temporal broadening of the pulse due to its propagation through the scattering medium of the cladding will also promote the inscription of a type II grating structure.

To confirm the thermal stability of the RHC fs-FBG, a device similar to the one shown in Fig. 9b) was placed in tube furnace in air and isochronally annealed up to 1150 °C. For comparison, a type II-IR FBG was also written in SMF-28® telecom fiber using the same exposure conditions as for the RHC fs-FBG and was placed in the tube furnace alongside the RHC fs-FBG. Figure 10 shows the variation in grating strength as a function of annealing temperature. It is observed that there is little variation in the index modulation of either grating below 1000 °C. Above 1000 °C, the gratings begin to erase.

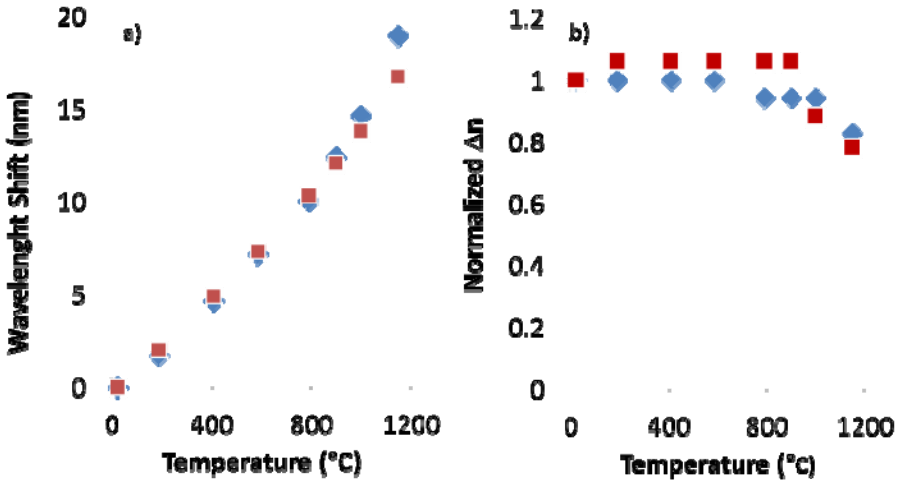

Fig. 10. a) Wavelength shift with temperature and b) variation in index modulation as a function of isochronal annealing up to 1150 °C of FBGs in the random-hole clad silica fiber (blue diamond) and SMF-28® fiber (red square).

The FBGs were then maintained at 1150 °C for an extended period of time. Figure 11 presents the wavelength shift of FBGs as a function of time. It is seen that in the case of the type II-IR grating in SMF-28®, linear drift in the Bragg resonance wavelength is observed (~100 pm/hr). In the case of the RHC fs-FBG, significantly more wavelength drift is initially observed at a higher rate than the SMF-28® fiber (~500 pm/hr), which later reduces to a shift similar to the SMF-28® fiber. At this temperature significant erasure is observed for both the random hole clad and the SMF-28® fiber gratings. When using the phase mask approach, the type II grating structure is the result of nanograting formation that occurs in the high intensity portions of the interference field when subjected to multiple writing pulses [46]. Disappearance of femtosecond laser induced nanogratings in bulk silica has been observed at temperatures of 1200 °C [47].

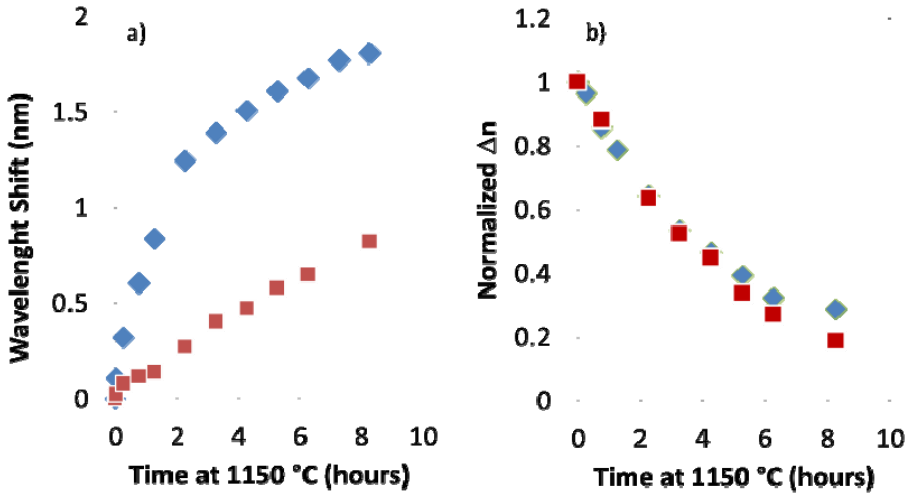

Fig. 11. Comparison of a) wavelength drift and b) reduction in index modulation of FBGs in random hole fiber (blue diamond) and SMF-28® fiber (red squares) as a function of annealing time at 1150 °C.

In a second experiment, a similar RHC FBG and an FBG in SMF-28® fiber were isochronally annealed up to 800 °C. They were then maintained at 800 °C for 125 hours. No erasure of the Δn was observed for either grating however some modest wavelength shifts were observed for both FBGs: ~8 pm per day for the SMF-28® fiber device and ~20 pm/day for the RHC device. See Fig. 12a). The temperature of the devices were then increased to 1000 °C and again little change was observed in the grating reflectivity. However the λ_{Br} of the gratings continued to shift to longer wavelengths at larger rates, ~27 pm/day for the SMF-28® fiber device and ~82 pm/day for the RHC device (see Fig. 12b).

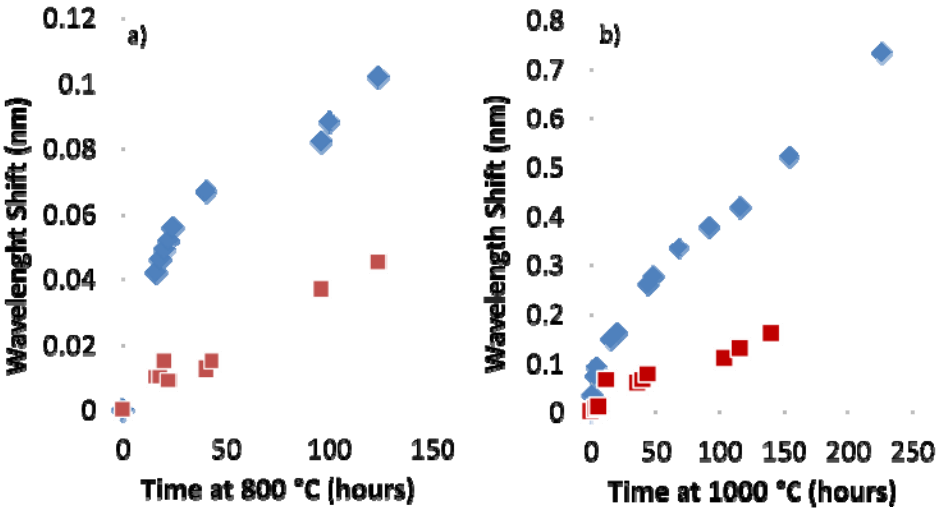

Fig. 12. Comparison of wavelength drift at sustained temperatures of a) 800 °C and b) 1000 °C of FBGs in random hole fiber (blue diamond) and SMF-28® fiber (red squares) as a function of time.

The λ_{Br} is related to the n_{eff} and the grating period Λ_G. Both these terms are changing with temperature but their high temperature behaviour is not well understood. Below the fictive temperature of

the glass fiber, the contribution of the variation of Λ_G with temperature to the λ_{Br} shift is small compared to the contribution determined by the variation in n_{eff}. For fiber Bragg gratings n_{eff} is determined by two factors: the neff of the unperturbed fiber and the average effective index resulting from the grating index modulation (Δn_{avg}). A reduction in the average effective index due to a reduction in Δn (grating erasure) would correspond to a wavelength shift to shorter wavelengths that it is contrary to the experimental evidence at high temperature (Fig. 10 and 11).

Increases in core index of SMF-28® fibers through thermal relaxation of residual stress have been observed at temperatures of 900 °C [46]. Such an increase in the core index would manifest itself as a wavelength shift to longer wavelengths. The drift of λ_{Br} could then be attributed to irreversible changes in the unperturbed refractive index of the fiber, grating length or both and is common to both SMF-28® and all silica core fiber. In the case of the RHC fiber, potential-hole collapse in the cladding region at elevated temperatures would result in an increase in the average index of the cladding resulting in an increase in n_{eff}. This would result in a positive wavelength shift of the λ_{Br}.

In summary, in this period of performance, we present results of Bragg grating formation in a specialized pure silica microstructured optical fiber having a cladding region consisting of a random distribution of sub-micron diameter air holes or bubbles. Being made of a single material, it is demonstrated that FBGs fabricated in this single mode fiber can operate at elevated temperatures and in harsh environments where standard optical fibers are not suitable.

Efforts to Develop Functional Nano-Materials for Sensing

One of the sensing mechanisms of fiber optical sensor is to detect the response of the evanescent wave of the guided mode to the surrounding environment. On the sensing location, sensory material is coated on to the fiber. In order to keep the signal being guided by total internal reflection, the coated material should have effective refractive index lower than that of the fiber core. This research is to develop simple but effective method for coating low effective refractive index mediating polymer layer for the attachment of sensory material on to the surface of optical fiber.

In previous section, we developed metal oxide nanomaterials. Through engineering porosity at 10-nano-meter scale, we can control refractive indices of sensory materials and their dopant variants. In this section, we further develop photonic crystal structures at 100-nm scales, which enable interaction of sensory materials with guided optical light through Bragg interaction. This will further enable the flexibilities of development of sensory materials. In this period, we utilized a scalable 3D nanomanufacturing technique: 3D holographic laser lithography to produce 3D photonic structures and demonstrated its feasibility for on-fiber integration.

1. LITHOGRAPHY METHOD FOR REDUCING EFFECTIVE REFRACTIVE INDEX

In our research, we mixed epoxy-functionalized cyclohexyl polyhedral oligomeric silsesquioxane (epoxy-POSS, EP0408 from Hybrid Plastics 70wt% in cyclopentanone) with 0.75 wt% photo initiator Cyclopentadienyl(fluorene)iron(II) hexafluorophosphate (Sigma Aldrich) to be the photoresist solution. The solution was spin-coated on the cover slip glass substrates (25mm x 25mm x 170 um) at spin-coating speed of 3000 rpm. Soft bake was performed at 50°C for 10 min. and then 95°C for 10 min. Then a transparent photoresist film was exposed to a two-beam interference setup, as shown in Fig. 13, with incoming laser beam $\boldsymbol{k}_1$ and $\boldsymbol{k}_2$ making an angle of 30° and 8° with respect to the normal of the photoresist film. After the first exposure, the photoresist film was rotated twice for the other two exposures, and the rotation angle is 120°. The laser source is Finesse (from Laser Quantum, a Nd: YAG 532nm CW laser). The output power was set to 3W, and the beam was expanded to about 40mm in diameter, and an aperture of diameter 18mm was applied to choose the central part of the expanded beam for interference patterning. The exposure time was about 1s for each exposure. After exposure, the photoresist film was baked at 50°C for 10 min. and then 95°C for 10 min. Development was done by putting the film in PGMEA (Propylene glycol monomethyl ether acetate, Sigma Aldrich) for 1 hour, and rinsed in IPA (isopropanol, Sigma Aldrich) for 20 min then in DI water for 1 min. Samples were dried in air finally.

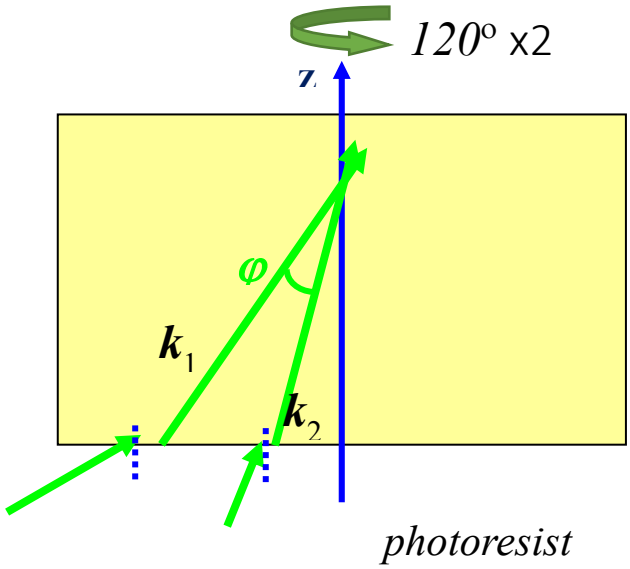

Fig. 13: Scheme of two-beam laser interference setup for patterning 3D photonic crystals.

Fabrication result is shown in Fig. 14. An optical image (Fig. 14a) shows the colorful diffraction under ambient illumnation. The overall size of the patterning size is about 12 mm in diameter, with the consideration the laser beam is still guassian after expansion and only exposure dose over the crosslinking threadshold could give patterns on the substrate. SEM images in Fig. 14(b-d) reveals the feature of the 3D structure. It has three dimensional FCC-like perioic structure with (111) direction papendicular to the substrate. The period in-plane is about 2um, and about 4um for (111) direction. The most interesting feature is in the nano scale porosity uniformly distributed in the over all periodic 3D scheleton. This is achieved because water is a poor solvent for the POSS polymer, the polymer chains collapsed instead of being swelled.

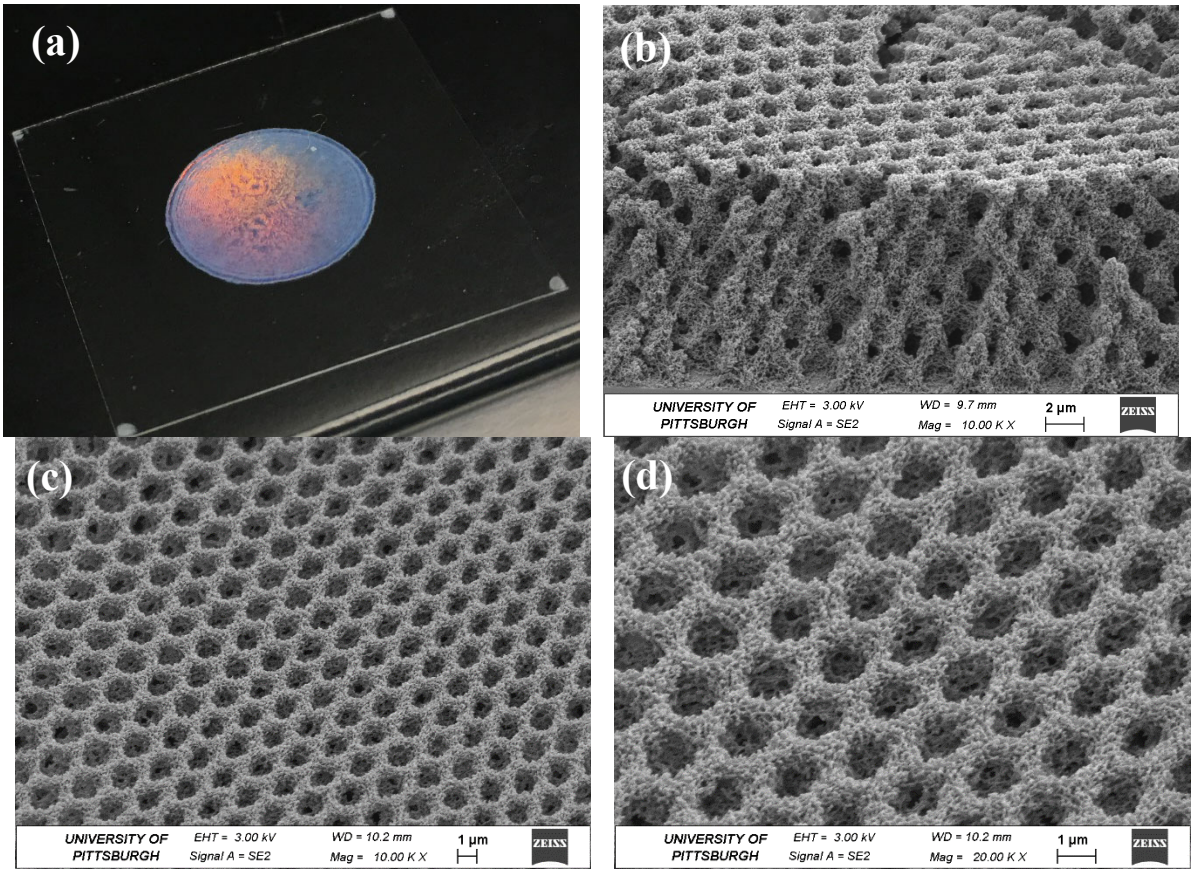

Fig. 14: FCC-like 3D photonic crystals fabricated in POSS material. (a) optical image of the overall sample on cover slip glass substrate 25mm x 25mm. SEM images of sample (b) cross section (c) top and (d) top zoomed. Nano scale porosity uniformly distributed in the over all periodic 3D scheleton.

2. PHYSICAL ABSORPTION OF SENSORY MATERIALS

Then we tested the physical absorption of ZIF-8 by the porous 3D sample as shown in Fig.14. A drop of ZIF-8 solution (0.2g/L in methanol) was dropped on to the POSS 3D sample, after dried in air, the sample was observed under electron microscope. Results are shown in Fig. 15. A close observation in Fig. 3(a) shows the size of the periodic holes at the top of the POSS 3D structure is about 10 times the size of the ZIF-8 nano crystals. ZIF-8 nano crystals conformably wrap around the 3D skeleton. At the hole position, ZIF-8 nano crystals drop into the holes, so we still can see the hexagonal arrangement of the periodic skeleton. Lower magnification images in Fig. 15(b) and (c) show that ZIF-8 nano crystals are densely absorbed on the top surface and surface of the cracking portion of the sample. However, the ZIF-8 nano crystal has very little distribution deep into the bottom layers of the 3D skeleton. Possible reasons include the high concentration of the ZIF-8 solution, the shape of the nano crystal, and the connectivity of the 3D skeleton. These will be the problems to solve in the next stage.

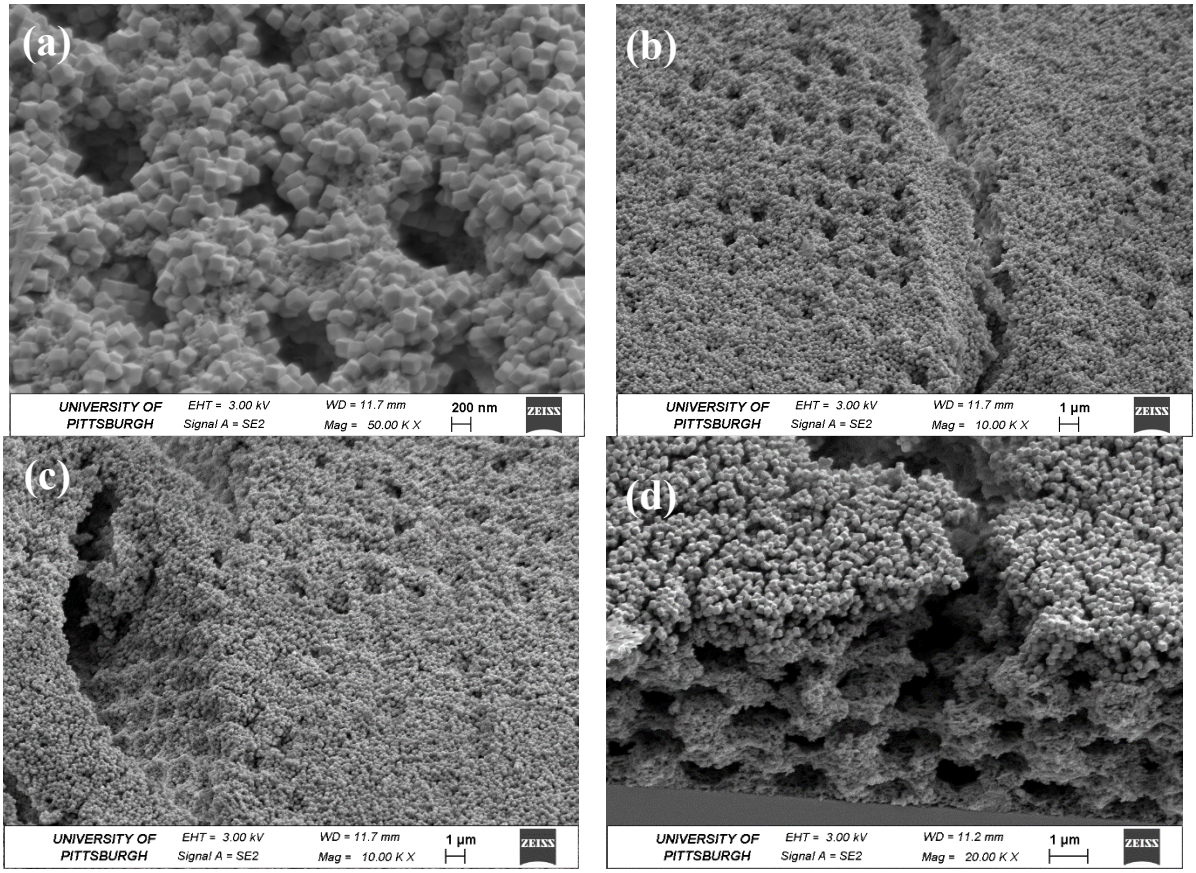

Fig. 15: SEM images showing the absorption of ZIF-8 nano crystals on the 3D POSS skeleton with micro-nano hierachy porosity. (a) ZIF-8 nano crystal wrap around the top hexagonal skeleton of the 3D photonic crystal as shown in Fig. 2. (b-c) Dense absorption on top and cracking surface of the skeleton. (d) Cross section view shows little ZIF-8 crystals go deep into the bottom layers of the skeleton under applied experimental condition.

3. INTEGRATION ON D-SHAPE OPTICAL FIBER

In this period, efforts have also been put on fabricating sensory material carrier layer on optical fiber. For our primary try, we fixed a piece of optical fiber with exposed cladding on glass substrate and follow all the fabrication procedure as in section 2. After fabrication, we departed the fiber from the rest of the excessive structure on the glass substrate for characterization.

Fig. 16 is the optical image of the fiber under ambient illumination. Colorful diffraction directly from the optical fiber indicates that periodic structure is formed successfully on the fiber surface. The black cover on the ends of the fiber is the sputter-coated Pd/Au conductive film for SEM imaging.

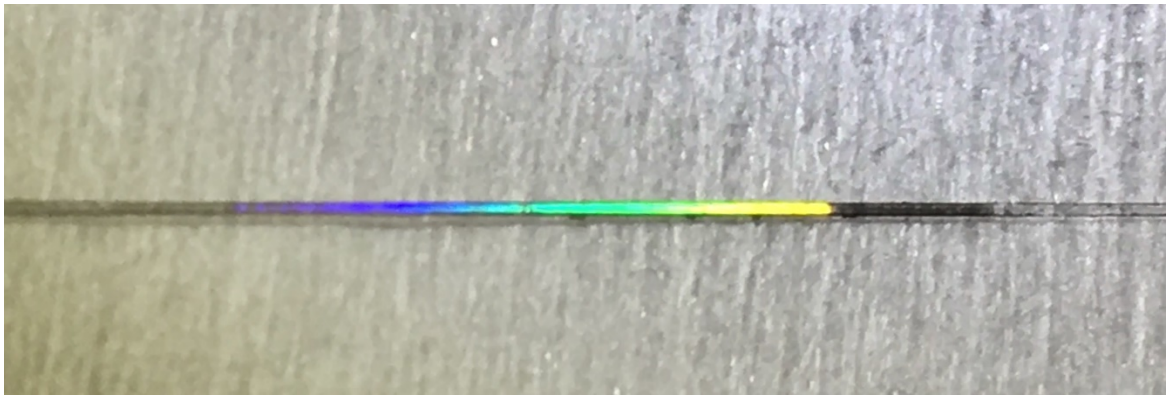

Fig. 16: Optical image of the fiber coated with POSS photoresist after interference lithography under ambient illumination.

SEM images in Fig. 17 show the periodic structure on the fiber surface, corresponding to the colorful section in Fig. 16. (When looking at Fig. 17, it's better to zoom in to above 300% of this document.) Fig. 17(a) is the center part of the periodic structure on the fiber. It shows that the upper edge of the fiber has structure, and the lower edge is bare glass, which implies that the photoresist film was formed unevenly at the stage of spin-coating and soft baking. One possible reason is that the fiber was not strictly leveled. So it should has less layers towards the lower edge and more layers towards the upper edge, as is shown also in Fig. 17(b). Fig. 17(c) shows the end of the colorful pattern along the fiber axis, where it is the far end of photoresist film formed by spin-coating, so it is normal to have thinner edge of the overall periodic structure, the same as fabrication on flat glass substrate. Fig. 17(d) was taken by scratching the structure on the fiber, so it reveals the fiber surface underneath of the periodic structured cladding formed by interference lithography. We need to improve the fabrication technic of fabricating periodic structure on optical fibers. One possible direction is to have a groove made into a glass substrate to accommodate the optical fiber, so that the optical fiber surface can be level to the surrounding glass substrate. In this way, we may solve the problem of applying photoresist film with even thickness, which is the base of good fabrication result.

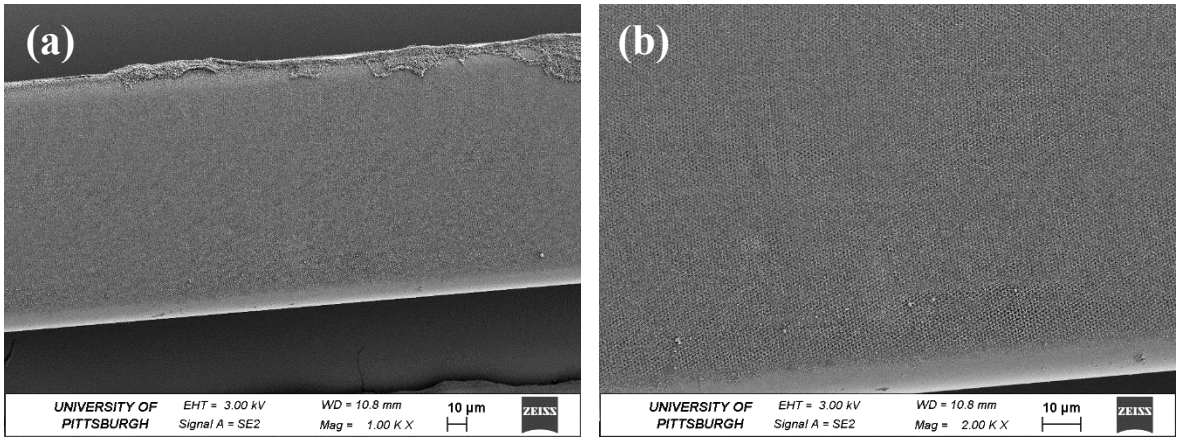

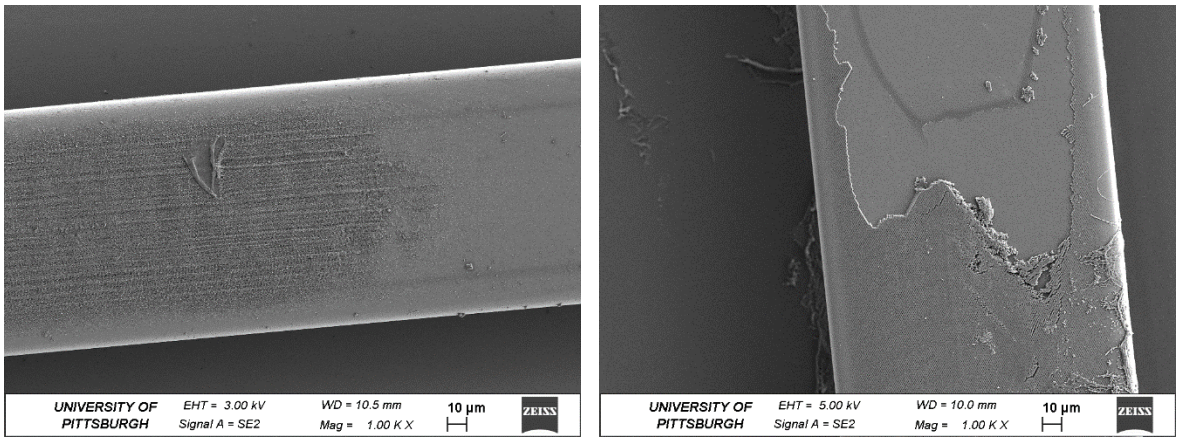

Fig. 17: POSS photonic crystal fabricated on D-shape optical fiber flat surface. (a) center part of the overall structure on the fiber; (b) lower half the structure in (a); (c) one end of the overall structure along the fiber axis direction; (d) scratched structure on fiber revealing the periodic cladding formed by interference lithography and underneath fiber flat surface.

4. FUTURE EFFORT:

Based on our efforts performed in this period, we will carry out further fabrication and testing works based on 3D photonic crystal integrated on optical fibers.

a. Determine the effective refractive index of the periodic cladding on fiber, i.e. the 3D photonic crystal skeleton with nanoscale porosity fabricated from POSS.

b. 2D photonic crystal skeleton with nanoscale porosity will be fabricated as well, since it is an option for thinning the sensory material carrier cladding layer further, if we find in the coming experiment that 3D multilayer structure is too thick for the evanescent wave sensing operation.

c. More effort will be put on the integration of sensory material, such as metal oxide nanomaterials, or metal organic framework materials into the POSS carrier structure with 3D periodicity and hierarchy porosity.

d. Based on the above technical achievements, optical fiber gas sensors will be fabricated finally and tested for the final stage.

Efforts on Development of Distributed Fiber Sensor for High-Temperature Environments using Silica and Sapphire Fibers

Purpose

Silica optical fiber sensors are known to be resilient sensors under many harsh environments. Compared to electronic sensors, fiber sensors have shown better survivability and performance under high temperature. Moreover, a unique trait for fiber sensors is its inherent capability to perform high spatial resolution distributed measurement. OFDR based on the Rayleigh backscattering can achieve high spatial resolution measurement with resolution better than 1-cm.

Previously, we successfully fabricated distributed fiber sensors in D-shaped fibers, which exhibited outstanding thermal stability and optical measurement performance. In this study, we further expand our femtosecond fabrication capability in to fiber with cylindrical geometries including both silica and sapphire fibers.

1. ULTRAFAST LASER FABRICATION OF FIBER SENSORS

In this quarter, we expand our ultrafast laser fabrication capability to produce fiber sensors on cylindrical shape fibers. An ultrafast processing method on silica optical fiber for improved stability under harsh environment for distributed sensing applications in nuclear cores was discussed as following and shown in Figure 18.

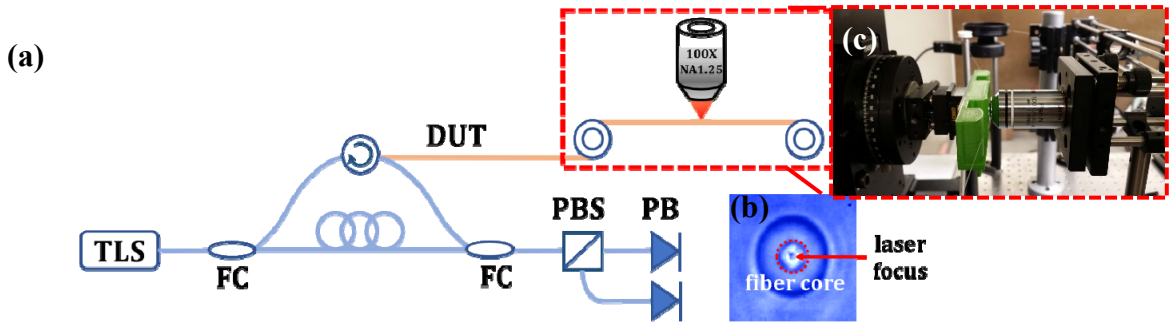

Figure 18. Schematic sketch of round fiber Rayleigh Enhancement setup. (a) Rayleigh enhanced optical fiber processing setup. (b) Optical microscope image of the cross-section of a Rayleigh enhanced Vascade fiber, the arrow points to a structure similar to ultrafast laser waveguide formed at the focusing spot in the core of the fiber. The red dashed block shows a roll-to-roll setup for long distance manufacturing. (c) Photo roll-to-roll setup, a 100X objective focuses laser beam at the core of the fiber on a home-made mount.

Coherent RegA system producing 300 fs pulse width (FWHM) at 800 nm, 250 kHz repetition rate, was used to perform processing on a single-mode and Vascade fiber samples. The laser beam was linear polarized and spatially shaped using a cylindrical telescope for symmetrical beam shape. Up to 200 nJ energy was focused into the core of the fiber using an oil-immersion objective (NA 1.25) with immersion

oil (refractive index 1.518) to eliminate the effect of spherical aberration due to fiber's cylindrical shape. Fiber was translated in a direction perpendicular to the beam propagation direction, using a roll-to-roll setup. An optical backscattering reflectometer (OBR Luna 4600) was used for real-time monitoring of the Rayleigh backscattering profile. Figure 19 show the photograph of the entire ultrafast laser fabrication setup.

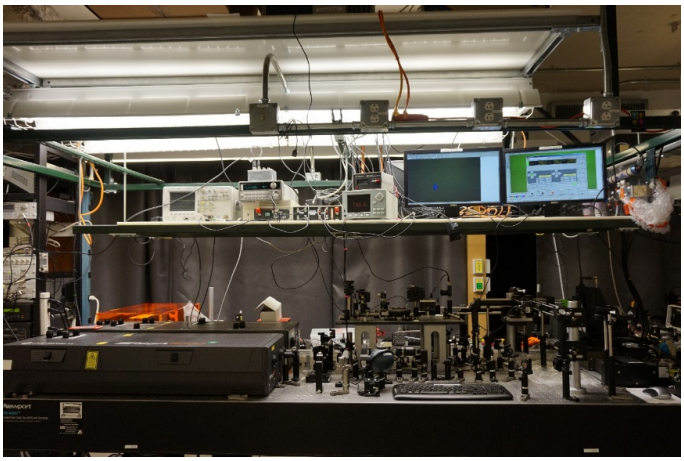

Figure 19. Picture of the ultrafast laser processing setup.

After the ultrafast laser irradiation, an enhancement of 40-45 dB was measured from the OFDR. This enhancement can be attributed to the formation of nanograting inside transparent material at ultrafast laser tight focusing condition[2]. To verify the high temperature stability, the sample was first annealed at 800ºC for 40 hours inside a thermal insolated tube furnace, data of these tests is shown in Fig. 20. A decrease in the propagation loss at the enhanced region during the annealing process was observed, which enables future processing of longer Rayleigh enhanced regions with minimal loss.

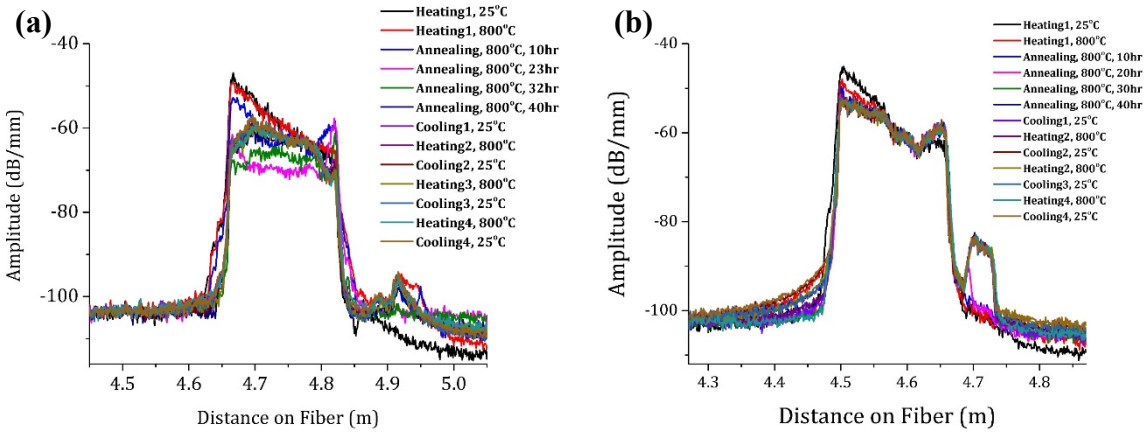

Figure 20. Single-mode fiber (left) and Vascade fiber (right) high temperature performance repeatability test. (a)-(b) shows the Rayleigh backscattering profile change before and after annealing, and during various cycles of heating and cooling.

The temperature coefficients were calibrated up to a second order coefficient and measured at a temperature step of 100ºC, and using 1cm gauge length. Repeatability test was done to demonstrate the resistance of the processed fiber against changing temperature as shown in Fig. 21 The furnace

temperature was heated to above 800ºC then decreased to the room temperature. Since little change in the Rayleigh enhanced region was observed after, the fiber was demonstrated to be stable for high

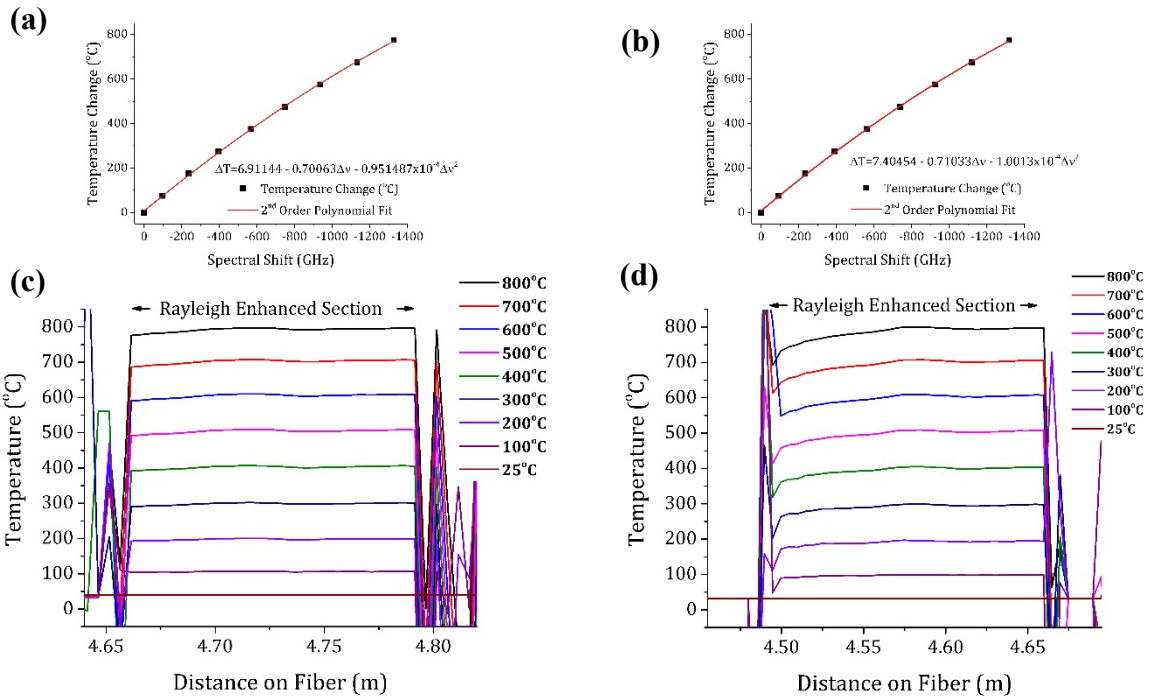

Figure 21. Temperature increment test on single-mode fiber (left) and Vascade fiber (right). (a)-(b) A second-order polynomial fit of the spectral shift vs. temperature during a calibration cycle from room temperature to 800ºC. (c)-(d) Temperature measurement on annealed fiber at an increment step of 100ºC.

temperature measurement.

Single crystal sapphire optical fibers have been produced and reported on extensively for decades. Sapphire has a melting point above 2000ºC, and has considerably greater resistance to hydrogen infiltration than fused silica. Generally, sapphire optical fiber is produced using the Laser Heated Pedestal Growth (LHPG) technique[4-6].

In order to perform temperature sensing at very high temperatures, we have worked with NETL researcher Dr. Michael Buric to obtain sapphire optical fibers, which were fabricated and modified using NETL in-house LHPG system as shown in Figure 22. The system contains a 100 W CO_2 laser, refraxicon optic, and parabolic focusing mirror to heat the pedestal. Precision brushless slotless DC positioning motors are used to control the vertical positions and movement rates of the pedestal and grown fiber. A 2-axis camera system is used to measure the diameter of the fiber and control the growth process. The system has been shown to produce sapphire optical fibers with less than 2% diameter variation over long lengths of fiber. Recently, the capability of continuously modifying the grown fiber diameter was added to the system. While a PID control produces control outputs to achieve a desired diameter, the system can also achieve a novel non-constant diameter profile along the grown-length. This permits the growth of various interesting features in single-crystal fibers.

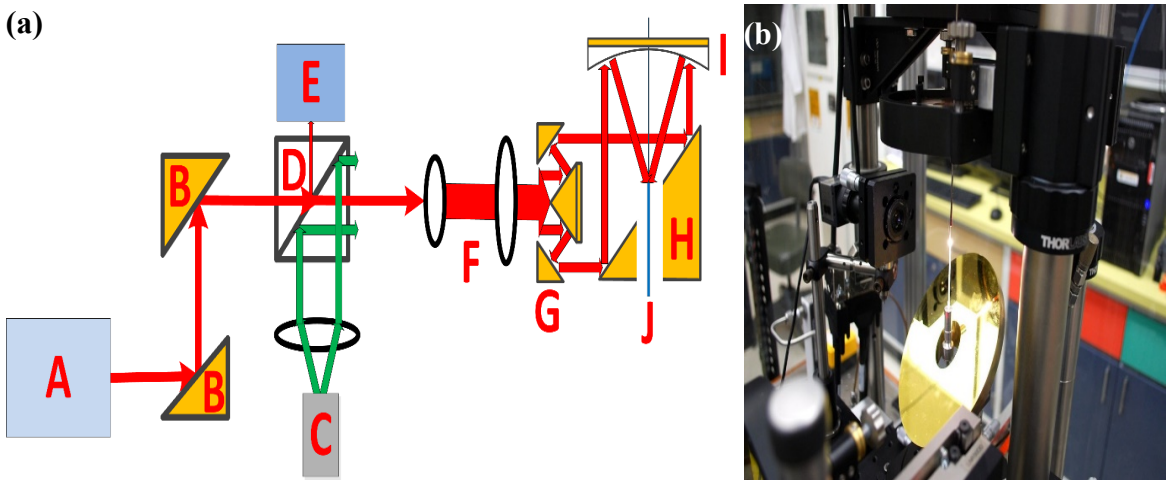

Figure 22. Optical system diagram and LHPG system. (a) A: CO2 laser, B: Gold flat mirrors, C: Alignment LED, D: Beam combiner, E: Power meter, F: Beam expander, G: Reflaxicon, H: 45-degree turning mirror with central hole, I: Parabolic focusing mirror with central hole, J: pedestal rod; (b) NETL LHPG System[8] (Figure provided by Dr. Michael Buric from NETL).

Femtosecond laser irradiation was used to modify the intrinsic backscattering in sapphire optical fiber. A 1-meter length of sapphire optical fiber with a taper at one end and a ball lens at the other was used as the sample sensing fiber. The fiber was positioned between a set of v-groove clamps on an air-bearing motion stage with nanometer precision (Aerotech, ABL20020). The laser (Coherent, MIRA900 with RegA9000 amplifier) produced pulses approximately 250 fs wide at 250 kHz repetition rate and average power of 120 mW. Focusing was accomplished with a 50X microscope objective. An inline camera system permitted imaging of the irradiated sections during writing. As an initial test of the effectiveness of the increased backscattering, the fiber was translated as a speed of 0.25 mm/s.

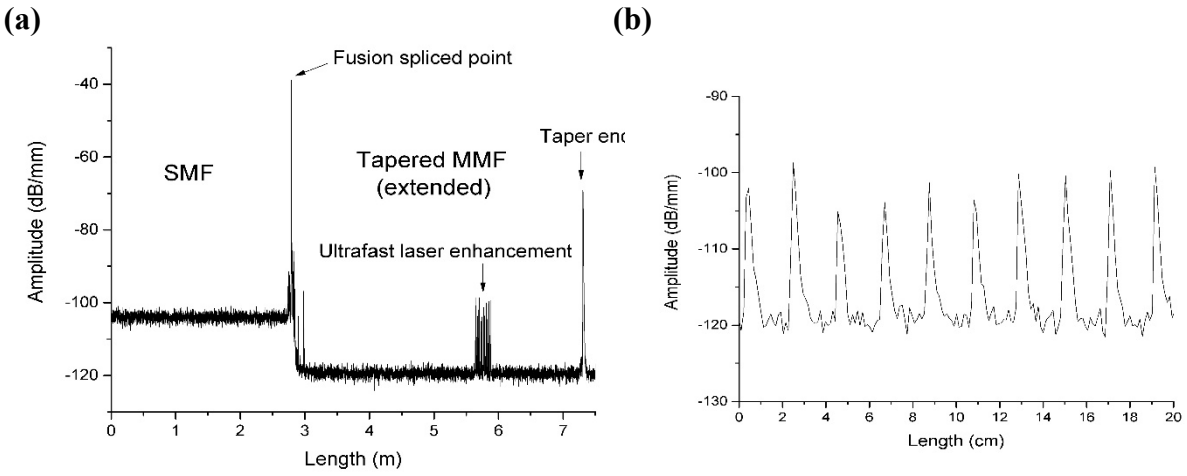

Figure 23: Enhanced Rayleigh scattering profile in sapphire optical fiber. (a) Connection of a single-mode fiber with the multi-mode sapphire fiber with ultrafast laser enhancement sections. (b) Ultrafast laser enhanced region with 10 damage sections.

The laser was turned on for 1 mm and off for 4 mm of translation distance, yielding a writing duty cycle of 20%. The backscatter profile measured during the laser-writing process is shown in Figure 23. Well separated scattering features were observed with an amplitude of approximately 10 dB. This meant that the peaks in the enhanced backscattering sapphire section were greater in amplitude than the intrinsic backscattering in the single mode pigtail.

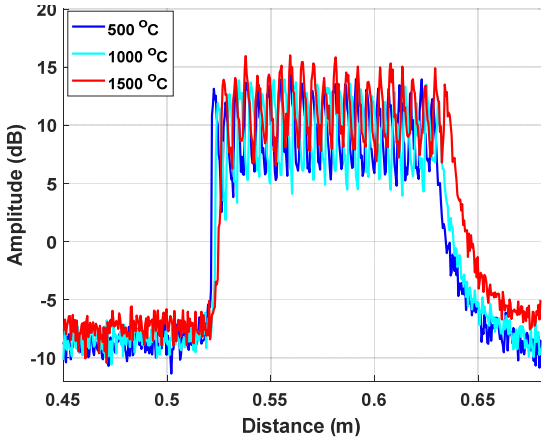

Figure 24. Enhanced Rayleigh backscattering stability during heating of 500ºC, 1000ºC, and

After irradiating the sapphire fiber sensor to produce enhanced Rayleigh backscattering over a 10 cm sections near the center of the 1-m fiber, the sensor fiber was placed inside a tube furnace with air atmosphere for annealing and testing. Initially, the fiber was heated to 1000°C for 5 hours to anneal some of the residual strain induced by the femtosecond laser irradiation. This step did not appreciably change the backscattering profile. After annealing, the fiber was re-heated in 100°C increments while recording the backscatter profile. Figure 24 shows the enhanced backscattering profile along with the central tube-furnace thermocouple reading as the furnace was ramped up to 1500°C. This point corresponds to the center point in the hot zone, which is also the hottest point in the furnace and is approximately equal to the furnace set point after equilibration. In the Figure we can see that the backscattering was stable even at the maximum 1500°C temperature. The features did not change in magnitude or position in any measurable way, confirming the stability of the enhancement features and fiber transmission during the test.

Summary:

In this study, we continue to improve our ultrafast laser fabrication capability on producing fiber optical sensors on optical fibers. The technical efforts made in this program lead to a drastic expansion of our laser fabrication capability. We now are able to fabricate fiber sensors on all fibers with cylindrical geometry, this is significantly improvements from previous efforts while we only can produce fiber in D-shaped fibers.

Notably, we worked with NETL scientists, for the first time to our best knowledge, we have successfully fabricated distributed fiber sensors in crystalline sapphire fibers. Stemming from our efforts, we will integrate high-temperature sensory material on both cylindrical silica and sapphire fibers to perform distributed chemical measurements.

Efforts on Development of Silica Nanostructures on Fibers for Distributed Sensing

Distributed fiber optic sensing is a potentially powerful technique to measure the spatial temperature profile of an operating SOFC (Solid Oxide Fuel Cell) system. Being well-suited for harsh environment sensing applications, fiber optic sensors have been widely used for high-temperature measurements. Distributed sensing schemes such as Rayleigh-scattering Optical Frequency Domain Reflectometry (OFDR) can perform distributed temperature sensing using unmodified single-mode optical fiber to achieve <1-cm spatial resolution. One of the key challenges of distributed sensing using the Rayleigh backscattering is the weak Rayleigh-backscattering intensity exhibited by conventional optical fibers. The weak Rayleigh backscattering is hardly a surprise, given that telecommunications optical fibers are designed for low-losses, including low Rayleigh-scattering losses. To address this challenge, several approaches have been attempted to increase Rayleigh scattering in single-mode fibers[6,7]. The enhanced Rayleigh scattering profiles result in larger scattering signals at the detector(s) and better spectral correlation quality between the measured high-temperature Rayleigh profile and the reference room-temperature Rayleigh profile. This in turn improves the fidelity of the distributed measurement as well as the useful range of temperatures over which the sensor-fiber can operate effectively. However, even though Rayleigh scattering enhancement may be used to effectively extend the operational temperature and fiber longevity, eventually environmental effects will overcome the stability of the measurement during extended periods of high-temperature operation (>700^{o}C). At the highest operating temperatures, the same fiber core structural non-uniformities that give rise to the intrinsic Rayleigh scattering undergoes permanent changes[8]. These changes will eventually compromise sensitivity and reliability of the distributed measurements, although the use of the types of scattering enhancement modifications described here may delay or mitigate the effects of such degradation, yielding a new regime of measurement capability.

In this study, we have used reactive ion etching (RIE) to produce enhanced Rayleigh scattering profiles in optical fibers that are stable at high temperatures. RIE is found to be able to produce large area non-periodic pillars with diameter in 100 nm scale on optical fibers, and we call it nano grass structure. The resultant enhanced fibers is promising to perform distributed temperature sensing in highly reactive fuel gas (hydrogen) stream. We also integrate the sensory material into HfO2 strengthened 3D photonic crystal for new scheme of light scattering, which is promising for higher sensing sensitivity.

Experiments and Results

To enhance the Rayleigh backscattering profile in optical fibers, RIE (Trion Phantom III LT) is used to etch the flat surface of D-shape optical fiber. The experimental setup is presented in Fig. 24. D-shape fiber is mounted on a piece of glass plate with jacket peeled off and flat surface facing up. The etched area is determined by the size of the RIE reaction area. In principle, there is no limitation of etching area since we can do sequential etching section by section to have required length of light scattering.

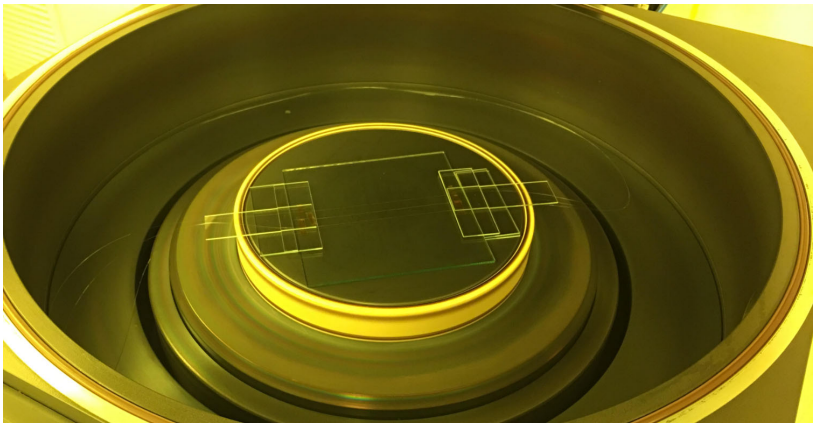

Fig. 25: Mounting of D-Shape optical fiber in RIE chamber for etching.

The backscattering profile can be tuned by controlling the size of the nano grass and also the distance between the bottom of the nano grass and the top of the fiber core. Three examples were fabricated by using the recipes in Table 1. Before etching, the dimension of the original D-shape fiber with jacket peeled off is shown in Fig. 26. The distance between the top flat surface to the farthest point of the bottom is about 75um, and to the center of the core is about 8um. These parameters are used to estimate the distance from the root of nano grass to the top of fiber core, as shown in the last column of Table 1.

Table 1. RIE recipes for etching D-shape optical fiber

Recipe #	Pressure (mTorr)	RIE RF (W)	GAS (sccm)	Process Time (s)	Height of nano grass (um)	Distance from the root of nano grass to the top of fiber core (um)
1	50	150	CHF3(50) /O2(5)	5400	4.7	-0.7
2	50	150	CHF3(50) /O2(5)	2700	2.1	0.16
3	200	100	SF6(40)/Ar(85)	2700	0.1	0

Fig. 26-29 shows the nano grass structure on D-shape fibers corresponding to the three recipes in Table1, and also the Rayleigh scattering profiles. The backscattering profiles of recipe 1, 2 and 3 are shown in Fig.27-29. Recipe 1 give negative distance from the root of nano grass to the top of fiber core, which cuts the core and introduces too much lose for efficient sensing. Compared with recipe 3, fiber etched under the condition of recipe 2 shows higher Rayleigh backscattered intensity, which has the advantage of higher sensitivity for distributed sensing. In the following experiment, recipe 2 is going to be used for the fiber etching.

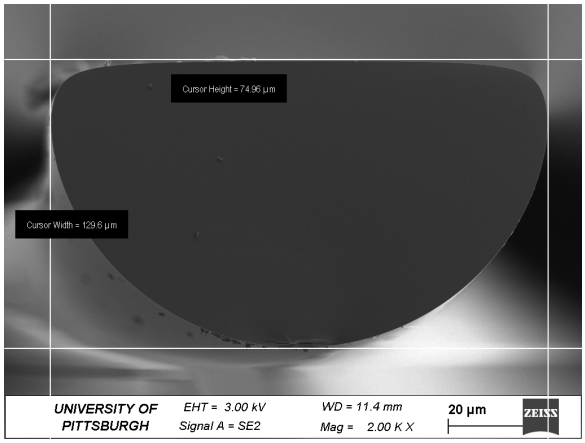

Fig. 26: Cross section of a D-shape fiber before RIE process. The distance between the flat surface and the farthest bottom is 75um.

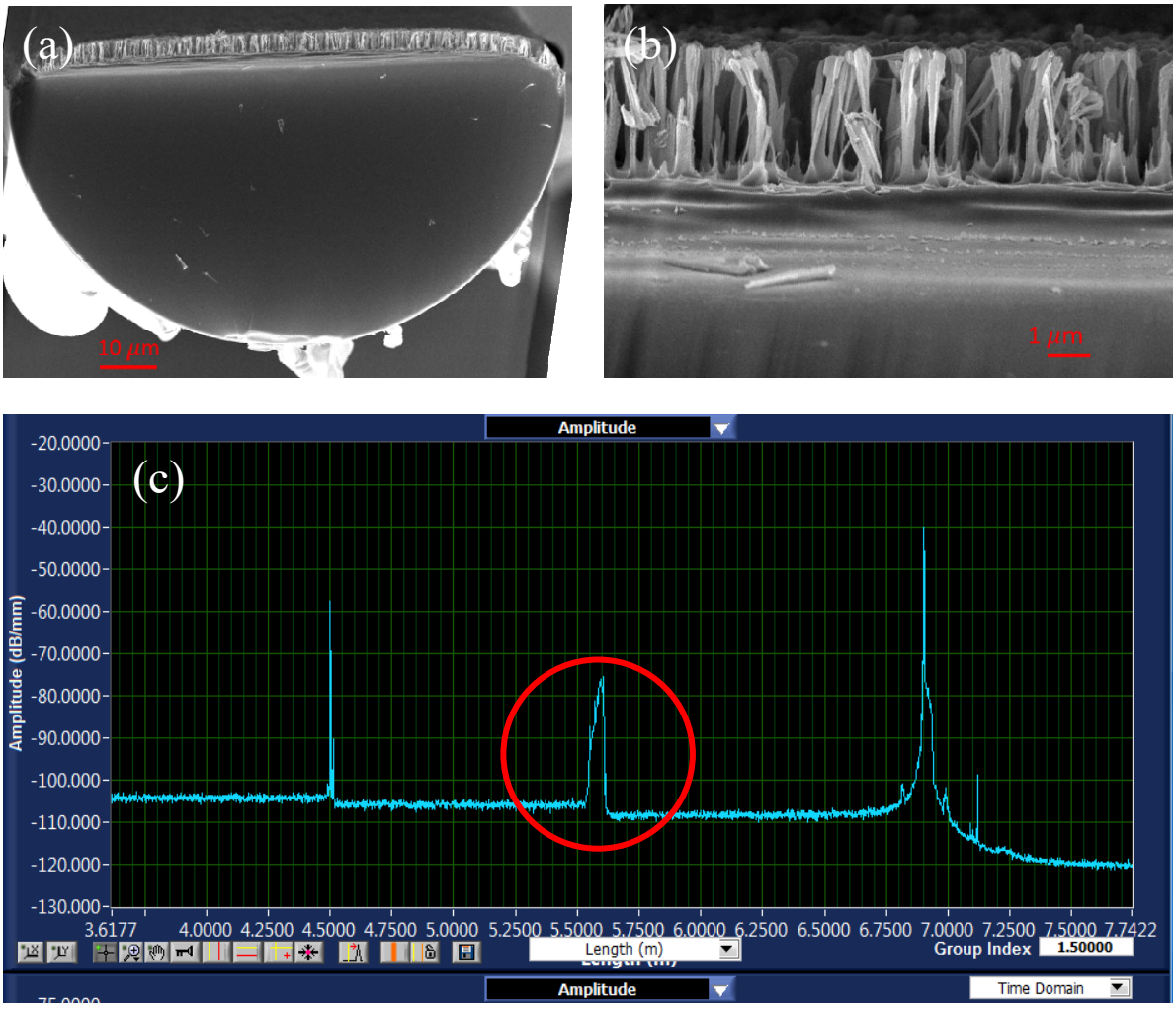

Fig. 27: SEM image of nano grass on D-shape fiber by RIE etching recipe #1, (a) cross section, (b) close-up of cross section, and (c) corresponding Rayleigh backscattering profile.

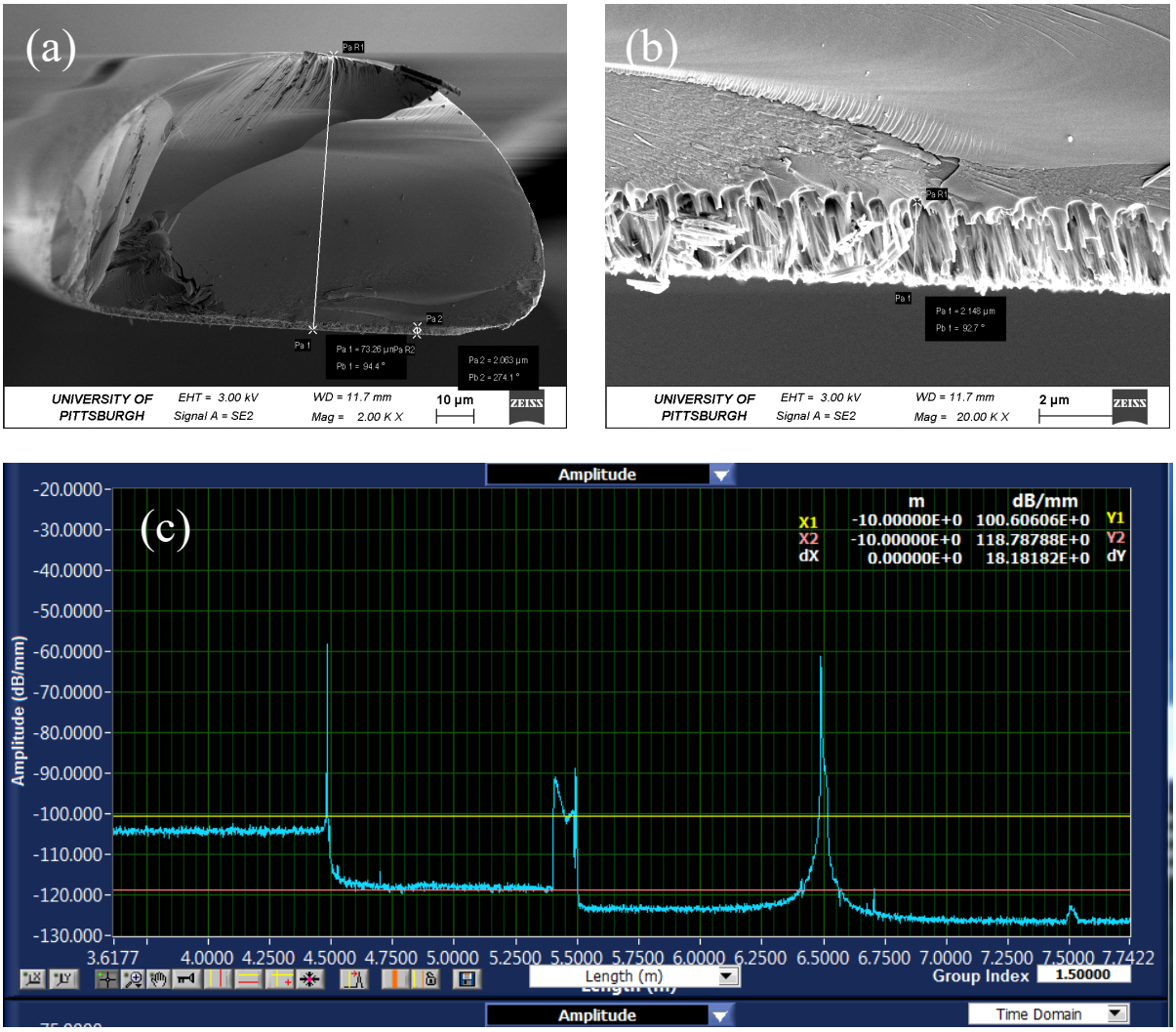

Fig. 28: SEM image of nano grass on D-shape fiber by RIE etching recipe #2, (a) cross section, (b) close-up of cross section, and (c) corresponding Rayleigh backscattering profile.

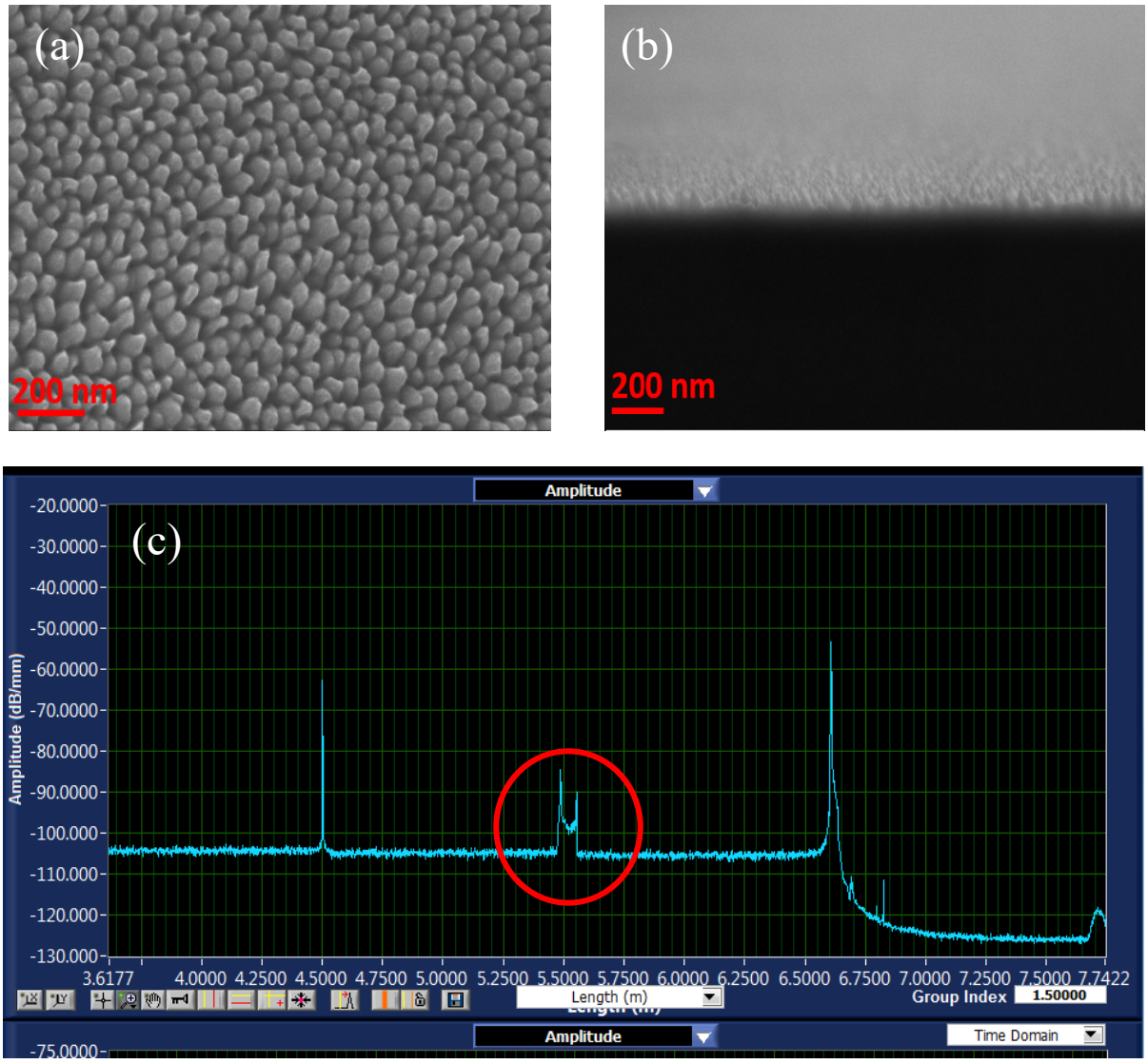

Fig. 29: SEM image of nano grass on D-shape fiber by RIE etching recipe #3 , (a) top view, (b) cross section, and (c) corresponding Rayleigh backscattering profile.

Sensing materials:

After confirming the RIE etching condition, we prepare sensory coating material that will be coated onto the etched D-shape fiber. Here is the steps to make the sensing solution:

1. PdCl2 solution: 0.5 g 35% - 37% HCl is added to 6.4 g of ethanol and stirred until cool down. Then 0.2 g of PdCl2 powder is added and stirred for more than 12 hours to dissolve in room temperature.
2. Ti solution: 0.42g 35% - 37% HCl is added to 5.95 g of ethanol and stirred until cool down. Then 1.5g Ti(OCH(CH3)2)4 solution was added drop by drop and kept stirring until cool down.

3. Ti-Pd solution: 1g of PdCl2 solution from Step 1 is added to Ti-solution. The solution is stirred for uniform mixture.
4. Add F127: Add 0.75g F127 polymer powder to the solution in Step 3, and kept the solution stirred and heated on hotplate at 60°C until drop-coating onto optical fiber.

Coating of sensing material onto optical fiber

After coating solution is prepared, D-shape Optical fiber with the original mounting setup on the glass substrate for RIE is drop-coated with its flat surface facing up for 3 times. The interval between each time is about 5 minutes to let the liquid fully stabilize on the fiber. Before annealing, the sample is put in air under room temperature for hydrolysis for 12 hours.

SEM images in Fig. 30 shows the porous film formed on flat surface of the D-shape fiber after annealing under 600°C for 1 hour. A continuous film is formed with voids in 10 nm scale. The voids are formed through the decomposition of F127 polymer in high temperature.

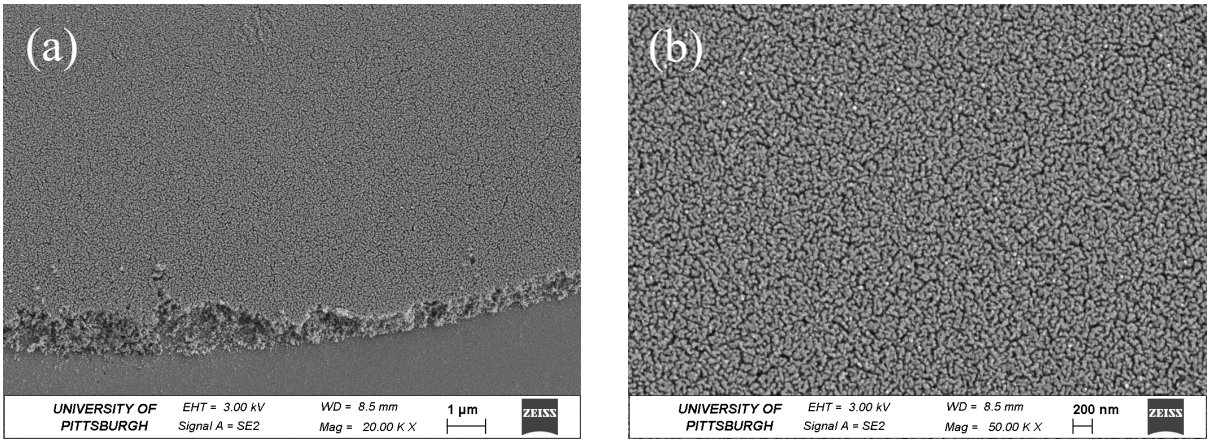

Fig. 30: SEM images of the porous film formed on flat surface of the D-shape fiber after annealing under 600°C for 1 hour. A continuous film (a) is formed with voids in 10 nm scale (b).

SEM images in Fig. 31 shows the coating formed on the nano grass surface of the D-shape fiber after annealing under 600°C for 1 hour. In Fig. 31(a), the center of the fiber has thinner coating than the both edges. Closer looks of the center part in Fig. 31 (b-d) show that the TiO2 coating is not completely attaching to the root of the nano grasses. This introduces air gap between them and the sensing result is not that good as shown in Fig. 32, where the backscattered Rayleigh signal at different hydrogen concentration ranging from 0.5% to 5% is characterized using the OBR made by LUNA OPTICS. As can be seen in the figure, the coated area is from 4.72 to 4.80 m. There is no significant backscattered signal difference under various hydrogen concentration as is shown in the enlarged figure, which means the coated fiber is not sensitive enough for the distributed sensing.

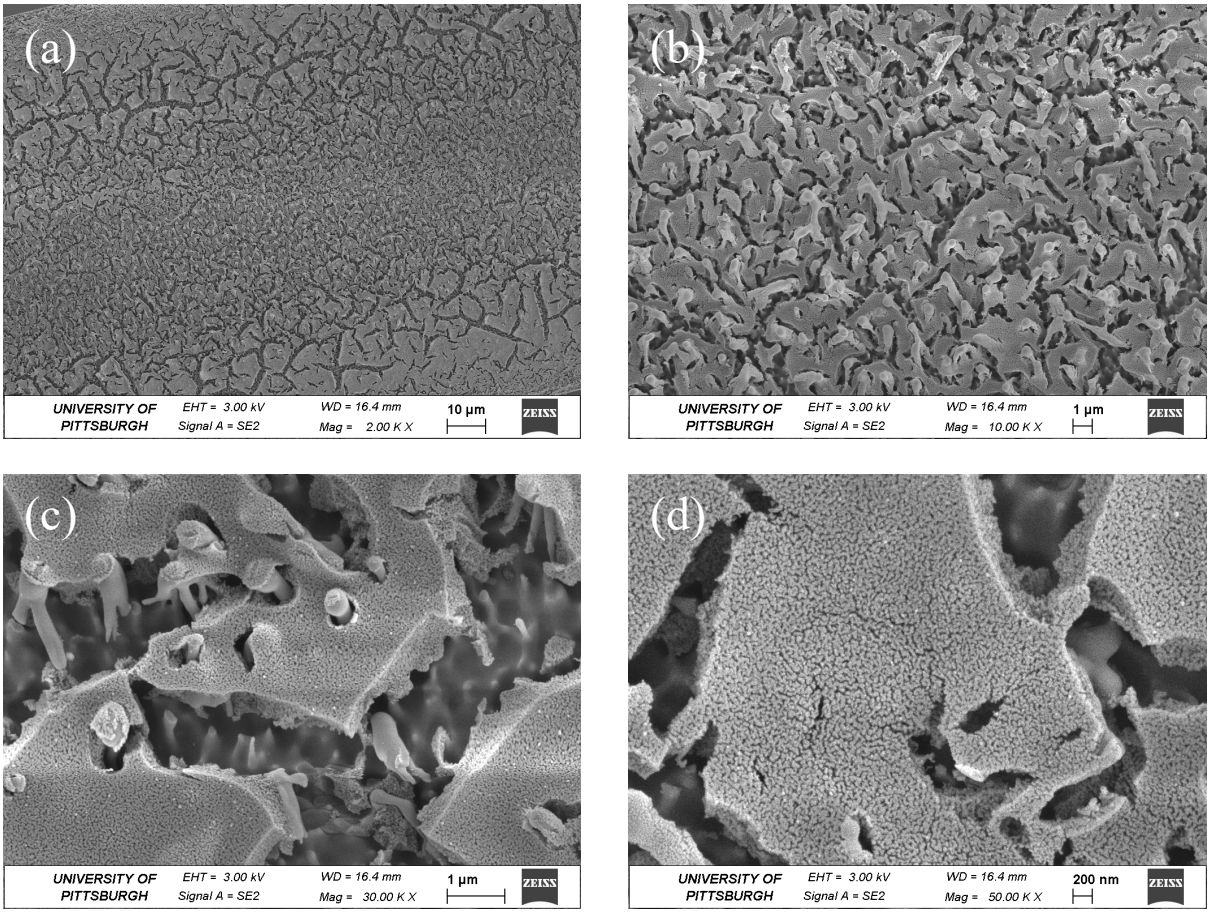

Fig. 31: SEM images of the porous film formed on nano grass surface of the D-shape fiber after annealing under 600°C for 1 hour. A cracked TiO2 film is formed with separation from the root of the nano grass.

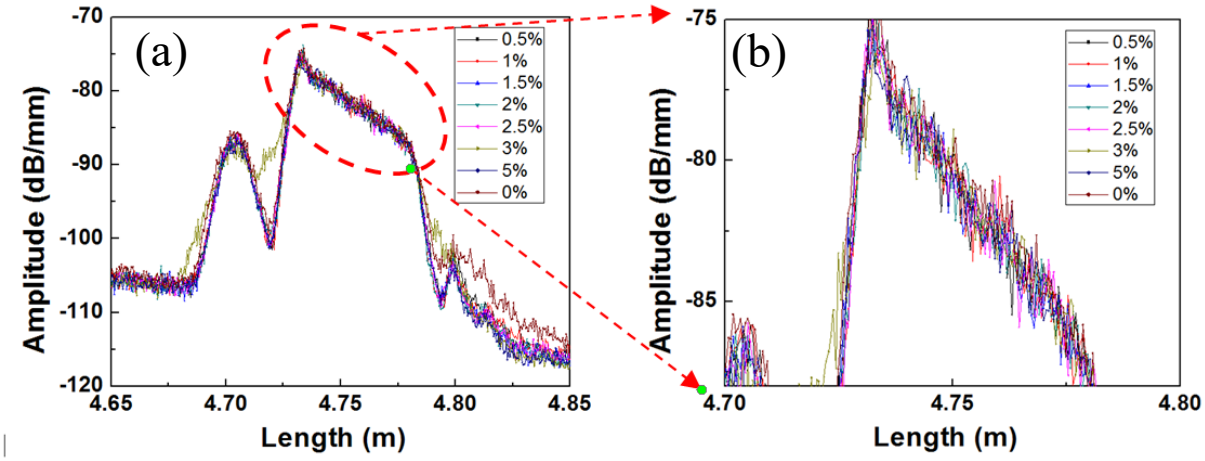

Fig. 32: OFDR of the sensor under different hydrogen concentration (a) and its enlarged view (b).

In order to fill the gaps of the cracked TiO2 film and reduce its separation from the root of the nano grass, a second time of coating after the first annealing was carried on. This second coating includes another three times of drop-coating with 5 minutes interval between them, just like the coating method for the first coating.

SEM images in Fig. 33 shows the second coating formed on the nano grass surface of the D-shape fiber after annealing under 600°C for 1 hour. In fig. 33 (a), cracks were still formed for the second coating. However, when we closed up to the nano grass, as shown in Fig. 33(b-d), we found that the gaps among the nano grass are filled with TiO2 without air gap any more. So this second coating reduces the gap between the TiO2 film and the nano grass formed in the first annealing. EDS result in Fig. 34 confirms that the void between nano grass is filled with TiO2.

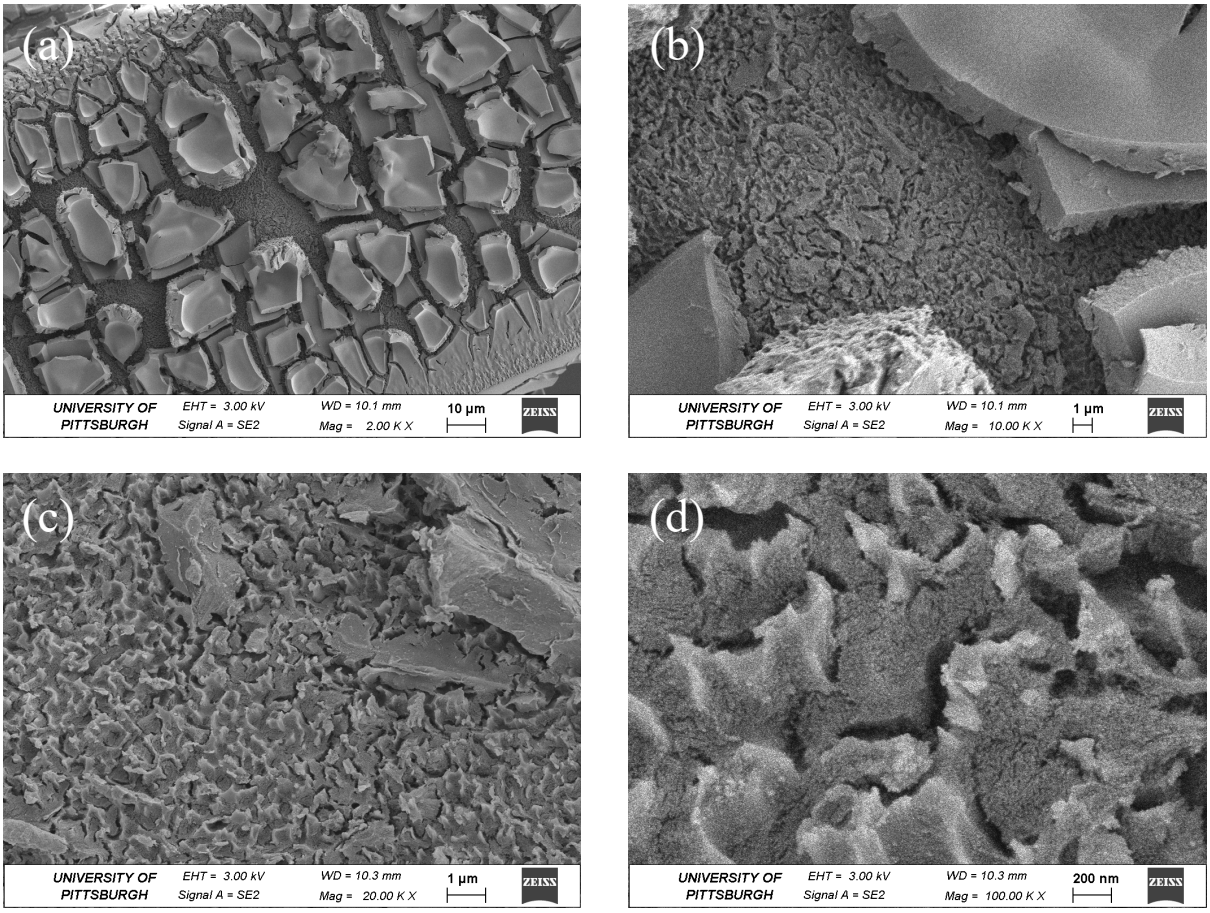

Fig. 33: SEM images for the second coating formed on the nano grass surface of the D-shape fiber after annealing under 600°C for 1 hour. (a) cracks were still formed for the second coating. (b-d) gaps among the nano grass are filled with TiO2 without air gap any more.

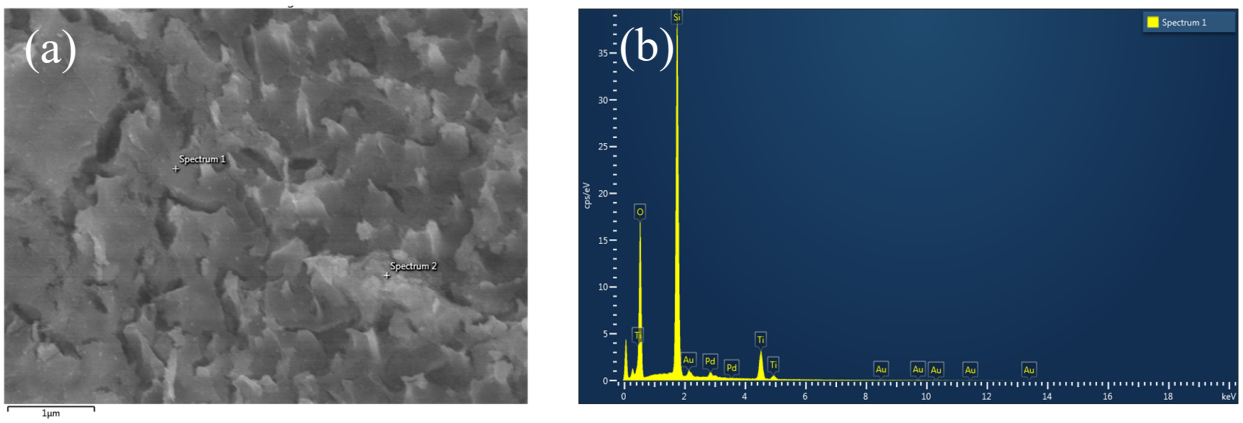

Fig. 34: EDS after second coating confirms that the void between nano grass is filled with TiO2.

Fig. 35 is the transmission recorded by a photo detector as function of different concentration of hydrogen balanced by nitrogen. The experiment was taken under 700 degrees. When the hydrogen is introduced into the system, a drop in the transmission power is observed. The reduced transmission power is in promotional with the hydrogen concentration. Meanwhile, the transmitted power goes up to initial level when introducing nitrogen for 10 min, which helps to reset the sensor back to the previous states. Besides, compared with the drop edge, the resetting process takes longer time. The minimum resolution achieved is 0.2%.

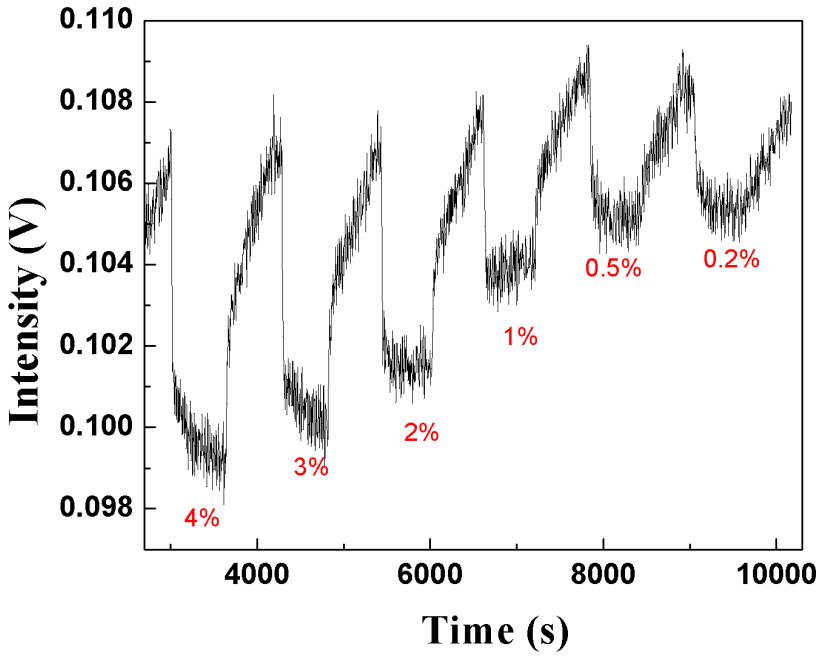

Fig. 35: Transmission power of sensor under different hydrogen concentration at 700 degrees.

3D photonic crystals as sensing platform

Photonic crystals are periodic light scattering structures, with the capability of enhanced light scattering when the period of the photonic crystal comparing to the wavelength matches certain condition. So it will be very interesting to investigate the integration of photonic crystal on to D-shape optical fiber and the possibility to make it a high temperature sensing platform.

In this preliminary study, we continue the work in last quarterly report and try to make the porous 3D POSS photonic crystal be robust in high temperature environment. First, we fabricate the photonic crystal by interference lithography. we mixed epoxy-functionalized cyclohexyl polyhedral oligomeric silsesquioxane (epoxy-POSS, EP0408 from Hybrid Plastics 70wt% in cyclopentanone) with 0.75 wt% photo initiator Cyclopentadienyl(fluorene)iron(II) hexafluorophosphate (Sigma Aldrich) to be the photoresist solution. The solution was spin-coated on the cover slip glass substrates (25mm x 25mm x 170 um) at spin-coating speed of 3000 rpm. Soft bake was performed at 50°C for 10 min. and then 95°C for 10 min. Then a transparent photoresist film was exposed to a two-beam interference setup with incoming laser beam k1 and k2 making an angle of 30° and 8° with respect to the normal of the photoresist film. After the first exposure, the photoresist film was rotated twice for the other two exposures, and the rotation angle is 120°. The laser source is Finesse (from Laser Quantum, a Nd: YAG 532nm CW laser). The output power was set to 3W, and the beam was expanded to about 40mm in diameter, and an aperture of diameter 18mm was applied to choose the central part of the expanded beam for interference patterning. The exposure time was about 1s for each exposure. After exposure, the photoresist film was baked at 50°C for 10 min. and then 95°C for 10 min. Development was done by putting the film in PGMEA (Propylene glycol monomethyl ether acetate, Sigma Aldrich) for 1 hour, and rinsed in IPA (isopropanol, Sigma Aldrich) for 20 min then in DI water for 1 min. Samples were dried in air finally.

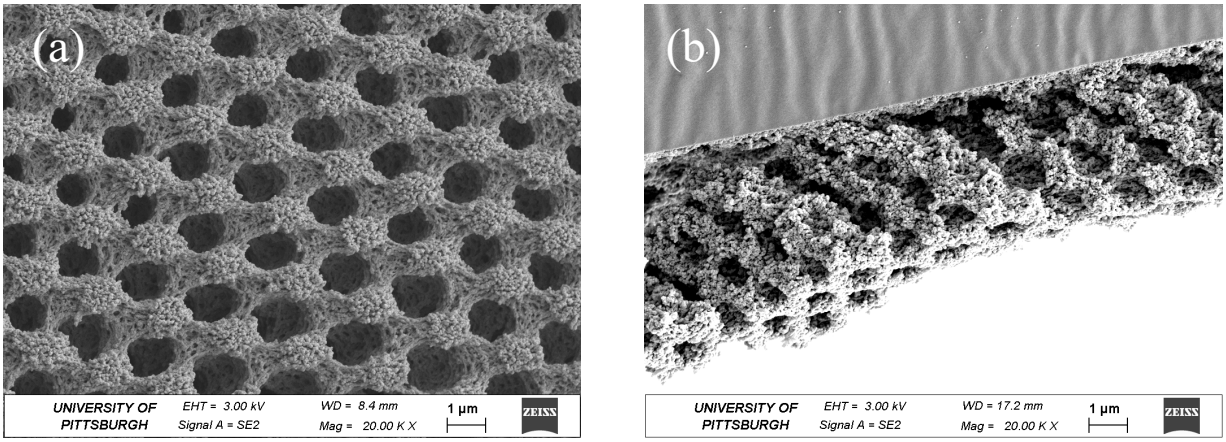

Fig. 36: Top view (a) and cross section view (b) of the HfO2 ALD-coated 3D POSS structure.

Then about 15 nm thick HfO2 conformal coating was formed to wrap the 3D periodic structure by using atomic layer deposition (ALD). With HfO2 coating, the polymeric POSS 3D structure can survive 600 °C annealing in air, and we will test its survival under even higher temperature

later on with proper substrate that can endure higher temperature. Fig. 36 show the top view and cross section view of the HfO2 ALD-coated 3D POSS structure. The micron scale size interconnected air channel let the HfO2 coating deposited on all the positions in the 3D structure, from the top surface to the bottom sitting on the glass substrate. The ALD coating didn't block the porosity in the scale of 100 nm. Energy dispersive spectrum (EDS) in Fig. 37 shows the formation of conformal HfO2 layer on the 3D POSS structure. Note that the morphology looks different under 15kV electron acceleration voltage for EDS to the scanning electron microscope (SEM) image taken under 3kV.

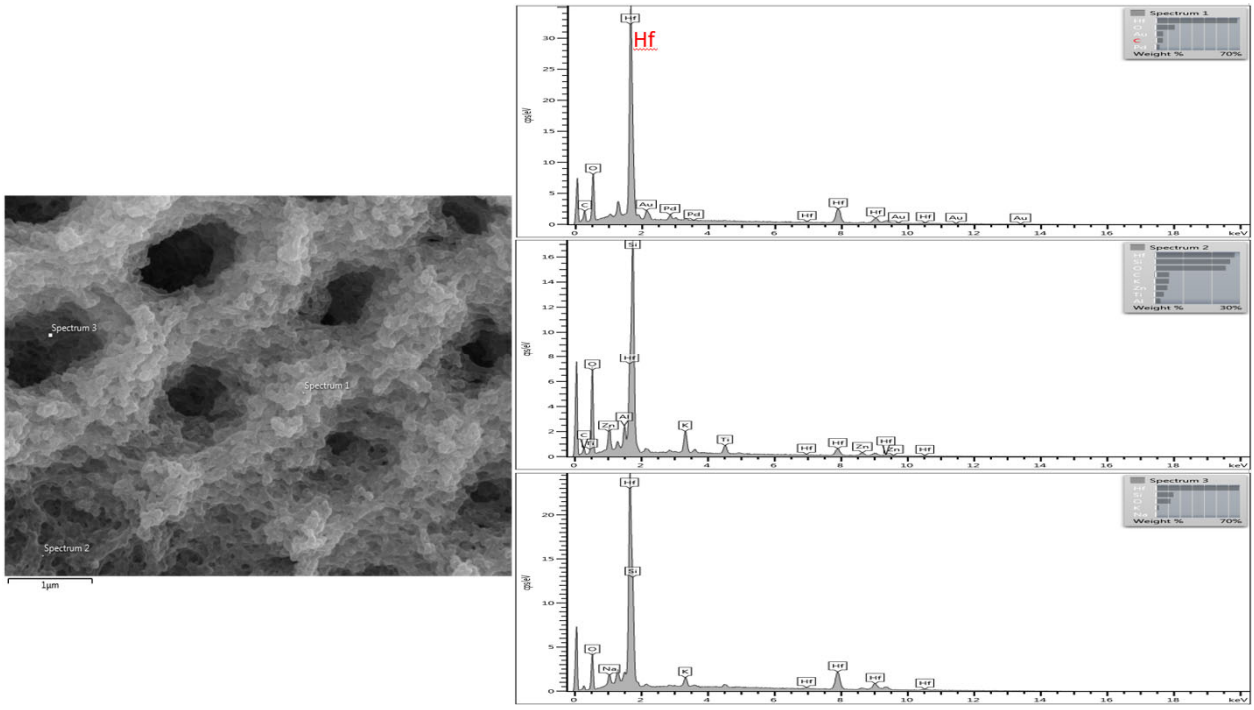

Fig. 37: Formation of conformal HfO2 layer on the 3D POSS structure. SEM image and EDS result for different position confirming the successful ALD coating of HfO2.

To make the HfO2 coated 3D photonic crystal to be a sensory platform, Ti-Pd solution without F127 polymer was coated on the HfO2 coated 3D photonic crystal. Fig. 38 shows the HfO2 coated 3D photonic crystal before and after the further coating of Ti-Pd sol-gel solution without F127 polymer and after annealing under 600°C in air for 1 hour. It's interesting to see that the 100 nm scale porosity of the HfO2 coated 3D structure is filled with TiO2 nano particles after annealing under 600°C in air for 1 hour. So after this step, 3 levels of hierarchical porosity is integrated in the 3D photonic crystal, from the periodic micron size void spaces in the 3D photonic crystal, the 100 nm scale void between the interconnecting POSS particles forming the 3D photonic crystal skeleton, to the 10 nm scale void between the interconnecting TiO2 particles locating between the POSS particles. It's important that with the coating of the HfO2 nano layer, the 3D structure survive temperature as high as 600°C without degradation. We will do higher temperature test later on to see if any other fabrication improvement is needed.

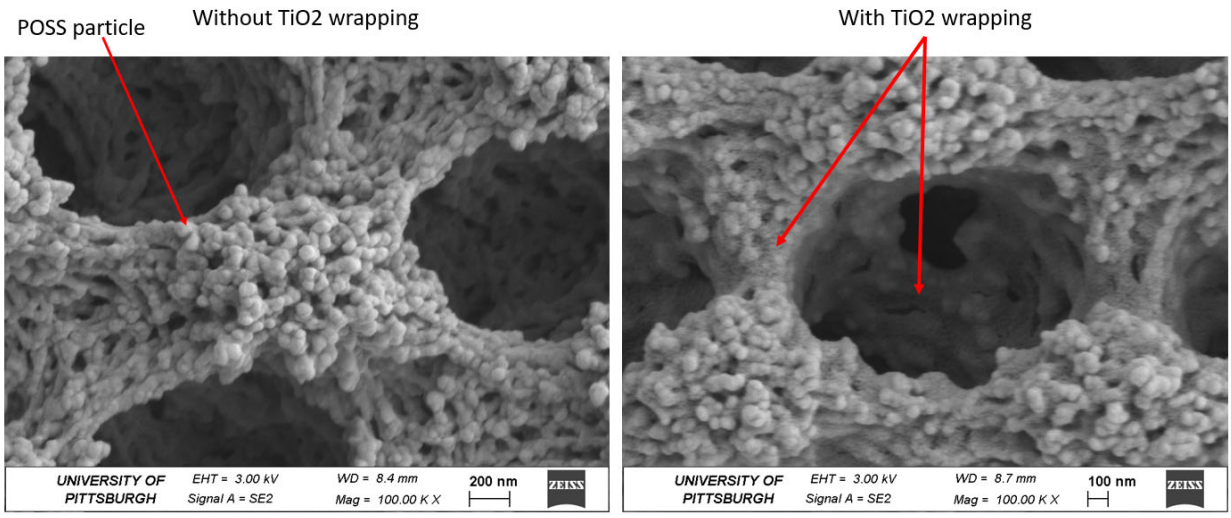

Fig. 38: HfO2 coated 3D photonic crystal before and after coating of TiO2-PdCl sol-gel solution without F127 polymer, and after annealing under 600°C in air for 1 hour.

We also observed that the coating of the TiO2 material could be thin or thick depending on the sitting of the TiO2 solution, as shown in Fig. 39.

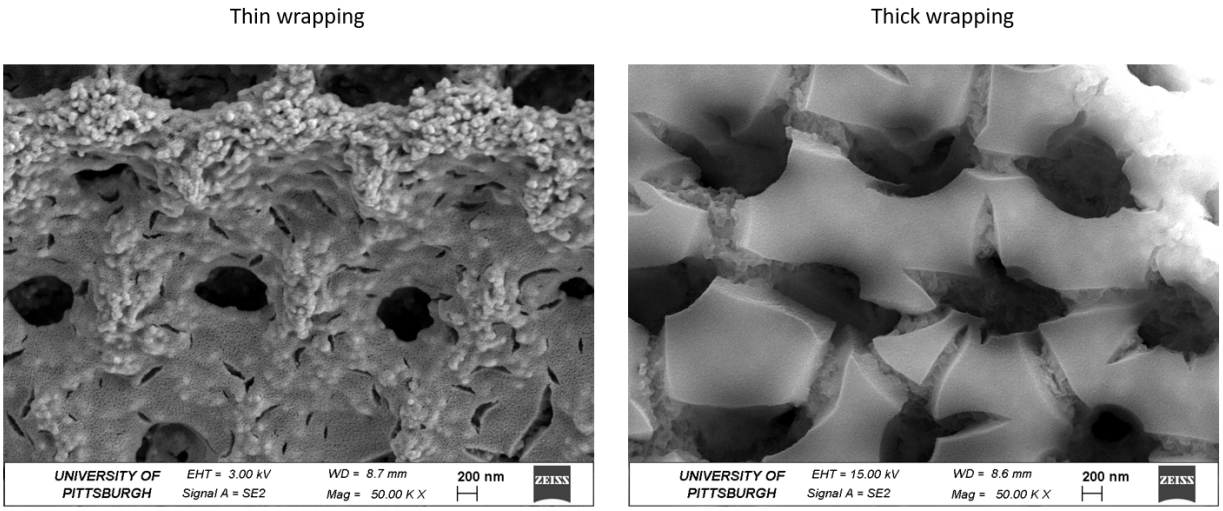

Fig. 39. Comparing thin wrapping of TiO2 at the center of the photonic crystal and thicker coating at the edge.

To confirm the elements in the two wrapping situations, EDS investigation was done and shown in Fig. 38 and Fig. 39 for the thin and thick wrapping respectively. The results show that Ti element is the added one compare to Fig. 35. So in the coating of the 3D structure, we have TiO2 on top of HfO2 on top of POSS.

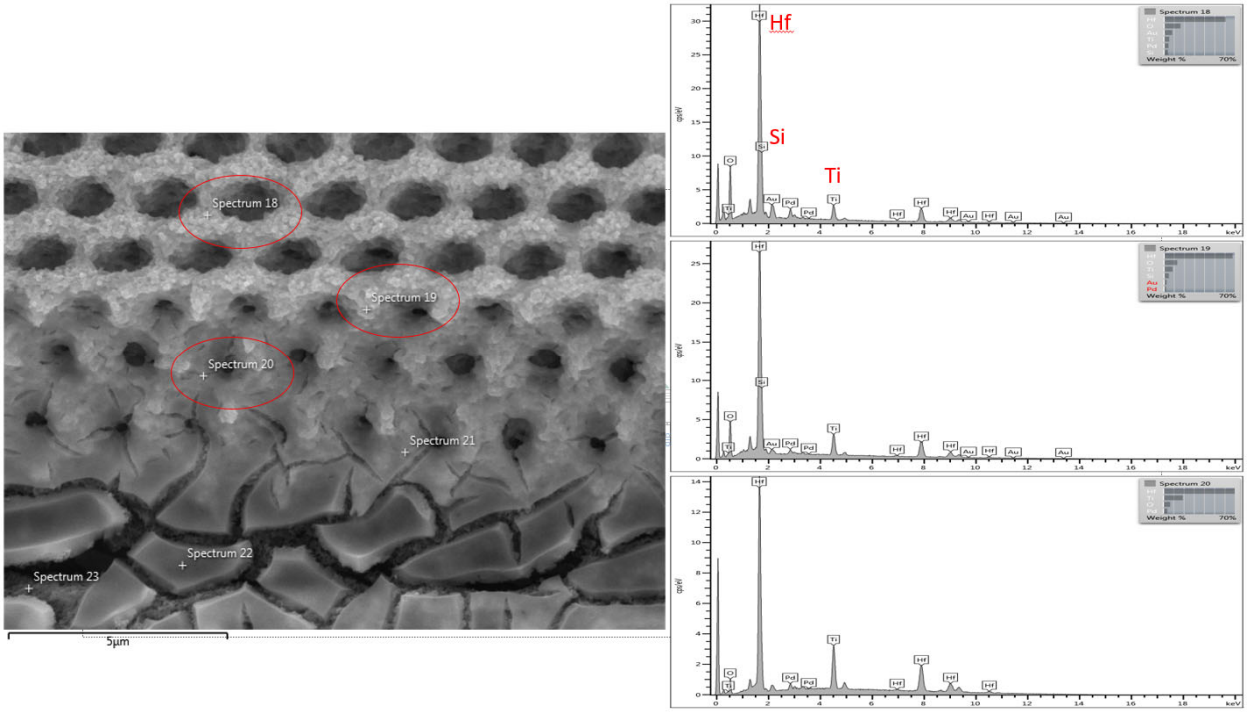

Fig. 40: SEM and EDS result for thin TiO2 wrapping.

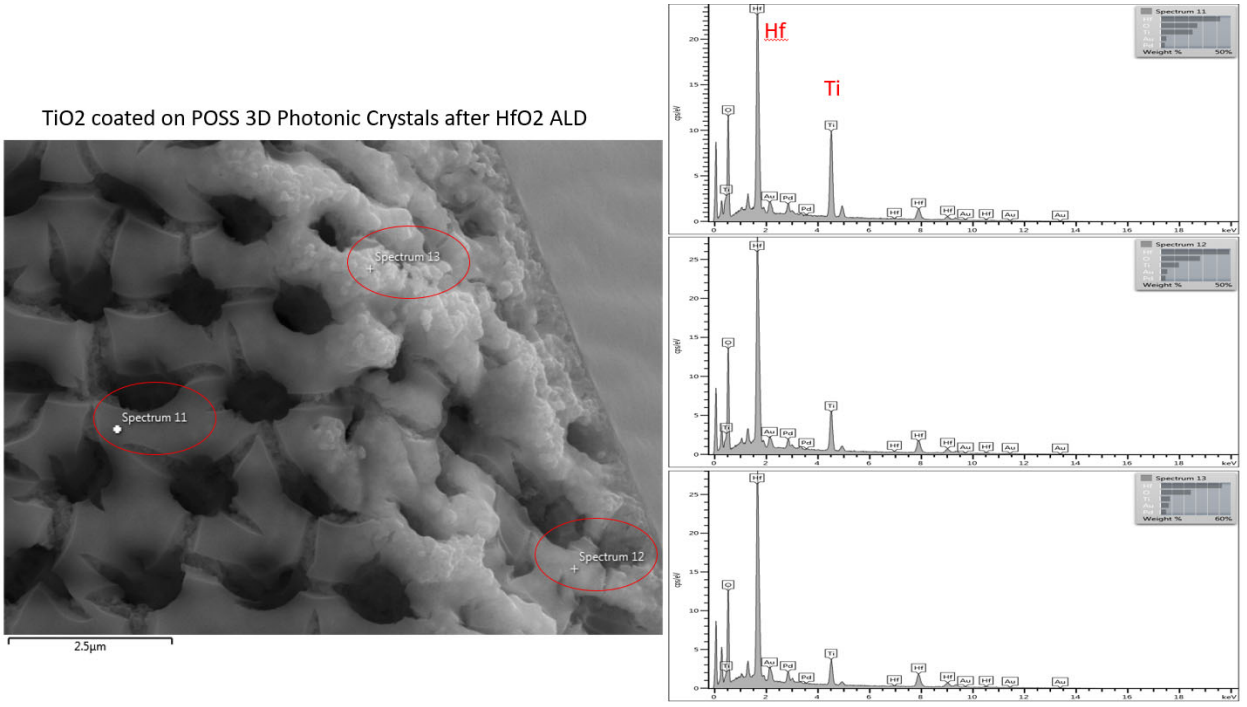

Fig. 41 SEM and EDS result for thick TiO2 wrapping.

We also broke the sample to found that Ti element is indeed inside the 3D skeleton, as shown in Fig. 40-42. This is because of the porosity of the POSS skeleton, the TiO2 solution can fill the void and be trapped between the POSS particles even after annealing at temperature as high as 600°C. This make the inner as well as the outer of the 3D skeleton be sensitive to hydrogen gas.

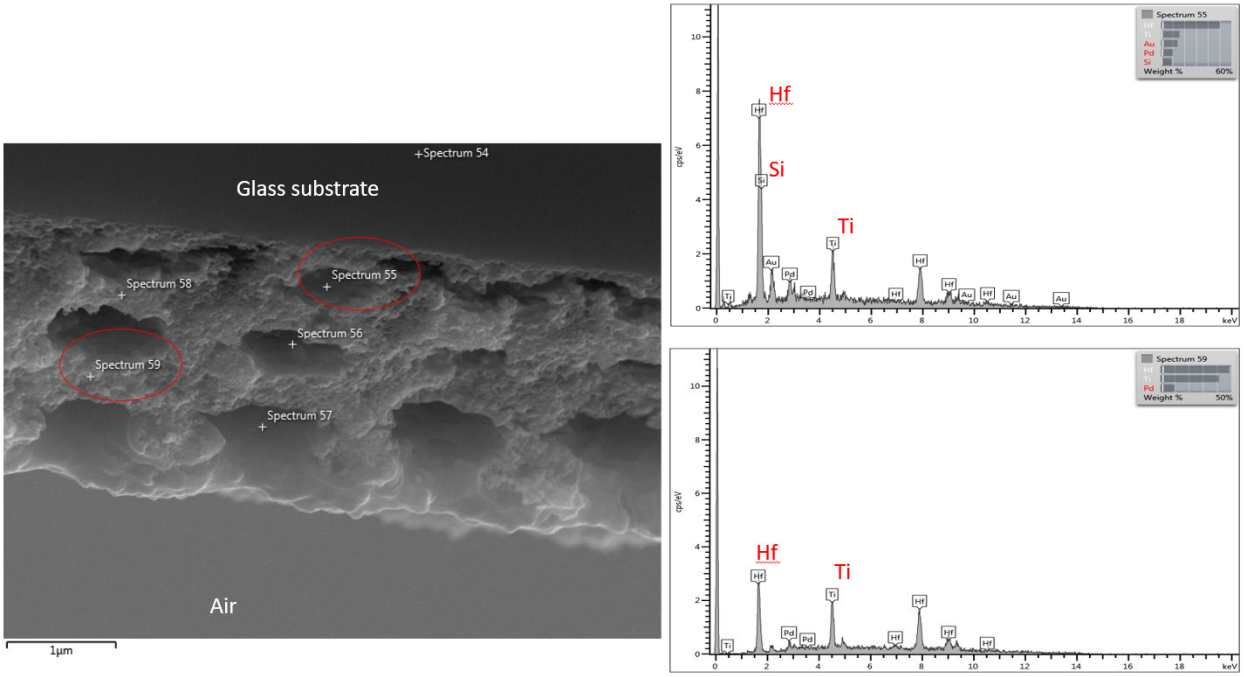

Fig. 42 EDS of the inner of the 3D skeleton after HfO2 ALD and TiO2 coating and annealing under 600°C.

FUTURE EFFORT:

Based on our efforts performed in this period, we will carry out further fabrication and testing works on sensory film formation on nano grass surface of D-shape fiber and 3D photonic crystal integrated on optical fibers.

e. Optimize the RIE recipe for forming sensory nano grass scatter structure.
f. Optimize the TiO2 film forming recipe to achieve smoother film without cracks.
g. Give better sensing result for the nanograss scattering structure.
h. Integration of the TiO2 and HfO2 coated 3D POSS structure to D-shape optical fiber and do sensing tests.
i. Design new optical mechanism and test the sensing property of the TiO2 and HfO2 coated 3D POSS structure to different gases.

Efforts on Developing Distributed Hydrogen Sensor for SOFC Based on Nanostructured D-shaped Silica fibers.

Hydrogen sensors with nanostructure was proved as effective method in improving the sensory response speed indicated by many literatures. So, our effort during this period is to utilize the structure we created to servers as the base for the optical hydrogen sensors.

Most of the nano-sensor reported for the sensing is based on either nanomaterial or nanostructure. The nanomaterial is expensive to fabricate and cannot be applied to the large-scale application. To create the nanostructure, the common methods are electron-beam lithography, electrodeposition into nano-frame, pulsed laser deposition, and electrochemical step-edge decoration. Most of the methods to create nanostructure is a quite complex and time-consuming process. Besides, it has higher demands for the equipment, which inevitably generate more cost. The method we mentioned in the previous report, however, provide a good solution to create nanostructure on fiber with simple process and lower cost. So, the following report will illustrate our recent work of developing a nanocone-based fiber optical hydrogen sensor.

1. NANOCONE FABRICATION.

The detailed nancone fabrication process on fiber (substrate) is illustrated in Fig. 43. Trion Phantom system was employed as the RIE system with the engaging gas of CHF_3, SF_6, and Ar. Chamber pressure was set to be 200 mTorr and the plasma power is tuned to be 100 W. The initial plasma will create polymer on the top of the surface. The polymer is proved to be based on C-F radicals. Those polymers were then served as the mask for the following etching process, which is referred as the maskless process. The cone structures were formed as a result. The size of the cone was controlled by the etching time: with increasing etching time, larger cones forms.

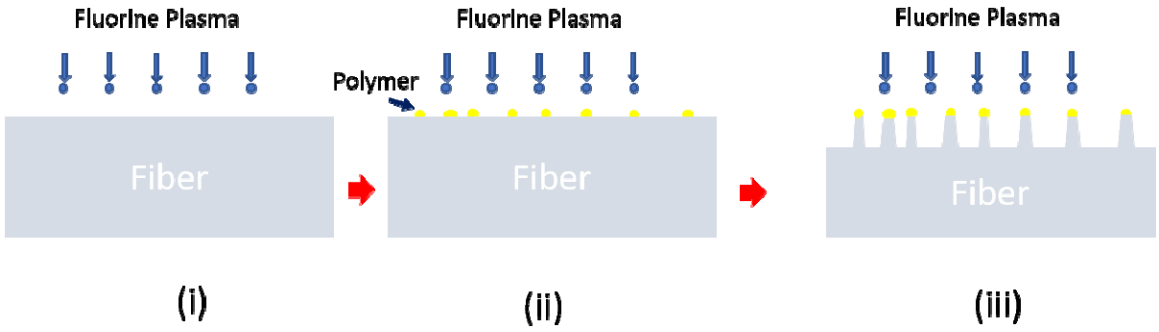

Fig. 43 RIE process in detailed stages.

In this report, the nanocones was formed on the D-fiber with the fiber mounted on the quartz wafer for the etching. D-fiber was special made by Corning with a core diameter of 8.5 μm and the core top to the flat cladding surface of 3.5 μm. The fiber was first cleaned by the solvent (acetone, methanol, and DI water) bath. Then it was transferred to the RIE system for the etching process. After the RIE, the fiber was cleaned again to remove the polymer residue before the sensing film coating. Pd/Au was utilized as the sensing material in this experiment due to its supreme characteristic of the eliminating the hysteresis induced by the pure Pd. Various film thickness was deposited on the fiber surface by the Denton TSC. Chamber pressure was fixed at 5.3×10^{-3}. Argon was being used as the carrier gas during the deposition.

The topography of the sensor was characterized by the scanning electron microscope (SEM) from Zeiss Sigma. Chemical composition of the nanostructures was investigated by the energy dispersive X-ray spectroscopy (EDX), of which the detector was equipped inside the SEM. The cross-sectional view of the fiber sensory is shown in the Fig 44(a). The outlined area is the fiber core with approximately 2 μm being etched away by RIE process. The enlarged image of the core top area is presented in the Fig 44(b) and its inset. As can be seen from the figure, cones with various sizes was formed after the etching. Though different in size, most of cone size was around 50 nm with relative uniform distribution. The height of the cone is around 100 nm. Besides, the gap between cones also various with distance ranging from a few nanometers to almost hundred nanometers. Moreover, the cones appear to be high contrast compared with the fiber underneath, which is due to the uniform distribution of the alloy film on top of the structure. The planarly view of the sensor surface was shown in Fig 44(c). A clearly size distribution was observed in the image with the few large cones of more than 200 nm. Besides, some of the cones has flatter surface than others, which appears to be more like a column instead. EDX spectrum was shown in Fig 44(d) with the accelerating voltage of 10ev. Along with the large amount of the silicon and oxygen atoms, a distinguishable amount of Au and Pd was also observed in the spectrum. This helps to confirm the functionalization of the nanocones with Pd/Au alloy. The two metal elements were mixed with a molecule ratio of Au to Pd 1.2.

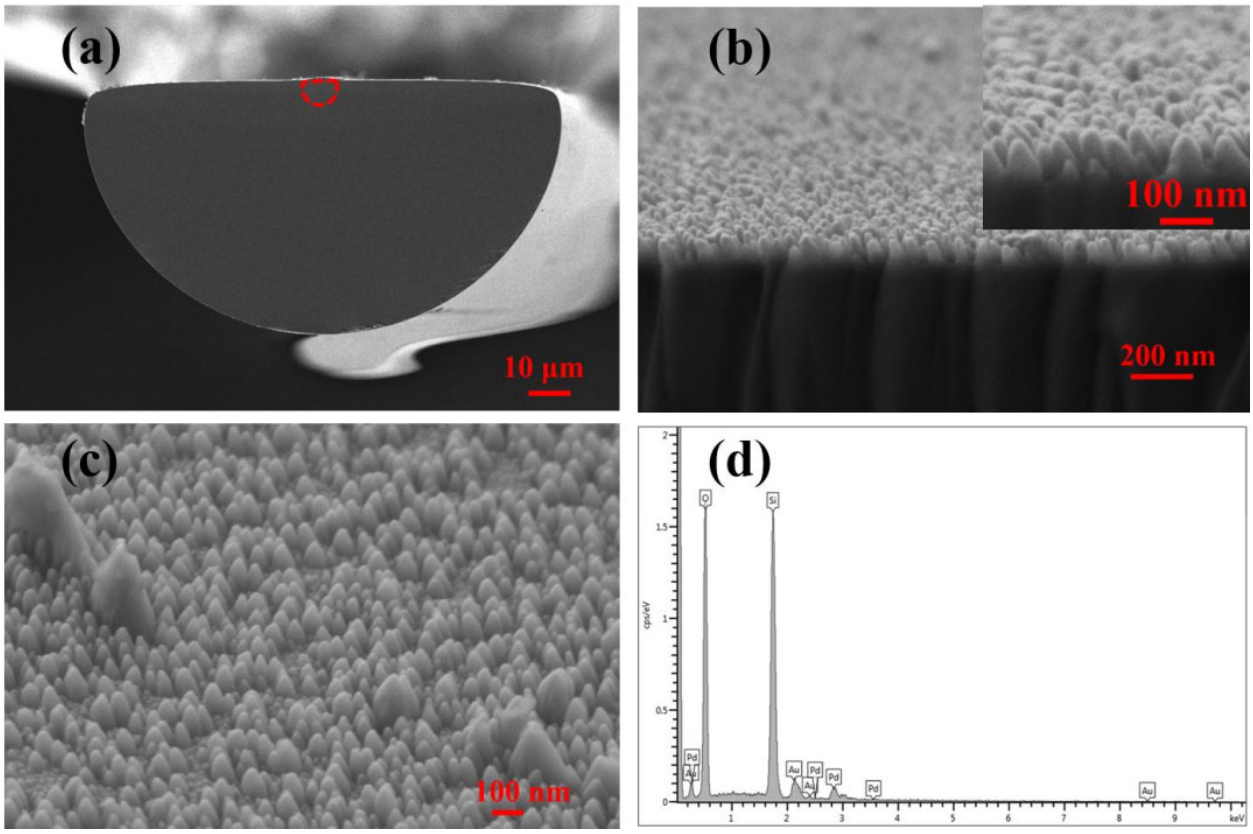

Fig. 44: (a) Cross-sectional view of the sensor, (b) enlarged area of the surface area above the core, inset is the zoomed view, (c) planary view of the sensor surface, (d) EDX spectrum of the nanocones.

The experimental setup is sketched in Fig 45. Broadband source with a wavelength range from 1515 nm to 1615 nm was utilized as the input optical source. Hydrogen was premixture with certain ratio was delivered to the tube furnace which could heat up to 800 ºC. The gas flow

rate was fixed to 20 sccm. Transmitted power was recorded in real time by a InGaAs photo detector connected with a data collecting card.

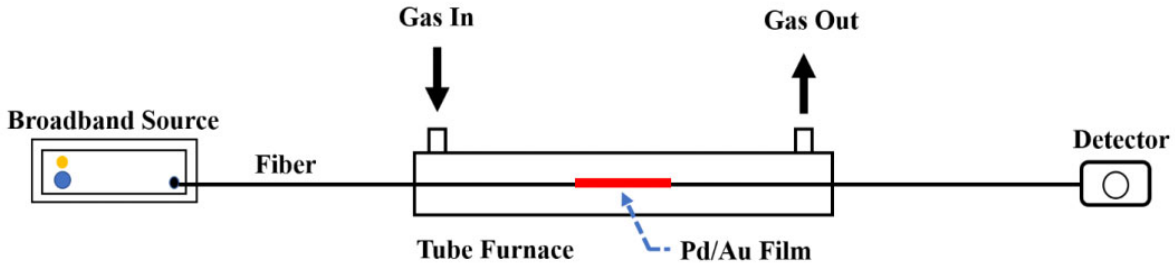

Fig. 45: Sketch of the experimental setup.

The time dependence of the output singal in response to varing hydrogen conecentration at room temperature is shown in Fig. 46(a). The dark line is the response of the reference sensor which has the same sensory film thickness without nanocones. In the experiment, hydrogen gas was being delivered to the tube continously without reseting process with pure nitrogen after each cycle, which has higher requiement of the sensor in sensitivity, stability. It can be note from the image that after servaral cycles, reference sensor without nanocones can no longer differentiate with the other concentrations such as the 6%. What's more, reference sensory profile, compared with the nanocone sensor, is quite noisy with large signal fluctuation under the same concentrations. The response of the sensor with nanostructures (red line) presents a well-defined and smooth signal profile in response to various hydorgen level, which has the benefits for real applications. In fact, stable response with better sensitivity was proved for both electrical and optical hydrogen sensors with nanostructures and nano sensing materials. The instability of the sensory response was mostly due to the mechanical property degradation such as the delamination, buckling, and cracking upon hydrogen loading and unloading. The degradation is the result of the accumulated internal stress. Zhao [47] has improved sensory stability through thermal annealing to release the strain. Nanostructure has been used extensively in the material growth especailly thin film growth to release the internal stress, such as the GaN. Herein, the more stable response of the sensor with nanocone was the result of the factor.

The response time versus hydrogen concentration for the sensor with and without nanocones is shown in Fig 46(b). Inset is the time dependence response of the sensor to 4% hydrogen. It is easy to notice that the response time has been significantly reduced to almost 1/3 -1/4 of the reference sensor. Meanwhile, the huge bump of the response time from 2% to 0.25% was eliminated in the nanocone-sensor. This result agrees well with the previous nanostructure sensor. The underlying mechanism is quite straightforward: the nanocone structure has a large volume-to-surface ratio, which could in turn increase the sensory film area, faciliating the accebility of the hydrogen gas transition and yields more active sites and fast speed for the hydrogen molecure absorption. The gas diffusion time suppose to be the same for both sensors since the coating thickness is the same for both. The larger film area was also confirmed by the more significant transmition power change for the sensor with nanostructure (around 1.2% for nanocone sensor, 0.8% for the sensor without nanostructure) in the inset image.

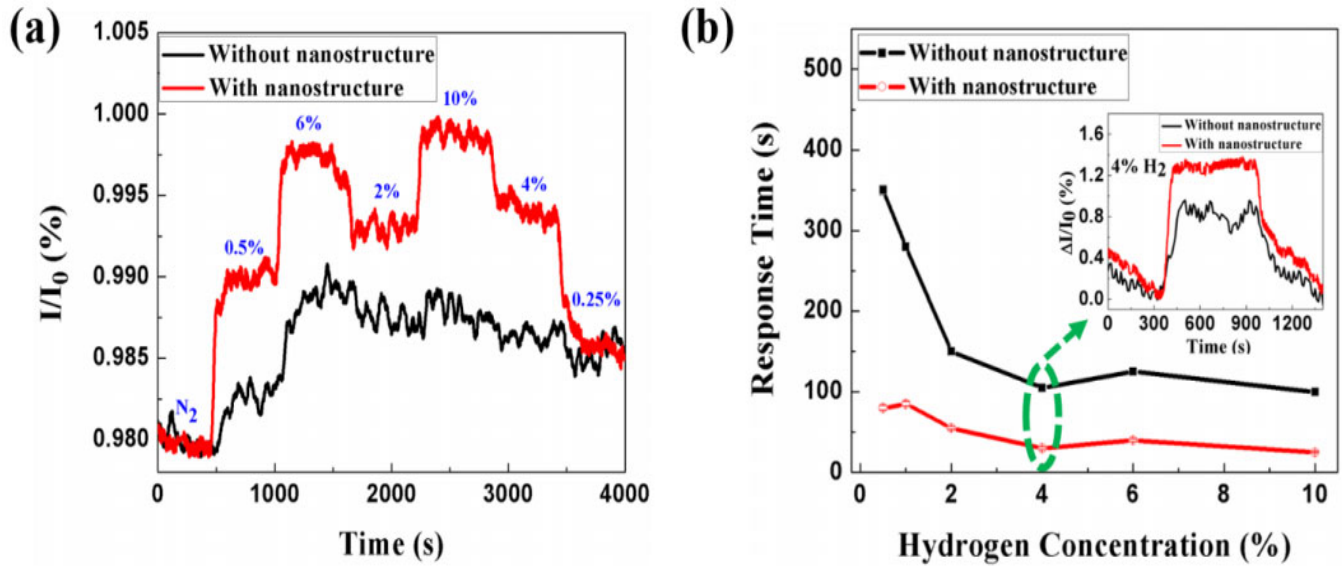

Fig. 46: (a) Response of sensors with and without nanocones to various hydrogen concentrations, (b) Response speed of those two sensors versus the hydrogen concentration. Inset is the time dependence profile of the both sensors to 4% hydrogen.

In addition to the response speed, stable and reversible response are also a non-neglecting factor for gas sensing. To testify the reversibility, a repetitive cycle of hydrogen mixture gas was delivered to the quartz tube furnace at room temperature followed by the pure nitrogen cycle for the sensor recovery. The cycle duty was fixed at 20 min. The response of the sensor with varying hydrogen concentrations ranging from 10% to 0.25% are listed in Fig 47. It is easy to find that there is a sharp drop in the output signal intensity during the initial recovery process and then the rate of the slope starts to slow down, indicating a non-uniform hydrogen desorption rate of Pd hydride. Since there are gaps between nanocones, there are basically two types of sensory film in the sensor: the flat film between nanocones and the film deposited on nanocones. The large surface-to-volume ratio of the sensing film deposited on nanocones, according to the previous results, has a much faster desorption process in comparison with the continuously flat films, which, as a result, dominates the initial signal drop for recovery process. When most of the Pd hydride on nanocone transition is accomplished, the slower desorption rate for the flat films between nanocone gaps starts to become even more noticeable and the slop of the recovery process start to slow down as shown in the image. Meanwhile, it should be noted that the hysteresis phenomenal, which is refer as the irreversible sensory response due to the uncontrolled structural changes, has been drastically eliminated in our sensors as output power almost resets back to its initial level after each 10-min cycle. This improvement of reversibility and repeatability can be account for the utilization of Pd alloy in combination with nanostructures, which could not only avoid the slow Pd-H phase transition process that could result in large mechanical distortion but also reduce the internal stress that could potentially degrade the sensory film mechanical property such as the bucking and detachment effect by insertion of nanostructure layer. In order to further accelerate the recovery speed, the introduction of oxygen or air instead of pure nitrogen could be a better choice according to multiple recent literatures due to the formation of intermitted PdO which act as the intermediate compound and facilities the transition of the PdH.

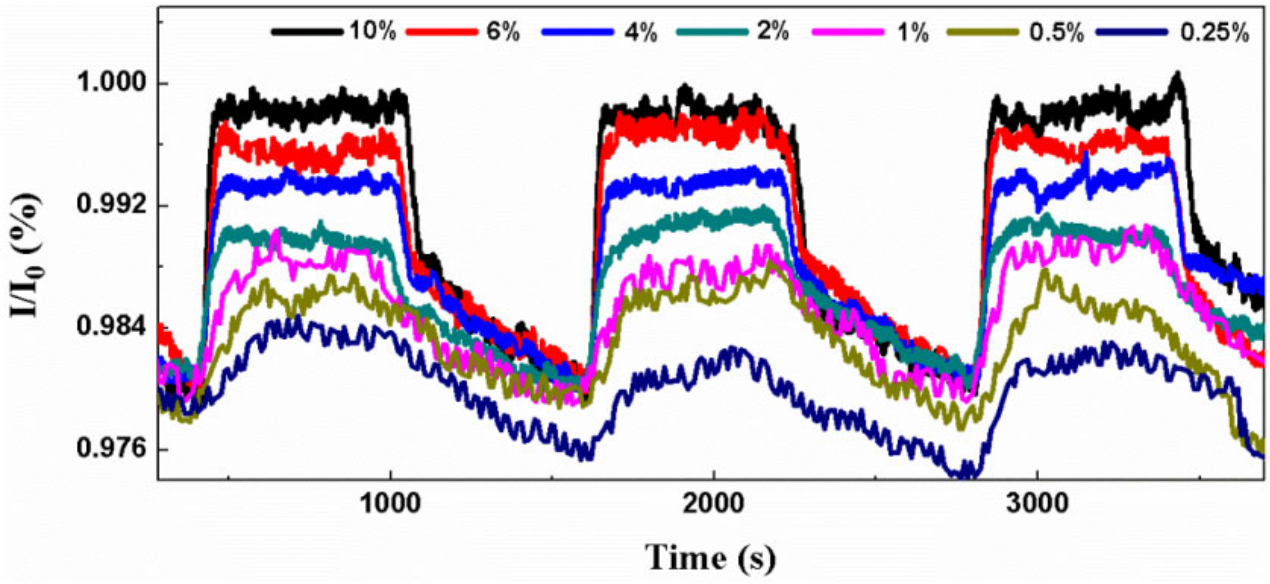

Fig. 47: Repetitive measured sensing response to hydrogen.

The thickness of the Pd/Au film is also considered a major factor in determining the overall sensory behavior regarding to effect of the hydrogen diffusion process. Herein, another two nanocone sensors are fabricated with coated sensing film thickness increased to 30 and 60 nm, respectively. The response speed, same as previous definition, was also referred as the time required for the output power to reach 90% of its maximum change and the result of those two sensors was plotted in Fig. 48 together with 15-nm sensor for more complete compression. As presented in the figure, the response time increases linearly when the sensory film thickness is increased. The observed experimental results are within expectation and in good agreement with other literatures for both electrical and optical sensing scenarios. Compared with other concentrations such as 4% and 10%, there is a sudden jump of the response time for the hydrogen concentration of 6%. As we discussed before, the surface-to-volume ratio can affect the sensory response speed. So the underlying mechanism might partially be due to the reduced surface-to-volume ratio with increasing coating thickness. Since the size of cone is relatively small (100 nm) with short gaps (< 50 nm), the thicker coating such 30 and 60 nm film layer can greatly decrease the average cone gaps, resulting in gradually decreased surface. Another factor worth considering is the diffusion time. For example, thicker film, compared with thinner one, needs longer time for the hydrogen to diffusion through, which will also lead to the overall increased response time. Inset shows the time-varying response of those three sensors to 4% hydrogen concentration. According to the inset, sensor with thinner sensing layer appears to be more stable in response profile in comparison with the thicker ones, which agrees well with the response of the sensor without nanocones in Fig 46, is also due to the enlarged surface area. However, the output power change was found to be increasing with thicker sensing layer. This might be easy to understand since the thicker sensory film provide more Pd sites to absorb the hydrogen to fulfill PdH formation process. Besides, the recovery time also seems to be longer for the sensor with thicker sensory film, which might be due to the increased diffusion time of nitrogen molecule into the film and PdH desorption process.

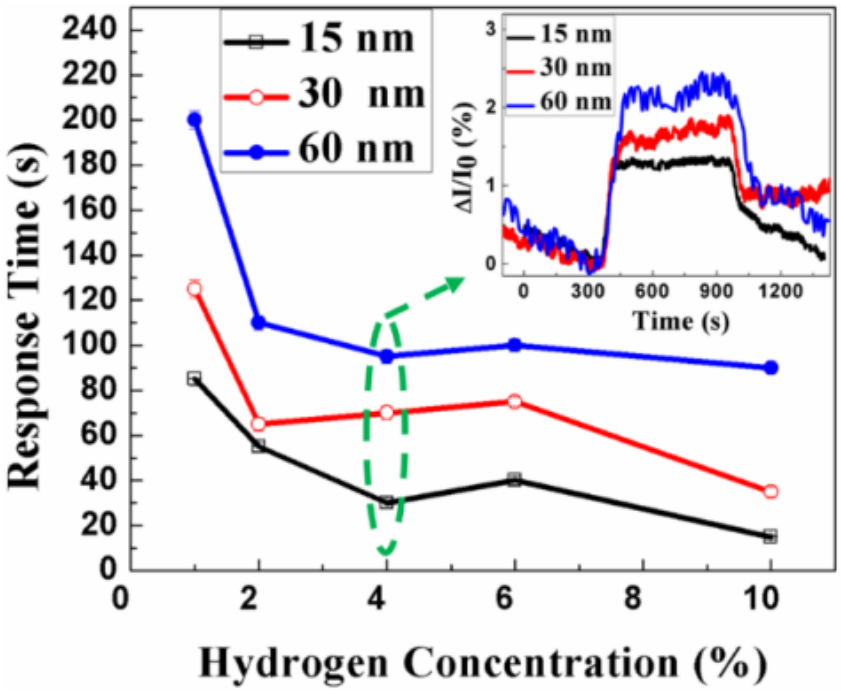

Fig. 48: Response time of three sensors with various sensing film thickness. Inset shows the sensory behavior of 4% hydrogen concentration.

The investigation of hydrogen sensor's behavior under elevated temperatures was also performed in this experiment to study the effect of temperature on the nanocone-sensor behavior. Sensor deposited with 15 nm Au/Pd sensing layer was heated up to 40, 80, and 120 degrees by the furnace with an accelerating rate of 1 degree/min and the time dependence of the output power upon same hydrogen exposure is shown in Fig. 49. A slightly decrease in the output power change is observed under 80 degrees compared with 40 degrees response. This slightly reduction of transmission power with elevated temperature is due to the decrease in the solubility of the Au/Pd sensing film. Meanwhile, the output power of the 0.25% hydrogen increase gradually and the output power mismatch between 0.5% and 0.25 hydrogen become less appreciable with temperature increasing from room temperature to 80 degrees census. To be more specific, when the temperature reaches to 120 degrees, the last two hydrogen cycles response of 4% and 0.25% can no longer be differentiated for the previous response with other concentrations any more, which indicates a degrade of sensitivity and sensory performance. The underlying mechanism might due to severely degraded hydrogen solubility which significantly reduce the active site for the hydrogen absorption. What's more, another possible reason is the increased internal strain that accumulate during the loading and unloading process of hydrogen gas, which, as mentioned before, can degrade the mechanical property such as the declamation and bucking of the sensory film that leads to reduced ability of the sensory film that cannot no longer proper response to various the hydrogen concentration change after several successive cycles of testing.

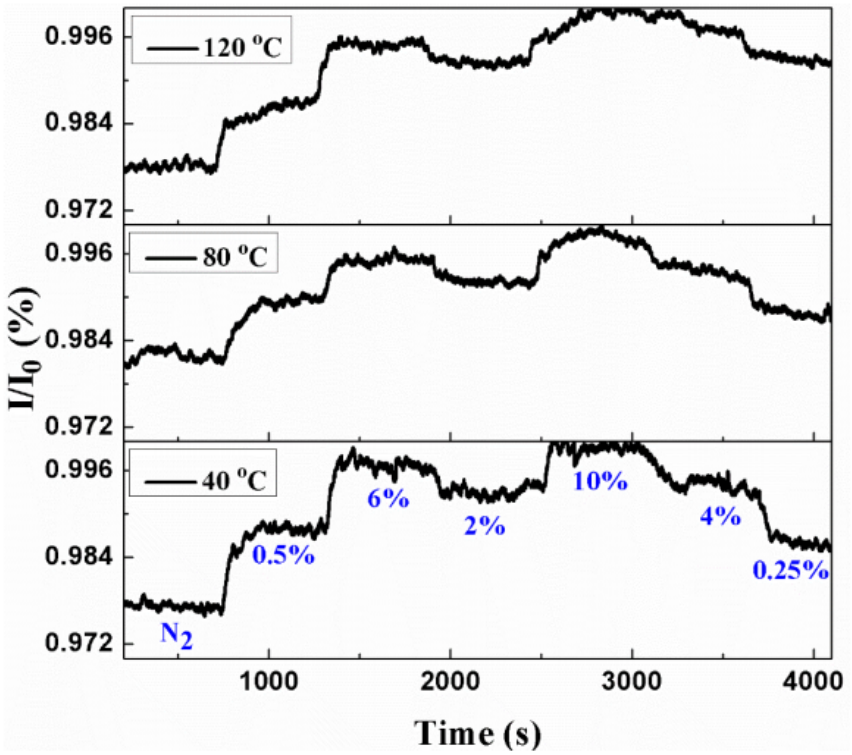

Fig. 49: Sensory response at elevated temperature with the same hydrogen concentration.

To summarize, we fabricated nanocone structures on D-shape fiber and functionalized them with Pd/Au alloy film for fiber optical hydrogen sensing. In comparison with reference sensor with without nanocone and with continuously sensing film, sensor with sensing film coated on nanostructures achieves more stable responses as well as much shorter response time. Besides, the sensor also appears to be more reversible in response compared with the reference one. Furthermore, response speed was also proven to be in proportional to the sensory film thickness, and thinner film could benefit the sensory behavior. Elevated sensing temperature was also studied and proved to affects the sensor stability. Our nanocone optical fiber sensor presents a new and convenient approach to fabricate nanostructure on optical fiber for gas sensing, which makes it an attractive candidate to increasingly diverse optical fiber sensing scenarios to improve the sensory response speed and overall performance for sensing.

Efforts on Optimization of Nanograss Structures for Hydrogen Sensing

Optimization of Nanograss structure on D-fiber for Hydrogen (H_2) sensing.

In the previous quarter, we have shown that nanograss structures on top of D-fiber can enhance the scattering signal, at the same time, it can increase surface area for the gas sensor operation measured by OBR (Optical Backscatter Reflectometer). However, higher scattering means greater the loss of signal. Therefore, optimization of nanograss morphology in term of porosity, pore sizes, and 3D structures for the nanograss are very important for the purpose of sensitive gas sensing.

In this quarter, we conducted etching experiment to study the height and diameter of the nanograss, and distance between nanograsses obtained from varies RIE (Reactive Ion Etching) etching time. We used Trion Phantom III LT RIE. The recipe of the RIE was as follows: CHF_3 50 sccm, O_2 5 sccm, chamber pressure 50 mT, RIE power 150 W. Etch time tested were 90, 50, 25, 15 and 5 min. SEM was used for observation and measurement as shown in Fig. 7-1 to Fig. 7-5 for each etching time, respectively. The circle in the SEM indicates the position of the original fiber core.

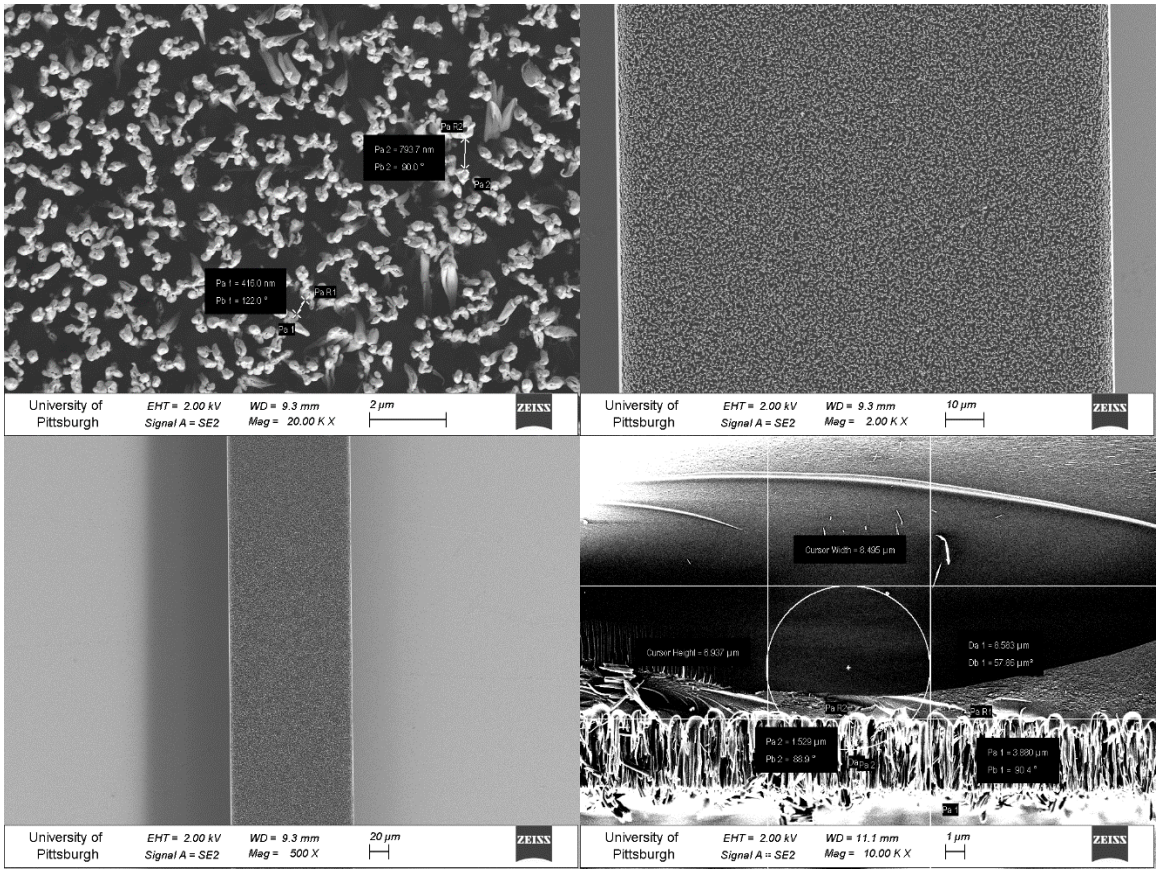

Fig. 7-1: SEM images of D-fiber after 90 min RIE, top and cross section, with measurement.

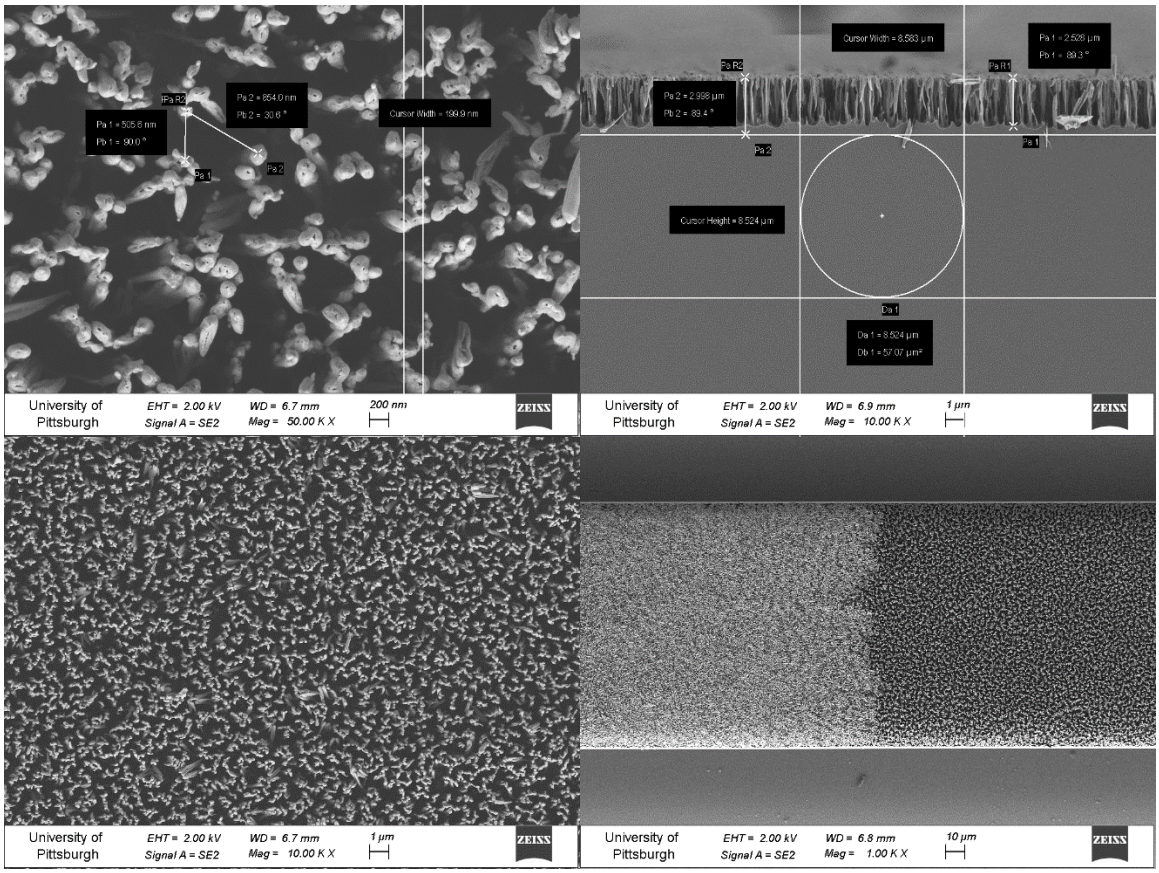

Fig. 7-2: SEM images of D-fiber after 50 min RIE, top and cross section, with measurement.

The D-fibers in Fig. 7-1 and Fig. 7-2 were placed into RIE directly after peeling off the fiber's protective polymer coating. The cross- section view shows that, by RIE 90 min, the root of the nano grasses already reach the fiber core, showing a deep etching with 3800 nm height of nanograss. While, for RIE 50 min, the root of the nanograss was about 470 nm above the top of the core. The height of the nano grass reduced to about 2500 nm.

However, nanograss with height above 2000-nm didn't give good sensing behavior as shown in our sensing test. This suggested that we should shorten the nanograss, while keeping the nanograss at the vicinity of the core so that evanescent wave can interact with the gas-sensing material (reduced TiO2-PdCl2 in H2) that penetrates the voids in between nanograsses. We found that we can use buffered HF solution to wet-etch the fiber for 16 min to reduce the thickness of cladding on the flat side of the D-fiber, to make the cladding-air interface to be about 500 nm on top of the fiber core. Base on this, we further conducted RIE for 25, 15 and 5 min, as shown in Fig. 7-3 to 7-5. It shows that the height of the nanograss was reduced to 884 nm, 488 nm and 83 nm, respectively.

At the same time, the heights, diameters and distances between the nanograss of different RIE time are reported in Fig. 6 together. Through controls of etching time and reactive gas recipes of RIE process, we can achieve thorough control of nanograss height, porosity, and pore size. This provides significant flexibility in controlling gas sensor's performance.

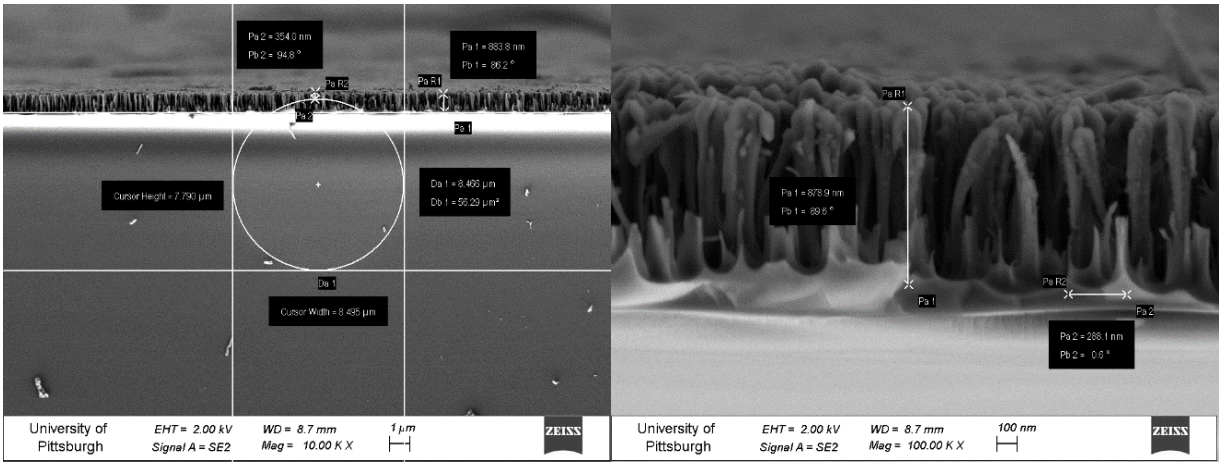

Fig. 7-3: SEM images of D-fiber after 25 min RIE, cross section with measurement.

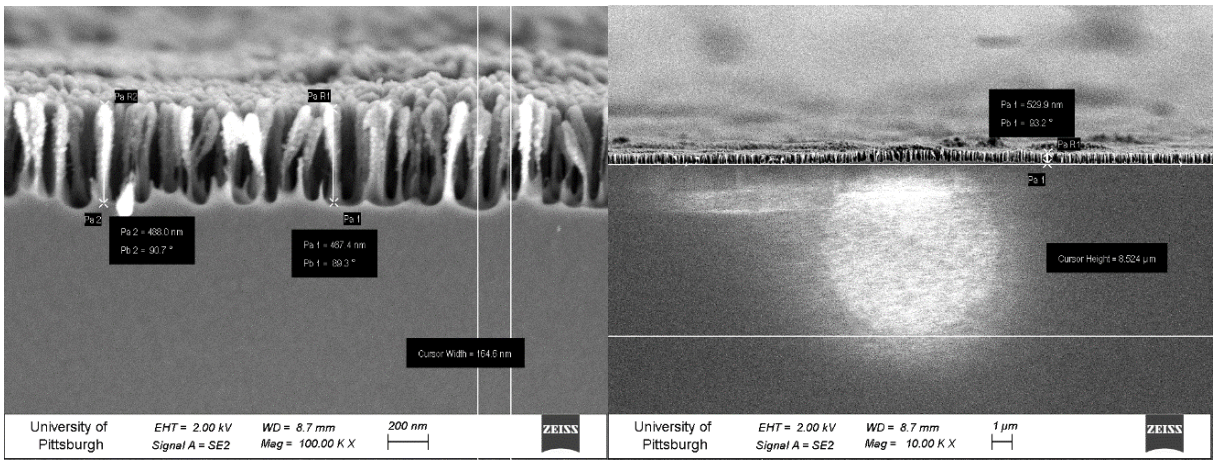

Fig. 7-4: SEM images of D-fiber after 15 min RIE, cross section with measurement.

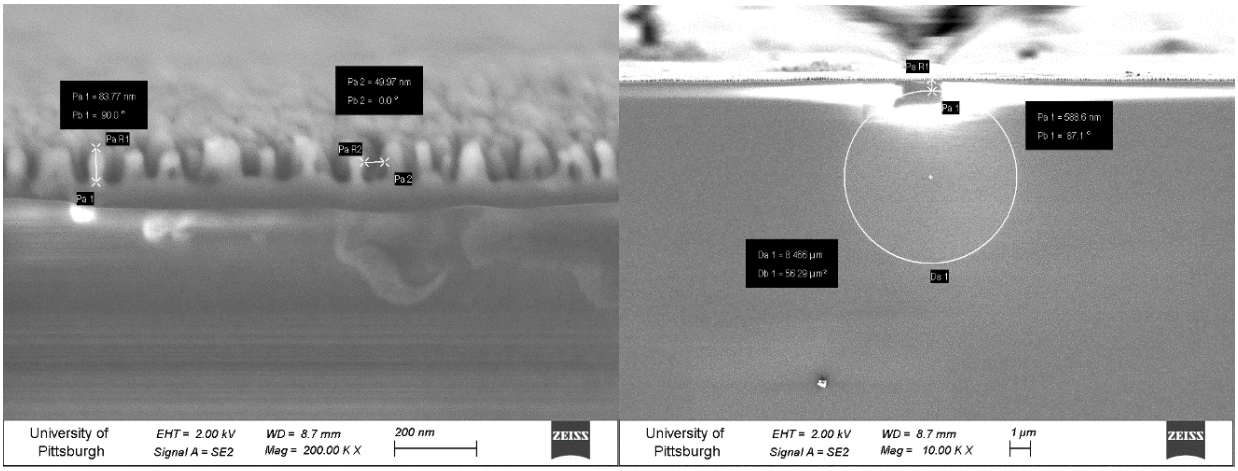

Fig. 7-5: SEM images of D-fiber after 5 min RIE, cross section with measurement.

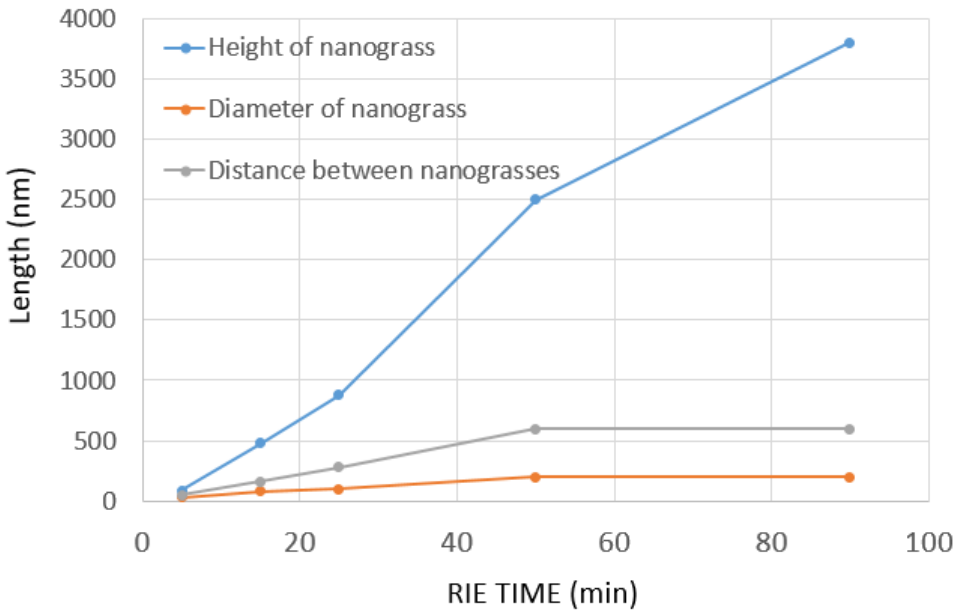

Fig. 7-6: Height and diameter of the nanograss and distance between nanograsses obtained from varies time (min: 90, 50, 25, 15, 5) of RIE etching.

Since the tall nanograss didn't yield good sensing result, we further choose the one etched by 15 min RIE to perform the sensing test. To fabricate hydrogen sensor Pd-TiO_2 sol gel solution were used. The solution was the same as that in previous quarterly report (using the clear part of the solution). The solution was also diluted to 25% in volume using ethanol to achieve optimal dip coating outcome. The etched fibers were dipped coated in sol gel solution for 30 minutes. After coating, the sample was let dry in air for one day, and then put in oven with air atmosphere for thermal treatment. The temperature variation and duration is shown in Fig. 7-7.

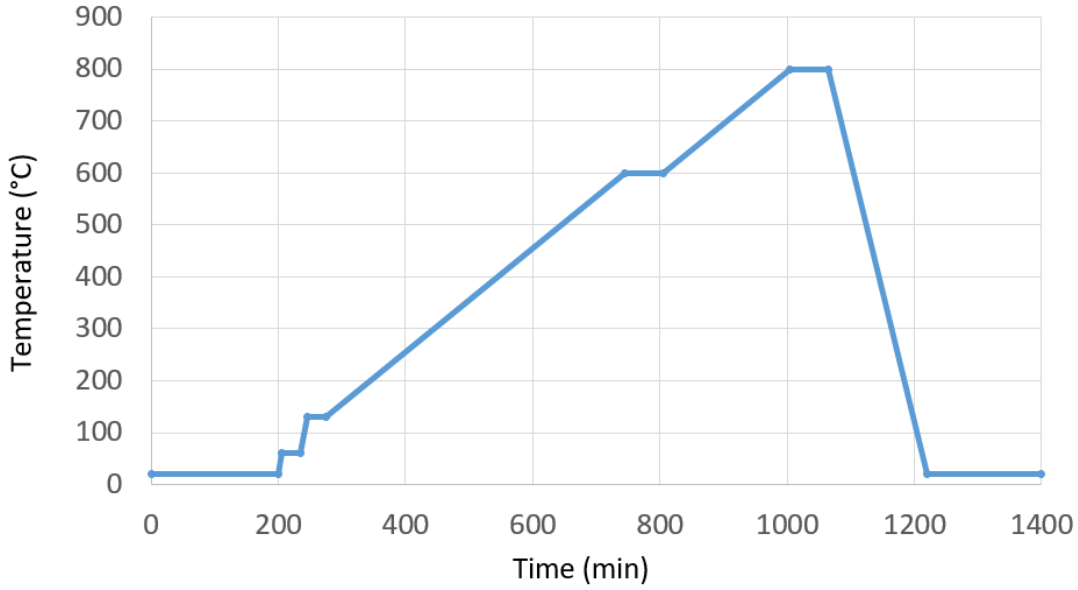

Fig. 7-7: The temperature variation and duration of the thermal treatment.

The resulted Pd-TiO_2 sol gel film was then observed by SEM, with top and cross section views shown in Fig. 7-8. The highest temperature the film experienced was 800°C for 1 hour. Fig. 7-8 shows that the film is uniformly formed on top of the RIE D-shape fiber with good penetration of TiO2-Pd particles in between nanograss structures. The coating and infiltration of Pd-TiO_2 also preserve overall porous structures after the film sintering at 800ºC in air, which burn out the F-127 templating co-polymer at high temperatures. With only a few cracks appeared, the top view of the result also shows good quality of sensory film formation on top of such RIE nanograss surface based on D-fiber as shown in Fig. 7-8.

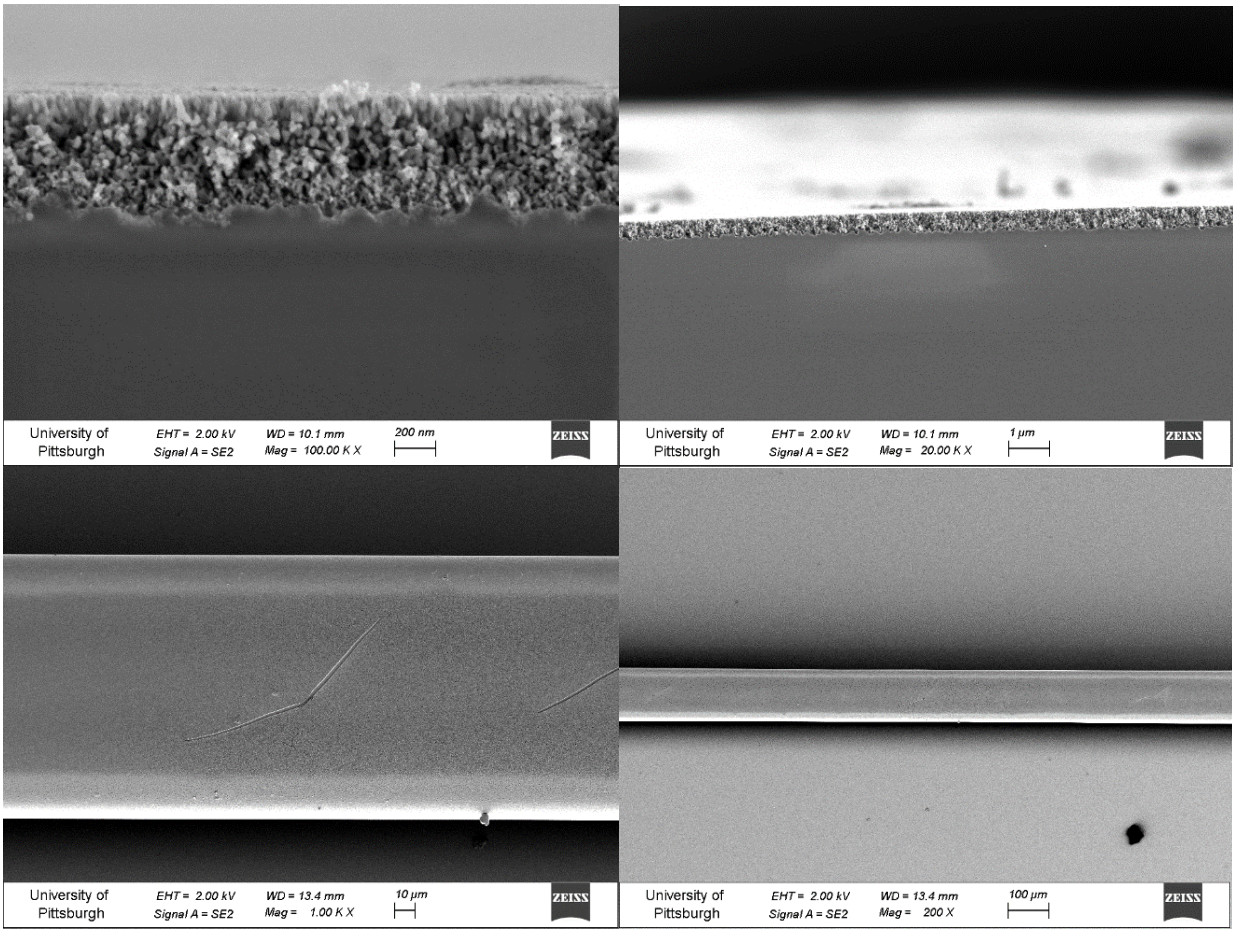

Fig. 7-8: SEM images of high-temperature treated D-fiber with nanograss coated by diluted TiO2-PdCl2 solution.

In the previous report, we have developed a distributed hydrogen sensor based on the surface-textured D-fiber functionalized with Pd-doped TiO2. To enhance the sensor performance, efforts invested in this quarter optimized nanostructure sizes, porosity, and overall shapes as shown in Fig. 7-1 to Fig. 7-5 and Fig. 7-8 above. Another factor limiting the sensory response is the distribution of sensory film coated on the flat face of the fiber. In this report, we demonstrate our effort to optimize the sensory film coverage first.

Meanwhile, the Pd concentration is another factor worth investigating since it not only determines the sensor's ability to absorb the hydrogen molecule but also affects the sensing

film's optical properties such as the refractive index, which in turn, affects the sensory performance.

Fig. 7-9 shows the topography of the sensor with and without using diluted sol gel solution to form the sensing film. In the Fig. 7-9(a), large chucks of the Pd-TiO_2 was observed on top of the nanostructure on top of the fiber. Those large chucks appear to be results of the disassemble of the whole sensory film after the pre-heating and Pd-exchanging process indicated by the large cracks. In contrast, the films penetrate through the gap of the nanostructure and forms a uniform distribution on top of the textured surface as indicated in the Fig. 7-9(b). Inset is the enlarged image of the plane view. The cross-sectional view of the sensor is shown in the Fig. 7-9(c). The film appears to be quite uniform across the whole fiber with the coating thickness around 600 nm.

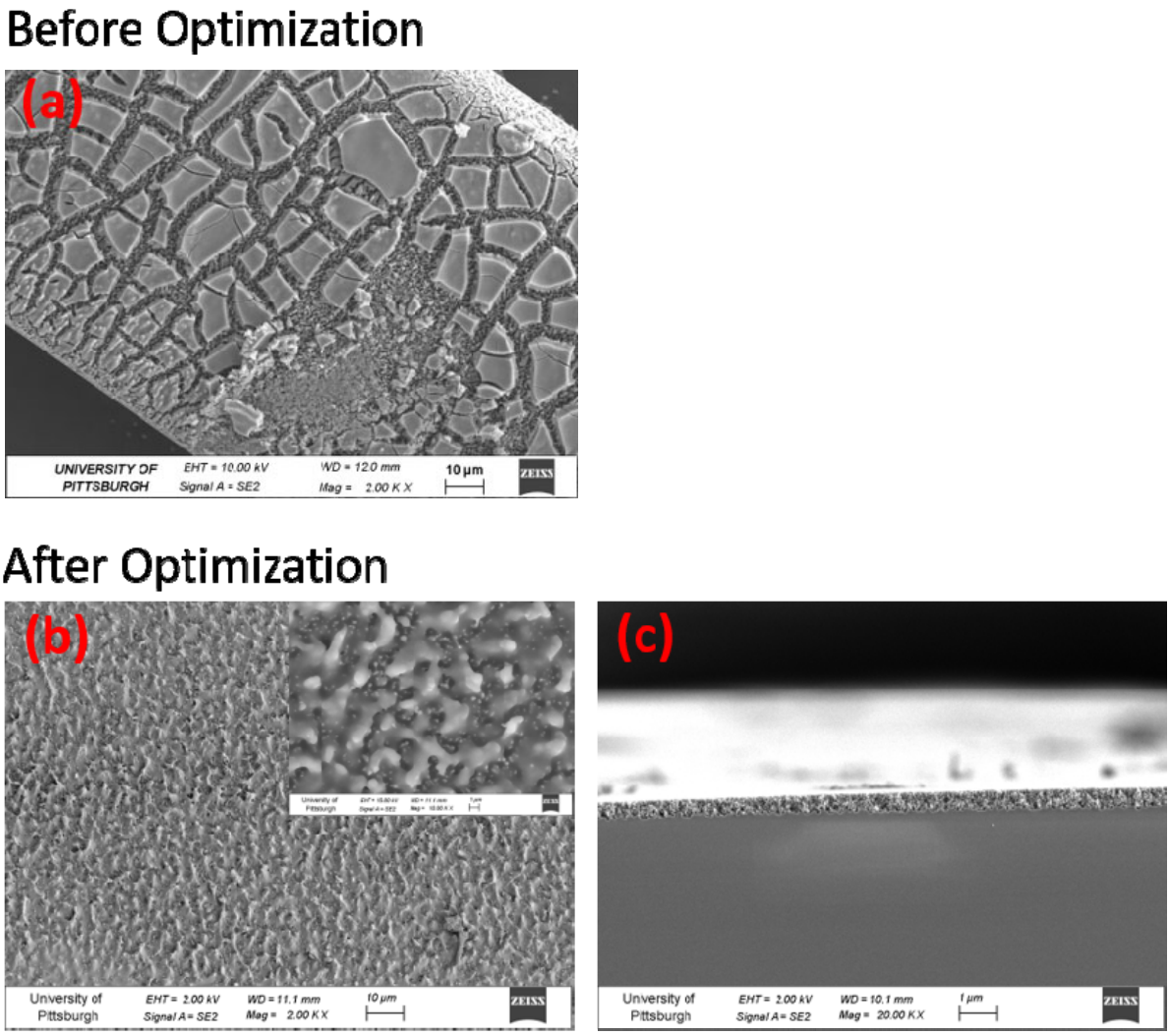

Fig.7- 9: The SEM image of the (a) sensory film without dilute, (b) sensory film with 4 times dilution, (c) cross-sectional view of the sensory with 4-times diluted solution

Summary: In this period, we made efforts to optimize nanograss structures directly fabricated on optical fibers to enhance Rayleigh backscattering and increase surface volume for subsequent Pd-TiO_2 sensory film developments. We have shown that through processing optimization, the pore size, height, and overall porosity can be controlled through reactive ion etching recipes and etching times. The topology of nano-grass structures has impacts on optical loss and Rayleigh scattering properties of optical fibers. Through diluting of sol gel film, we have achieved thorough infiltration of Pd-TiO_2 sensory film, which will lead to improved performance of optical fiber sensors. In the following report, we are discussing the impact of the distributed sensory profile when increasing the Pd level in the sensor to 2 and 4 times, respectively.

Section 8: Detail Report for 2018-Q4 Efforts

8.1: Optimization of Nanograss structure on D-fiber for Hydrogen (H_2) sensing.

In the previous reporting period, we have shown that nano-grass structures on top of D-fiber can enhance the scattering signal, at the same time, it can increase surface area for volume for subsequent Pd-TiO_2 sensory film developments. In this quarter, we studied the impact of the distributed sensory profile when increasing the Pd level in the sensor to 2 and 4 times, respectively. In our experiment, Optical backscattering reflectometer based on Rayleigh-backscattering OFDR system shown in Fig. 8-1 was utilized to quantify the distributed sensory performance in response to different methane levels. The experiment was carried out at 750 ℃ with a fixed gas flow of 20 sccm.

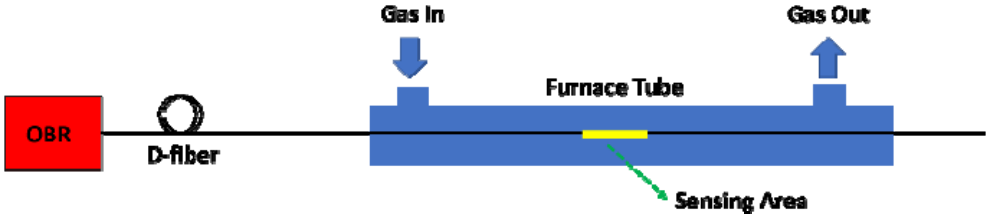

Fig. 8-1. Schematic diagram of experiential setup.

The experimental results are shown in Fig. 8-2. It is easy to notice that a well distributed sensory response profile is achieved for the Pd element concentration of 1 and 2 time of previous level. The hydrogen response carried out at this temperature show a more differentiable responses form 1× increase of Pd element concentration in sol gel film. All of these results were obtained on nanograss structures with 500-nm height, which were achieved after 15-minute reactive ion etching processing as shown in the previous quarterly report (Fig. 7-4 and Fig. 7-6).

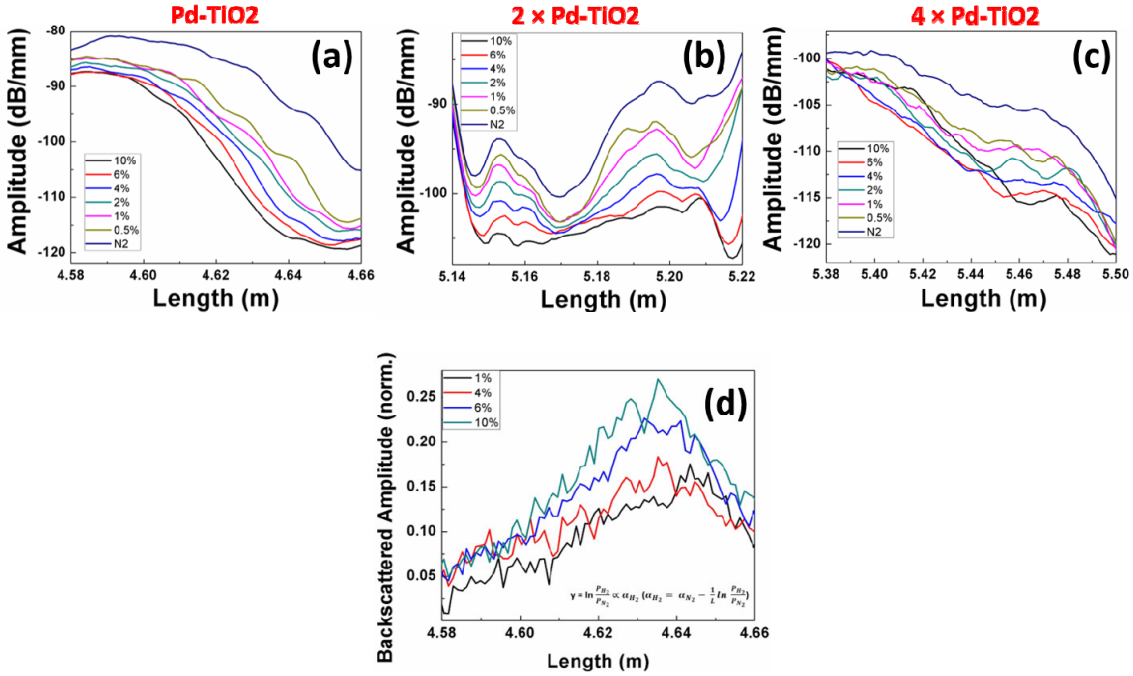

Fig. 8-2. Distributed sensory profile in responses to various methane concentration when the Pd is (a) original level, (b) 2 times, (c) four times, (d) absorption rate distribution

However, when further increase the Pd concentration to 4 time, a significant degradation of the sensory performance is observed, which is indicated by the intertwined signal response that no longer differentiate hydrogen levels between 0.5% and 6%. The deteriorated sensory response might be due to the increased refractive index that generates more absorption and loss than Pd-absorption/desorption of hydrogen, this is because Pd nano-particle has significantly higher refractive index compared with TiO_2.

Since our sensor is absorption based. According to Beer-Lambert Law, the absorption rate is in proportional to the logarithm of the output signal of the hydrogen to nitrogen reference. The processed data is shown in Fig. 8-2(d). The absorption rate is supposed to be uniform across the fiber if the sensory material is uniform. However, we saw an initial linearly increase in the absorption rate and then it gradually decreases, which might be due to the nonuniformity of the sensor during the manufacturing process. It is also worth noting that the absorption rate at different hydrogen concentrations can be differentiated with a resolution up to 1%. This is more than sufficient for fuel cell application where fuel concentration is run between 5% to 100%.

The time dependence response of the distributed sensor was also being explored at various hydrogen concentrations and the related nitrogen resetting cycles. The results are shown in the Fig. 8-3 and Fig. 8-4. In Fig. 8-3, the sensor appears to be more responsive at high hydrogen concentration as indicated by the more significant drop of signal at 2 min and the sensory profile lines of various concentration beyond 2 min tends to bundle together as the concentration was further increased.

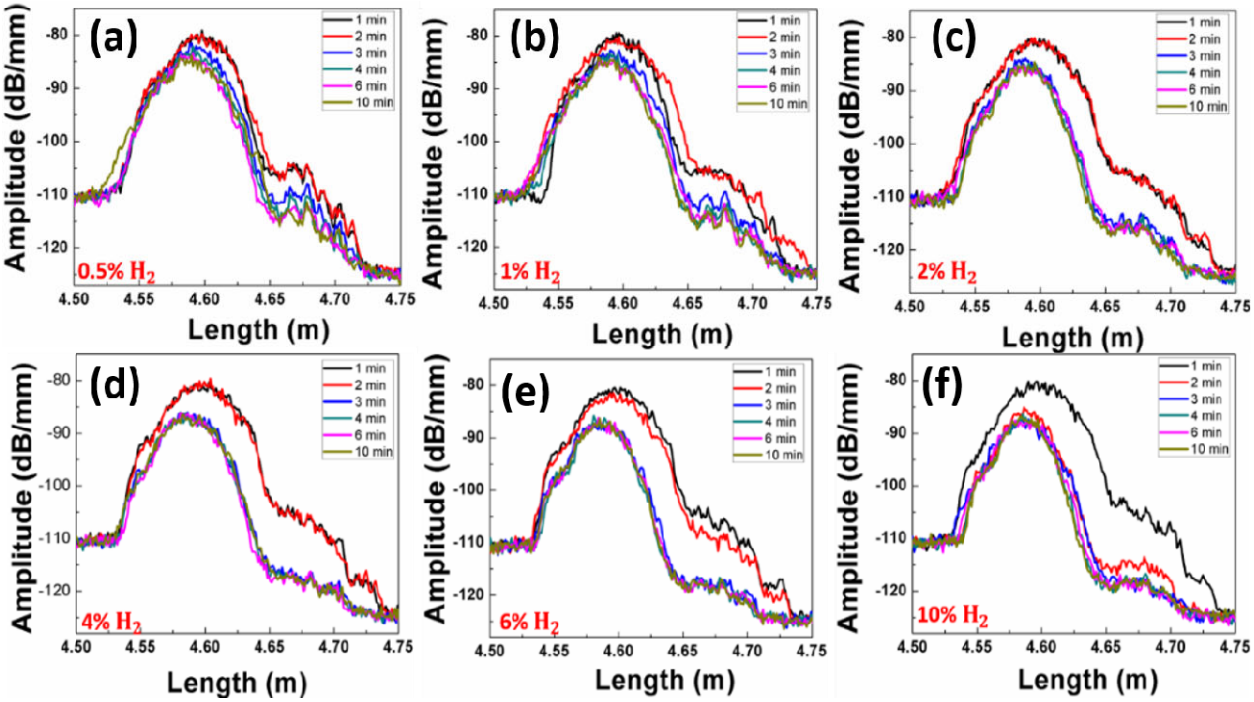

Fig. 8-3. Time-dependence response of the sensor to various hydrogen concentrations (a) 0.5%, (b) 1%, (c) 2%, (d) 4%, (e) 6%, (f) 10%.

Meanwhile, in the Fig. 8-3, the time-dependent response of sensor during the reset cycle after varied hydrogen was also studied to investigate the resetting cycle behavior. It is easy to notice that the initial resetting speed for the higher concentration hydrogen is also faster than the lower one.

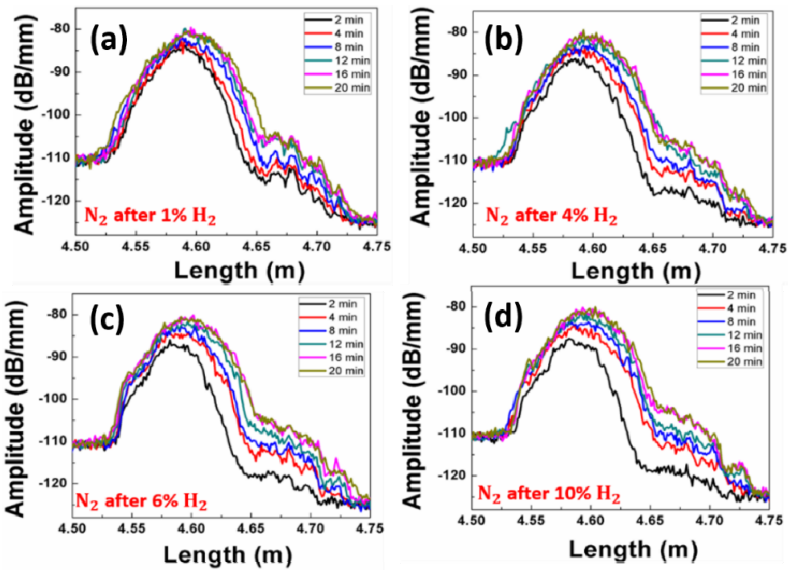

Fig. 8-4. Time-dependent response of the sensor to nitrogen after hydrogen exposure with various concentration a) 1%, (b) 4%, (c) 6%, (d) 10%.

The transmitted power change upon hydrogen exposure was also recorded upon heating with the temperature ranging from 500 ℃ to 750 ℃. The results are shown in the Fig. 8-5. A more well-defined sensory response was achieved at higher temperature compared with lower one, which might be due to the more active Pd element in the sensing film as proved by many other researchers. Meanwhile, we notice that the power change when exposing to 6% hydrogen (750 ℃)is about 34%, which is quite significant compared with the previous results. The enhanced signal change is the result of the introduction of the textured surface which significant increase the surface-to-volume ratio that providing more active Pd site for the gas absorption.

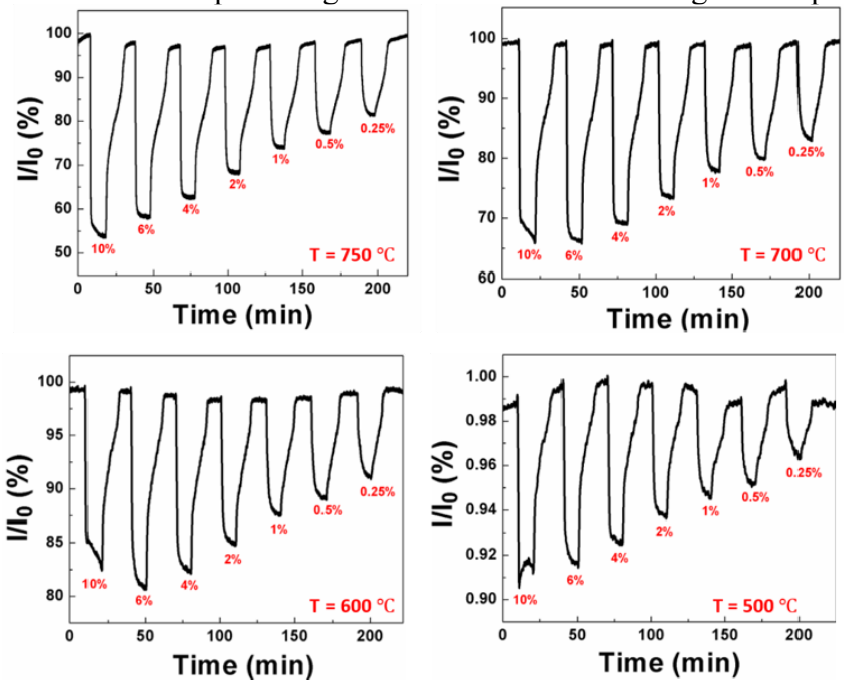

Fig. 8-5. The time-dependent transmitted power change upon hydrogen exposure at (a) 750 ℃, (b) 700 ℃, (c) 600 ℃, (d) 500 ℃.

The transmitted power change at different temperatures upon various hydrogen concentration is shown in the Fig. 8-6(a). The output power change is in proportional with the elevated temperature, which corresponds to the case in Fig. 8-4. Moreover, the slope of the profile tends to gradually increase with elevated temperature.

Sensory speed is another crucial factor in evaluating the sensing performance. Herein, the response time of sensor at 750 ℃ was calculated as the time required for the transmitted output power reaches 90% of its maximum level, and the response time at various hydrogen level is shown in the Fig. 8-6(b). In the figure, as the hydrogen concentration increase, the sensor becomes more responsive. For example, when the sensory is exposed to 6-10% hydrogen, the response time reduced from more than 120 s (0.25% hydrogen) to less than 20 s (10% hydrogen), which is more significant compared with previous result. The improved sensitivity is resulted from the nanostructure which makes the gas molecule more accessible.

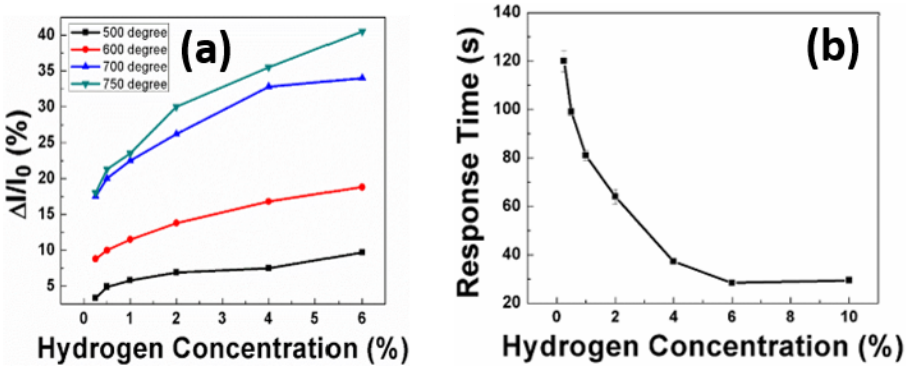

Fig. 8-5. (a) The time-dependent transmitted power change upon hydrogen exposure at various temperature, (b) sensor response time at different hydrogen level.

Summary: In this perform period, we made efforts to characterize Pd-TiO_2 infiltrated nanograss structure on D-shaped optical fibers. Using the Rayleigh backscattering reflectometer as a mean to perform distributed absorption measurements, we characterized hydrogen gas response using the optimized nanograss structures (500-nm height, 15-minute RIE etching) infiltrated with Pd-TiO_2 sensory film. In this quarter, we show that Pd concentration will have significant impact on distributed absorption measurement for hydrogen concentration between 0.5% and 10% from temperature between 500C and 750C. The optical transmission measurements show a reproducible hydrogen measurements from 0.25% and 10% with hydrogen response time up to 20 seconds. Based on this success, we will further optimize our nanograss structures to improve the operational temperature of distributed hydrogen sensors to reach 800C.

Efforts on Continuous Improvement of Nanograss-based Fiber Sensors for Distributed Hydrogen Sensing

In the previous research period, we made efforts to characterize Pd-TiO_2 infiltrated nanograss structure on D-shaped optical fibers. Using the Rayleigh backscattering reflectometer as a mean to perform distributed absorption measurements, we characterized hydrogen gas response using the optimized nanograss structures (500-nm height, 15-minute RIE etching) infiltrated with Pd-TiO_2 sensory film. In this quarter, we show that Pd concentration will have significant impact on distributed absorption measurement for hydrogen concentration between 0.5% and 10% from temperature between 500C and 750C.

In this period, we have achieved a significant success toward the development of nanostructures for high-temperature applications. It is well-known that nanostructures are far more vulnerable to high-temperature degradation than their bulk counterpart. This is probably due to large surface defects associated with large surface area. Therefore, nanostructures, though could be useful for short-term applications, are prone to high-temperature melting and degradation.

9.1: Solving Nanograss Melt Issue at High Temperature

To better understand the sensing performance of metal-oxide on top of the textured fiber surface, a thoroughly study of the nanograss at high temperature was carried out. In the following experiment, nanograss was characterized from both topography and chemical aspects when gradually increased the operational temperature.

To begin with, D-fiber was first etched by the RIE for 15 min (the optimal sensing structure), and the etching recipe was mentioned in previous report. The resulted nanostructures were shown in Fig. 7-4 and also shown here as Fig. 9-1. This serves as a reference for the following experiment. In the figure, a densely packed nanograss array was formed on top of the fiber surface with the average height around 411 nm and widths of 50 nm.

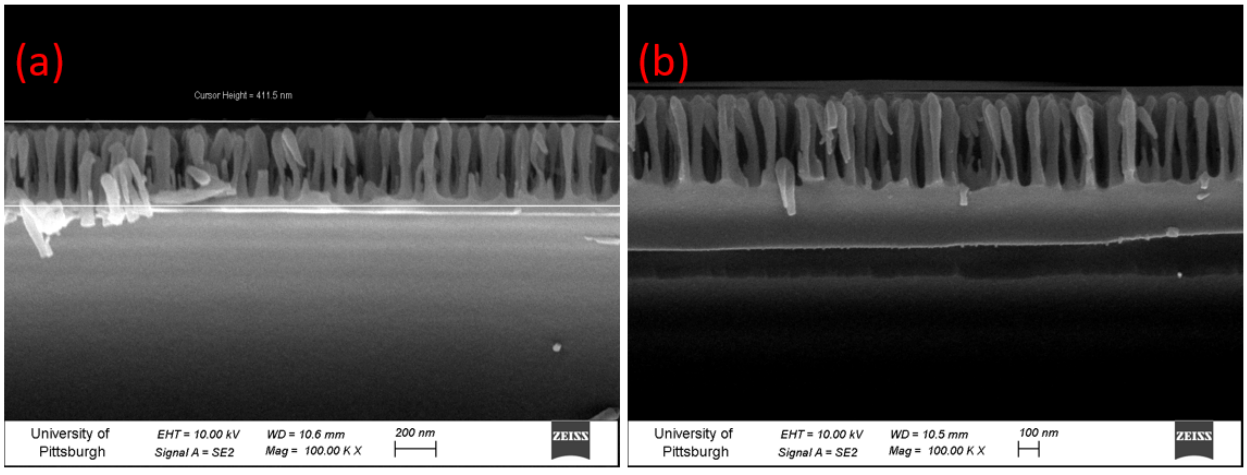

Fig. 9-1: The cross-sectional view of the D-fiber surface after 15 min etch by RIE system

The etched fiber sample was then transferred into an oven with various setting temperature. After annealing in 400 ℃, no apparent topography change of nanograss was observed, while nanograss morphology stay identical as shown in Fig. 9-1(a). The operating temperature of the furnace was further increased to 600 ℃, and the resulted nano-grass is shown in Fig. 9-2. In Fig. 9-2(a), the height of the nanograss was found to reduce to 352 nm across the whole fiber, 60 nm less than the sample at room temperature. In addition, the gaps around nano-grass structures on top of the core area from the plane view (Fig. 9-2(b)) appears to increase with the cladding area. The core area was confirmed by the presence of Ge in the EDX (fig 30(c)).

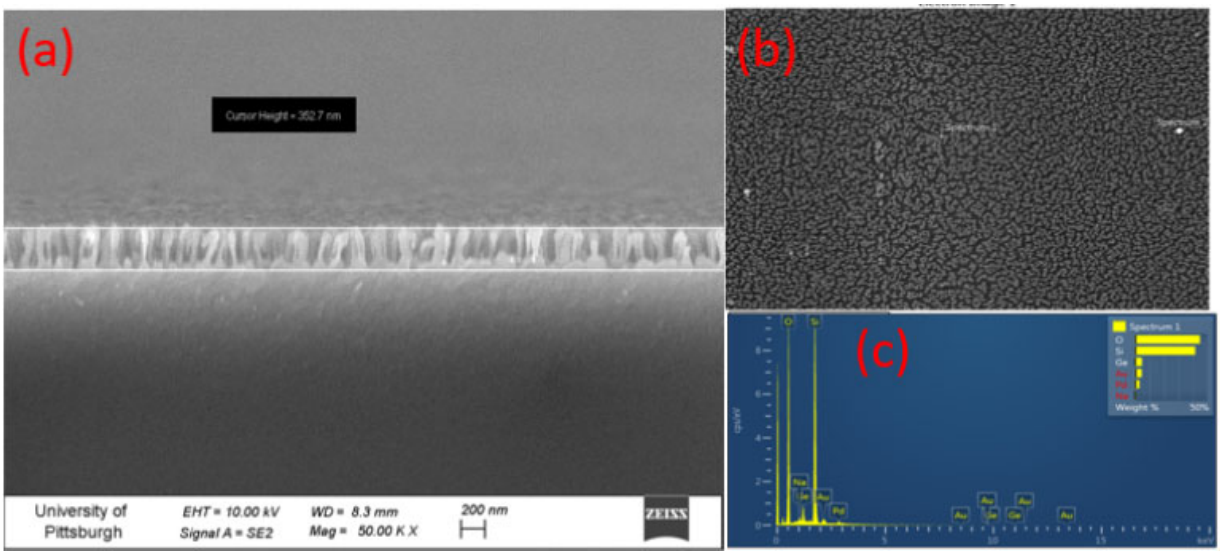

Fig. 9-2: (a)The cross-sectional view, (b) plane view, (c) energy dispersive spectrum (EDX) of the D-fiber surface after 15 min etch by RIE system at 600 ℃

At 750℃, a significant reduction of nanograss height was confirmed as shown in Fig. 9-3(a). The densely packed nanograss disappears due to partial melting and turned into sparsely separated shadow wavy pattern with average height around 70 nm (Fig. 9-3(b)). This is in sharp contrast to bulk Ge-doped silica (composition of fiber core) melting temperature at ~1250°C.

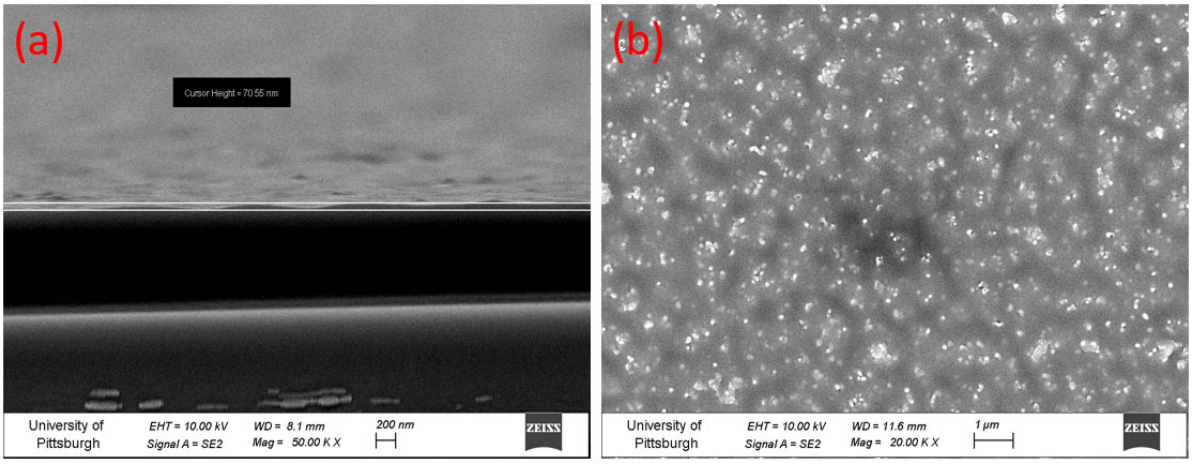

Fig. 9-3: (a)The cross-sectional view, (b) plane view of the D-fiber surface after 15 min etch by RIE system at 750 ℃

Once annealed in 800 ℃ for 1 hour, the nanograss, as shown in Fig. 9-4, was totally melted out in the core region while it still preserved in the cladding area. This is probably due to higher melting temperature of pure silica than Ge-doped silica. This underlying mechanism is unclear right now. It might be related to the Ge doping and further investigation is needed to explain this "melting" phenomena.

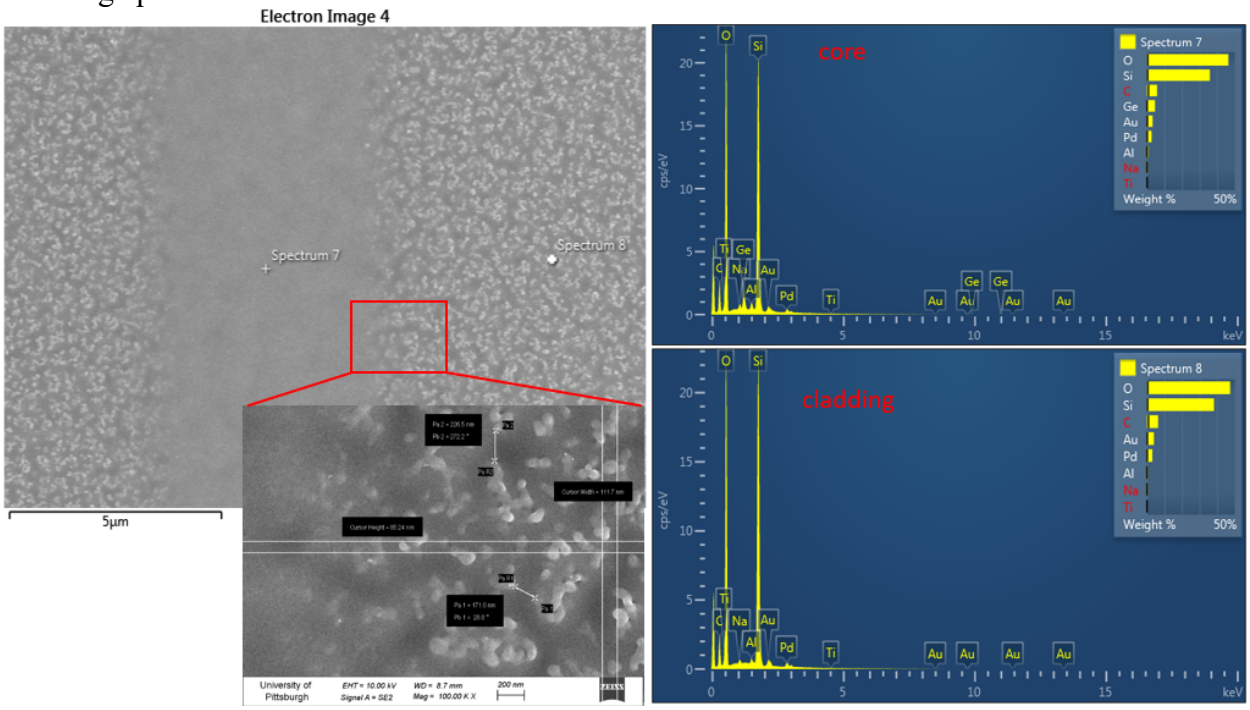

Fig. 9-3: The plane view of the D-fiber surface after 15 min etch by RIE system at 800 ℃

The melted nanograss could be a significant issue for sensor performance since the tuning effect of the refractive index of metal-oxide would be eliminated. In fact, this has been a common issue for all nano-materials based sensors developed for high-temperature applications. For example, in our previous works detailed in this report, direct deposition Pd-TiO_2 nanostructures also start to collapse at 850ºC. This is despite that the melting temperature of bulk TiO_2 is around 1500ºC.

To solve this issue, we deposit HfO_2 thin film on top of the nanograss as a protecting layer using an atomic layer deposition (ALD) system. HfO_2 is well known for its high-Temperature stability. Melting at 2758ºC, the degradation of HfO_2 nanostructure could occur well above 1500ºC. After 100 cycles of ALD deposition, nanograss was covered by HfO_2 film with the coating thickness around 15 nm. The sample was then annealed in the furnace with the setting temperature of 750 ℃ for 1 h, and the result is shown in the Fig. 9-4. From Fig. 9-4(a-b), we found that the height nanograss reminds unchanged as well as the gaps between nanograss stay the same, indicating that the nanograss "melting" was prevented by the HfO_2 protect layer. The 15-nm HfO_2 film is smaller than the pore space but will add considerable thickness to nanograss with average size of 70 nm. To further address this problem, the coating thickness is optimized to 5 nm with 35 cycles of ALD coating. The coated sample was transferred into the furnace for the annealing treatment as mentioned above. The result is shown in Fig. 9-5. The nanograss remained intact from both views, confirming the same protecting functionality of the thinner film.

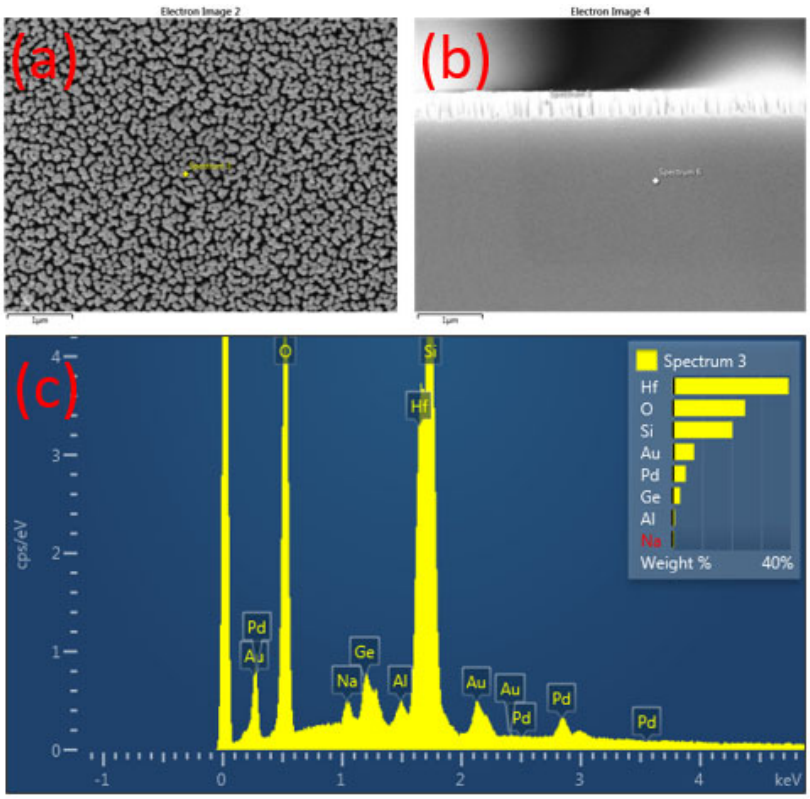

Fig. 9-4: (a) The plane view, (b) cross-sectional view, (c) EDX of the sample with 15 nm HfO2 protection layer at 800 ℃

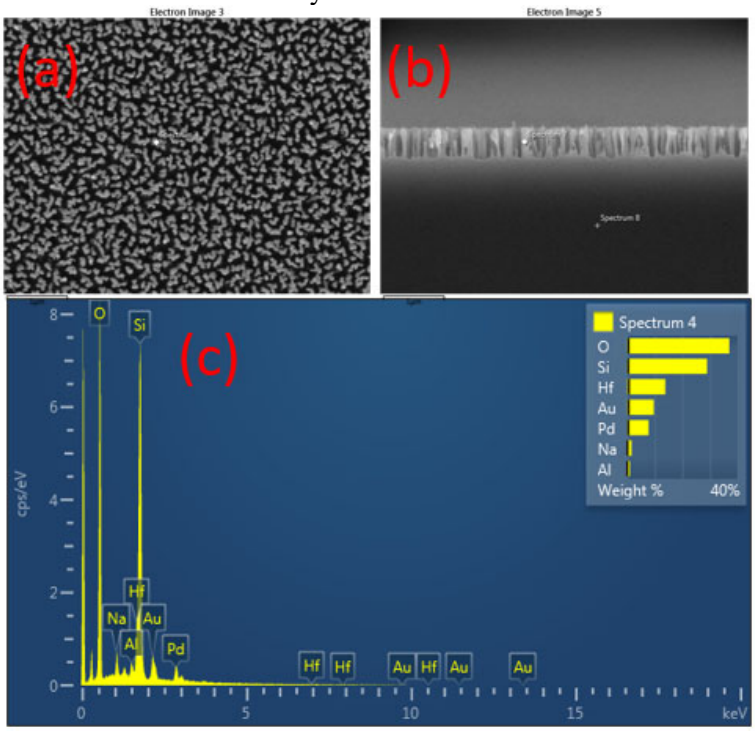

Fig. 9-5: (a) The plane view, (b) cross-sectional view, (c) EDX of the sample with 5 nm HfO2 protection layer at 800 ℃

Once this “melt” issue is resolved, the next step is to optimize the sensory film distribution on top of the nanograss. In this experiment, the sol-gel solution was first diluted to 1/4 of its original concentration with ethanol to prevent the large crack of metal-oxide as confirmed in the previous report. Four samples with various nanograss sizes were prepared in the experiment with RIE etching time of 4, 6, 7, and 10 min respectively. Dip coating method is introduced in the experiment to get uniform distribution. The topography of the coated nanograss was characterized by SEM and shown in the Fig. 9-6. In the plane view, the cracks appear in the sensory film surface and grows larger with longer the RIE time, which matches very well with the previous observation. The sensory film, as shown in the cross-sectional view, tends to penetrate and fill the gap between nanograss. Compared with small nanograss, the large gaps in sample with longer etching allows deeper penetration of sensory film, forming a more metal-oxide coated nanograss layer.

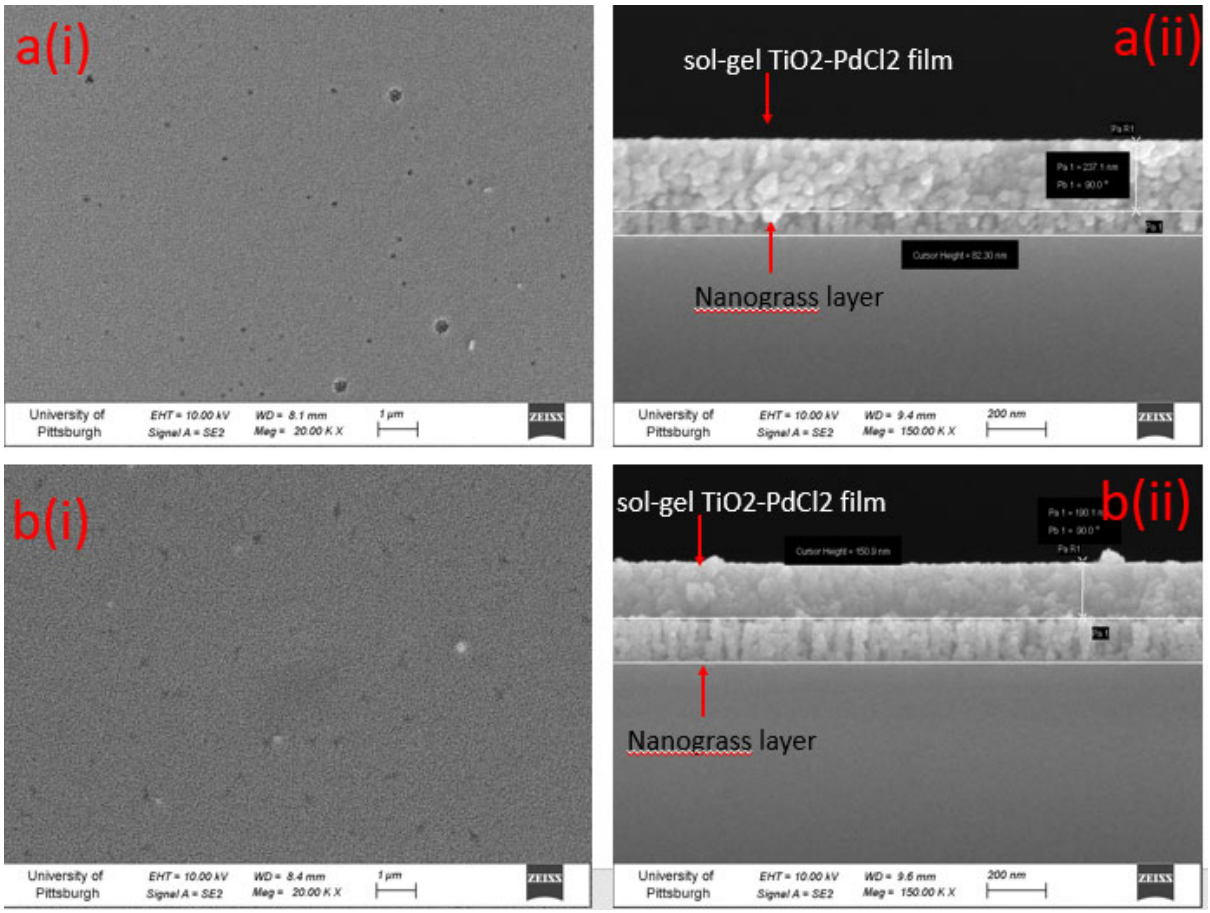

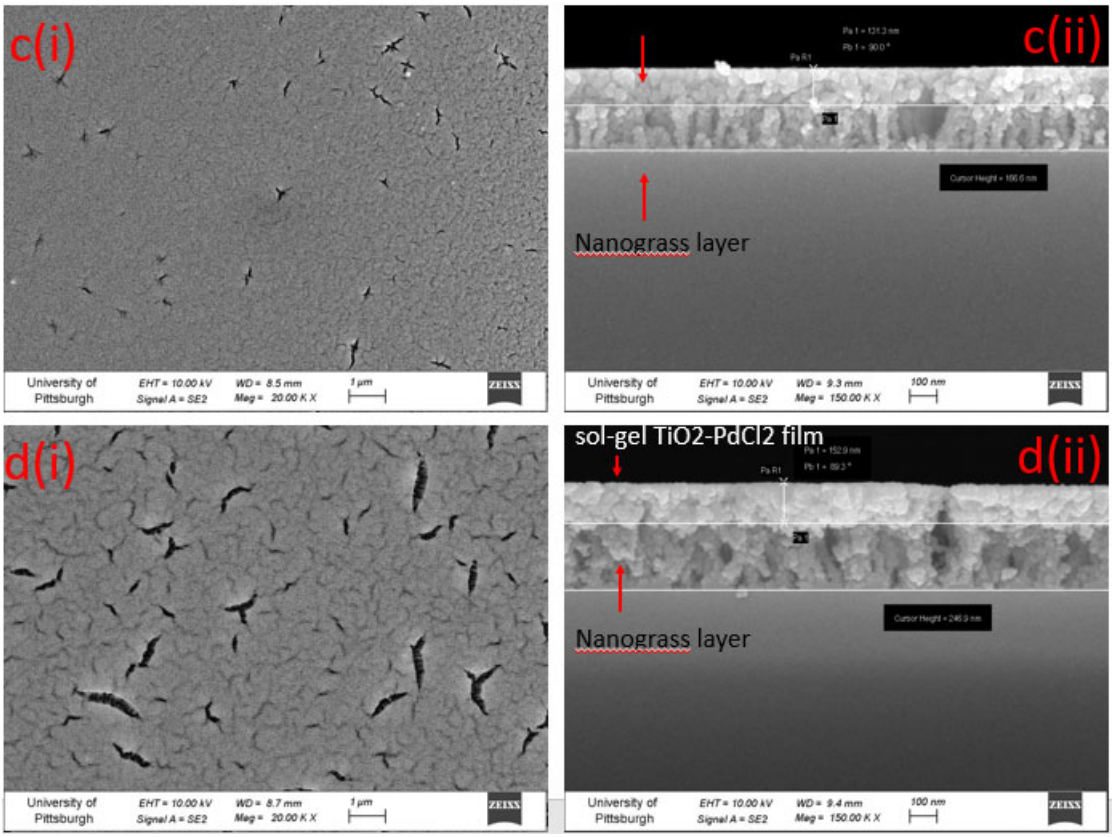

Fig. 9-6: The plane and cross-sectional view of sensing film on 5-nm HfO_2 protected nanograss after (a) 4 min, (b) 6 min, (c) 7 min, (d) 10 min

The effects of the HfO_2 protecting layer on sensory performance is then studied. In the experiment, metal-oxide sol-gel was drop-coated on top of 5-nm HfO_2 protected nanograss-textured D-fiber. Nanograss after 5-min RIE etching was chosen as the textured surface to avoid the crack of the sensory film at high temperature. The distributed sensing behavior was record by OFDR system at 750 ℃. The experimental setup is the same as previous report, and experimental result is shown in the Fig. 9-7. In the figure, a slightly enhanced detection limit was observed as the distinguishable sensory profile in response to 0.25% and nitrogen. However, the sensory performance degrades at higher gas concentration as the overlap of sensing profiles for 6% and 10% hydrogen, which might be due to the diluted sensory film that accommodate less Pd sites for PdH formation. To further improves the sensor performance, an optimization process of RIE time and metal oxide concentration is needed for our following experiments.

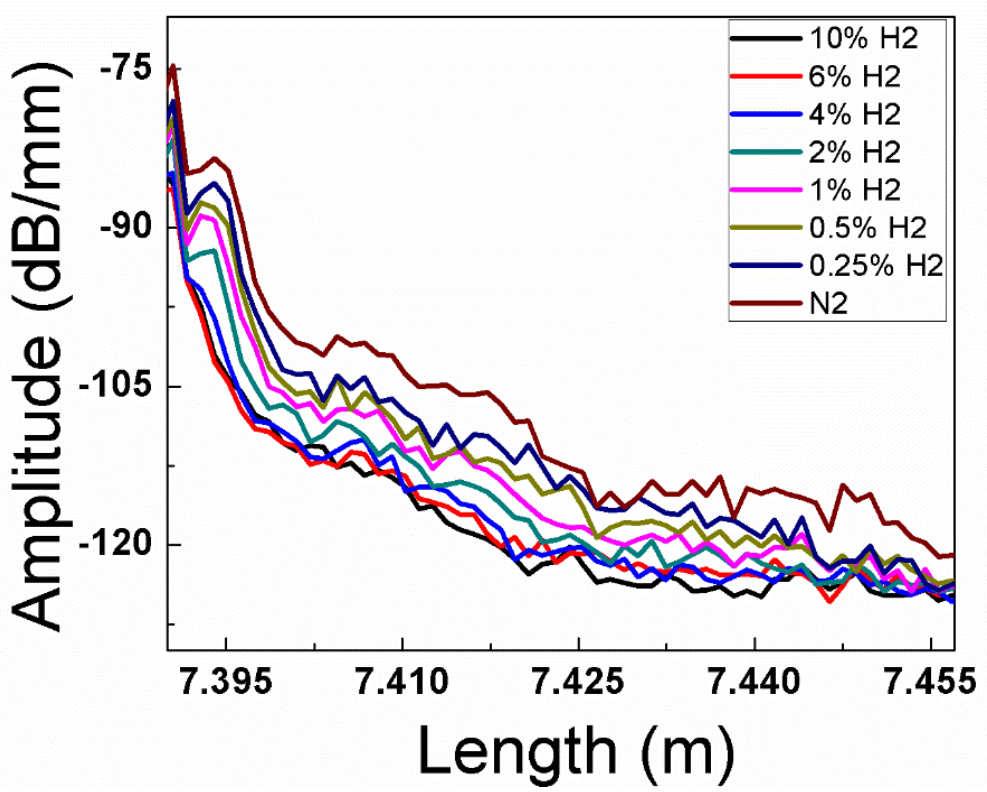

Fig. 9-7: Distributed sensory behavior of HfO_2 protected hydrogen sensor with various gas concentrations

Summary: In this period, we have achieved a significant success toward the development of nanostructures for high-temperature applications. It is well-known that nanostructures are far more vulnerable to high-temperature degradation than their bulk counterpart. This is probably due to large surface defects associated with large surface area. Therefore, nanostructures, though could be useful for short-term applications, are prone to high-temperature melting and degradation. In this quarter, we have developed a method to solve this problem and potentially push applicable temperature of nanostructure higher by at least 200ºC. This work will have significant impact for nanostructure applications for high-temperature environments.

Efforts on Developing Low-Cost Multiplexable Hydrogen Point Sensor Arrays.

In this report, we will present our initial result of hydrogen sensor based on Intrinsic Fabry-Perot interferometric (IFPI) for hydrogen monitoring at 750 °C. Comparing with distributed sensor, IFPI sensor array can be interrogated using instrument that is much cheaper. The IFPI array also have potentials to achieve much higher sensitivity.

Part 1. Principle of FPI sensor

Fiber-optics sensor based FPI has been widely deployed in structure health monitoring applications through the measurement of the strain, temperature, and pressure [36-40]. The distinguished characteristics of fast response, resilient to the electromagnetic interference, and high sensitivity make it a promising candidate for the chemical measurement too. Depending the cavity configurations, there are generally two types of FPI sensor: EFPI and IFPI which is short for extrinsic and intrinsic FPI interferometer, respectively. An EFPI was formed when the cavity of the optical sensor was constructed by two fiber ends with air gap while generally an IFPI was usually fabricated through a fiber Bragg grating inscribed into the fiber core with the cleaved fiber end as a mirror or two mirrors were both fabricated by the laser processing inside the optical fiber core. In this work, the IFPI cavity was formed by the two enhanced Rayleigh scattering point fabricated by femtosecond laser writing.

Optical interference servers as the underlying principle of FPI sensor, in which the optical beam was usually split into two separated optical signals with different optical path as the cavity length. The recombined light property such as the intensity is a function of the cavity length which could be tuned when exposed to the environmental change. By analysis and demodulate the combined interference pattern, the cavity length change will be extracted as an indicator of the targeted chemical or environmental variation. Mathematical calculation can be deduced in referring to the configuration of Figure 10-1.

In the figure, two point in optical fiber with certain separating distance (from 200 nm to 1 mm) were inscribed by femtosecond laser to form the nanograting structure for the enhancement of the Rayleigh backscattering, serving as the two mirrors inside the optical fiber. The Rayleigh enhancement of the background signal is around 45 dB. To eliminate the Fresnel reflection from the fiber end that disturb the Rayleigh backscattered signal from the cavity, the optical fiber was physically bend to form multiple small cycles with a diameter less than 0.5 cm to maximus the loss at the fiber end, and the total reflected light is the sum of the light reflected from R1 and R2 interface, when neglecting the relative small signal of the Rayleigh scattering from unenhanced parts.

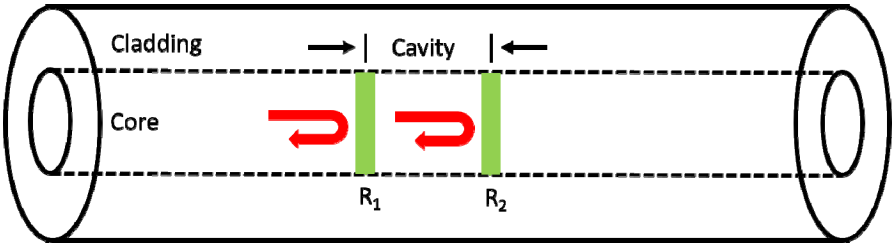

Figure 10-1. Schematic of the intrinsic FP structure.

The intensity of the Rayleigh backscattered light can be calculated as:

$$I_{rtotal}(\lambda) = I_{1ref}(\lambda) + I_{2ref}(\lambda) + \sqrt{I_{1ref}(\lambda) I_{2ref}(\lambda)} \cos(\phi)$$

where λ is the input light wavelength, I_{1ref} and I_{2ref} stands for the reflected light intensity from Rayleigh enhanced point 1 and 2, respectively. ϕ is the phase difference between the two reflected light introduced by the optical path difference (cavity length) when the phase shift caused by the material is neglected. The phase difference can be described as:

$$\varphi = 2k\, n_{eff}\, L\cos(\theta)$$

where k denotes the wave vector, n_{eff} stands for the effective refractive index, θ is light incident angle, L is cavity length. Cos(θ) approaches to 1 for optical fiber due to the small incident angle and will be neglected for following discussions.

Assuming that the laser enhanced points has the the same reflectivity, and the total reflected light intensity can be rewrite as:

$$I_{rtotal} = I_{input} \frac{2R(1-\cos\phi)}{1+R^2-2R\cos(\phi)}$$

where R is the reflectance of the Rayleigh enhanced surface. By introducing the term of finesse F, the transmitted output power ratio can be calculated as:

$$\frac{I_{trans}}{I_{input}} = \frac{1}{1+F\sin^2(\phi/2)}$$

where the finesse is:

$$F = \frac{4R}{(1-R)^2}$$

It can be noted from the equation that the output power change is a function of the cavity length. By demodulating the output light power spectrum, the cavity length variation can be calculated. This equation is defined as the Airy function. MATLAB was utilized to quantify the relationship between the phase shift and the transmitted or reflected light power, and the results are plotted in the Fig. 10-2. The phase shift ranges from -6π to 6π, and the fitness was adjusted from 0.5 to 5. As can be seen from the simulation, large fitness results enhanced reflected light, which is in consistent with the increased reflectance in the above equation. In our case, the enhancement of the back scatted light introduced by the laser irradiation is more than 40 dB compared with random Rayleigh scattering by the fiber density fluctuation, which could significantly improve the signal to noise ratio and results better resolution in chemical sensing applications.

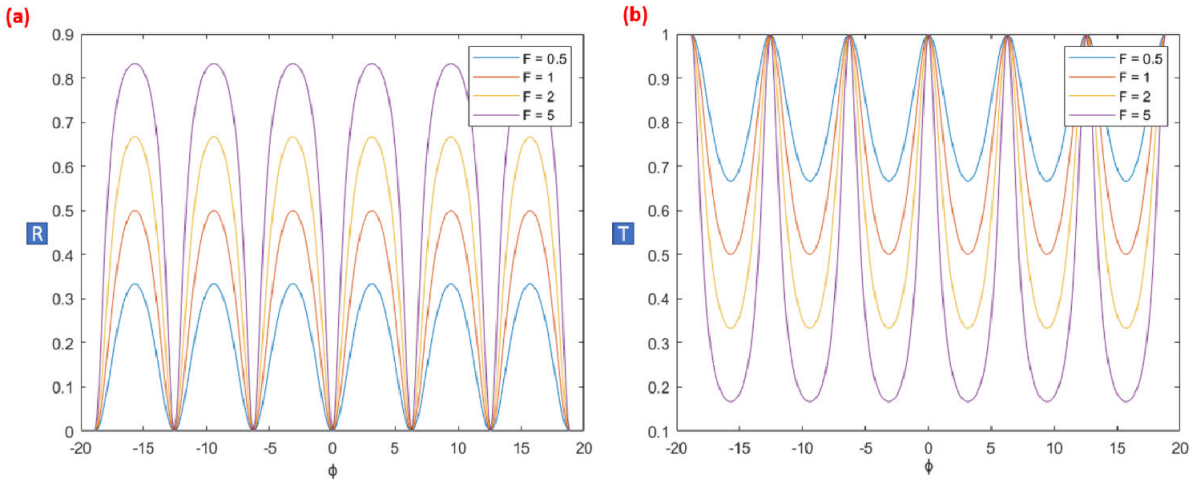

Figure 10-2. Reflected (a) and transmitted spectrum (b) of Airy function.

The resulted interference spectrum of the intrinsic FPI sensor with 1 sensing cavity fabricated by femtosecond laser writing is shown in the Figure 10-3, and a well-defined fringe with good contrast was observed in the figure.

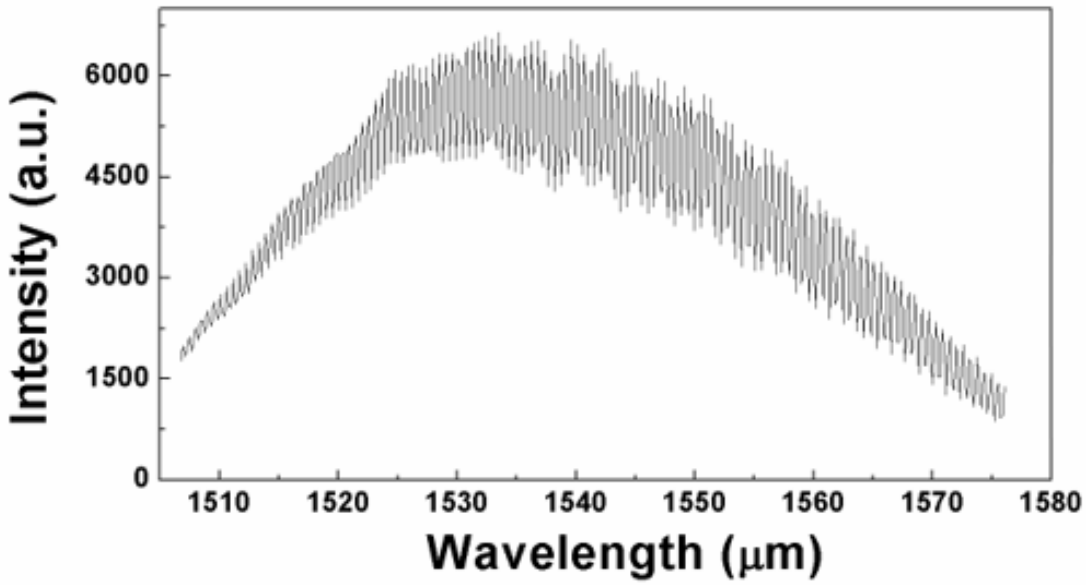

Figure 10-3. an actual FP sensor interference spectrum.

Part 10-2. Fabrication of Fabry-Perot Cavity in Optical Fiber

The sensing cavity of the fiber FPI sensor was fabricated through ultrafast laser writing. The experimental setup is shown in Figure 10-4(a). The laser source utilized in the experiment is a femtosecond laser with the pulse width of 300-fs and operating wavelength of 800 nm. The Coherent RegA laser system operates at 250 kHz, and the laser beam with 80 nJ energy was reshaped to form a symmetrical beam with the dimension between 2 μm to 7 μm, and further focus to the fiber core through an oil emersion objective with the NA of 1.25 to eliminate the spherical aberration. Once finishing the laser irritation on the first point of the optical fiber, the

moving stage would roll the fiber another position with specific distance for the second point writing. Those two enhanced points forms a cavity that reflected the optical light inside the optical fiber, and the separating distance between those two points are defined as the cavity length.

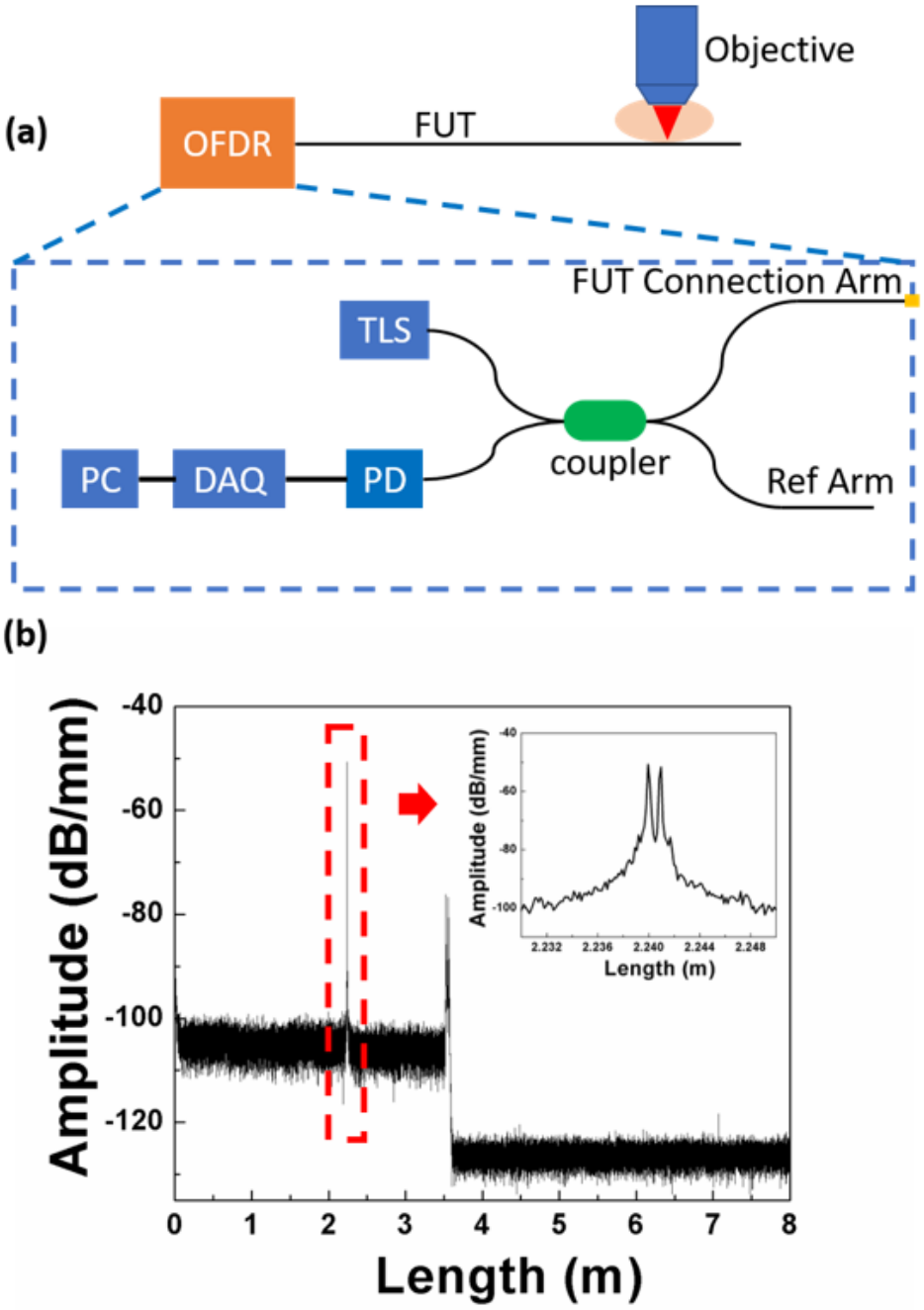

Figure 10-4. (a) Schematic of the cavity fabrication by femtosecond laser writing, (b) OFDR spectrum of the fiber with 1 cavity, inset is the enlarged figure of the measured cavity.

Part 10-4. Demodulation algorithm for Fabry-Perot Sensors

Apart sensing cavity manufacturing, a reliable signal demodulation algorithm with high precision and low computational cost is also crucial in determining the sensing system performance. The demodulation process is carried out by analyzing the spectrum pattern formed through beam interference. The white light interferometry (WLI) is considered as the most sophisticated approached with the advantages of the high accuracy and resilience to the environmental fluctuation. Broadband source or frequency swept light source is utilized in the setup.

The whole demodulation process can be described as the flow chart [48] as shown in the **Figure 10-5**. The initial spectrum data was first reshaped to eliminate the envelope influence of the laser power spectrum. The pre-processed was then being interpolated to form a uniform wavenumber distribution instead of the wavelength. The reshaped spectrum was transferred into frequency domain though FFT. The peak position of the FFT spectrum relates to the position of the cavity length. The estimation of the peaks in FFT consists two steps: the initial rough estimation of the peak through the Buneman frequency estimation followed by the further verification and adjustment by the total phase analysis to minimize the error of the phase shift number. This whole demodulation process is defined as type II approach due to its direction calculation of the total phase. Another commonly used method is to calculate the OPD density from the density of the fringes while ignoring the initial phase, which in this case, is less efficiency with limited resolution.

The interference spectrum equation of an IFPI can be modeled as:

$$I_s\left(k\right) = 2I_0\left(k+k_0\right)\left[1+\gamma\cos\left(l\left(k+k_0\right)+\varphi_0\right)\right] \quad \textbf{(1)}$$

where $I_0(k)$ is the light source intensity spectrum envelop, k is the wavenumber, k_0 is the wavenumber of the spectrum's first wavenumber point, γ is the fringe visibility, l is the optical path difference (OPD) of the FPI cavity which is $l = 2nd$ where n is the refractive index of the optical fiber core and d is the cavity length, and φ_0 is the initial phase which is zero for the IFPI. In order to perform the demodulation algorithm, the light source power spectrum envelop function $I_0(k)$ are eliminated using a standard normalization method. Thus, an interpolation process can be performed to the AC component of Eq. (1) to obtain equidistant points of wavenumber k.

In this work, the discrete Fourier transform (DFT) is used to demodulate sensor data. The discretization of Eq. (1) after the interpolation process can be expressed as:

$$I'\left(n\right) = 2\gamma\cos\left(\frac{l\Delta kn}{N} + lk_0 + \varphi_0\right) \quad \textbf{(2)}$$

where $k = \Delta kn/N$, $n = 0,1, 2, \ldots N\text{-}1$ is discrete series, N is the number of the data set and $\Delta k = k_1 - k_0$, where k_0 and k_1 are wavenumbers corresponding to the beginning and the end of wavelengths of the acquired spectra, respectively.

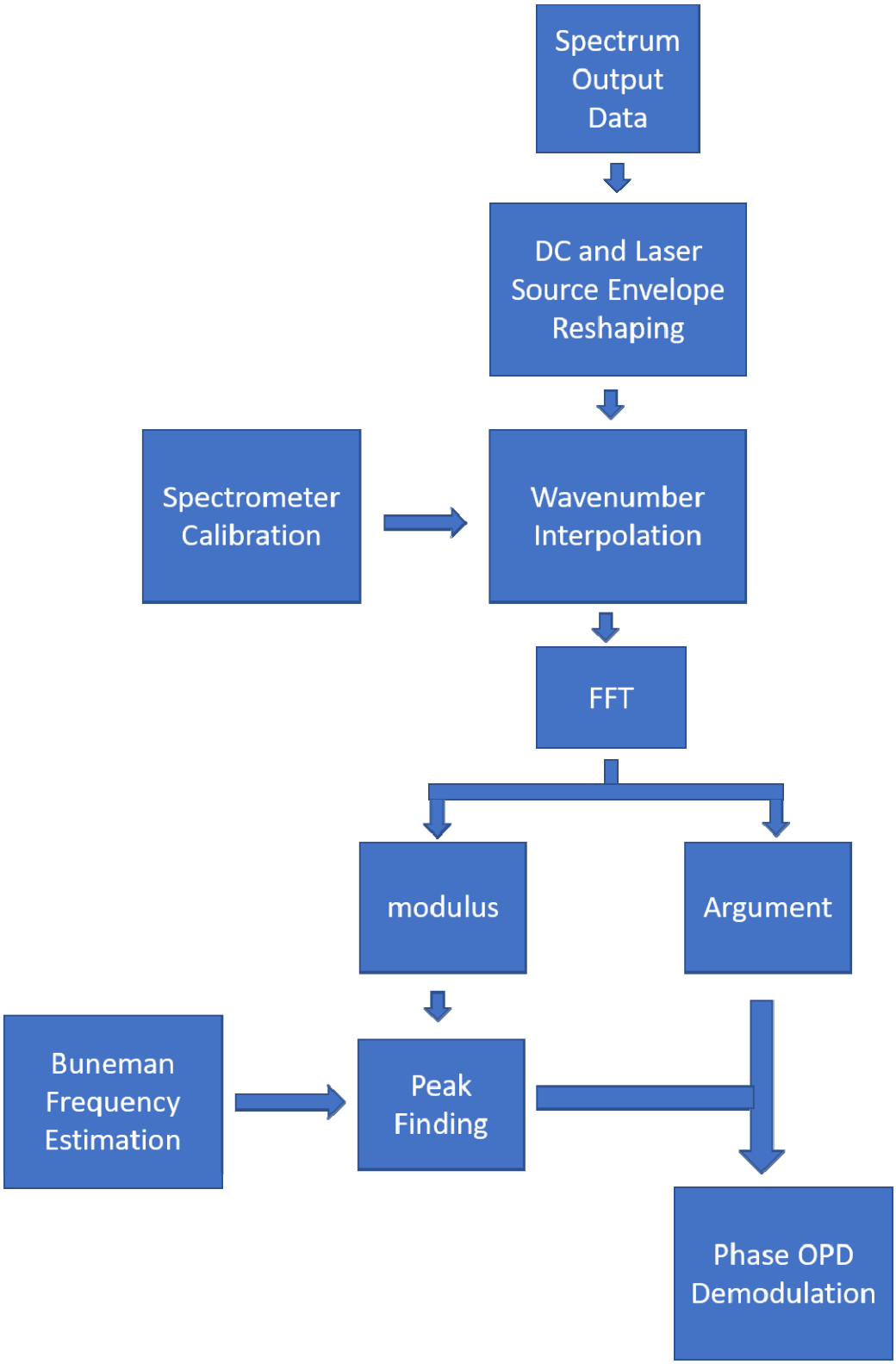

Figure 10-5. Demodulation algorithm flow chart.

By applying DFT to the spectral set of Eq. (2), we have Eq. (3) based on Euler formula.

$$F(\xi) = \sum_{n=0}^{N-1} \gamma e^{i(\frac{l\Delta kn}{N} + lk_0 + \varphi_0)} e^{-2\pi in\xi/N} = \gamma e^{i[lk_0 + \varphi_0 + \pi(\frac{l\Delta k}{2\pi} - \xi)(\frac{N-1}{N})]} \frac{\sin[\pi(\frac{l\Delta k}{2\pi} - \xi)]}{\sin[\pi(\frac{l\Delta k}{2\pi} - \xi)/N]} \quad \textbf{(3)}$$

where $F(\xi)$ is the positive half of the DFT spectrum and ξ is directly related to the OPD. In this work, Eq. (3) and Buneman frequency estimation is used to determine both the peak location ξ_P and its phase from experimental data in order to determine the cavity length of IFPI sensors. Unlike demodulation algorithm presented in [17, 18], two distinct cases were considered to avoid phase jump problems. At the peak location where $\xi \equiv \xi_P = l\Delta k/2\pi$, as shown in Eq. (3), the total phase is $\varphi(l\Delta k/2\pi) = lk_0 + \varphi_0$, where $\varphi(\xi)$ is the phase term in Eq. (3). The relationship between the OPD l and the peak index ξ_P derives from the above equation as

$$l = \frac{2\pi\xi_P}{k_1 - k_0} \quad \textbf{(4)}$$

The total phase at the peak can also be expressed as

$$\varphi\left(\frac{l\Delta k}{2\pi}\right) = \frac{2\pi\xi_P k_0}{k_1 - k_0} + \varphi_0 \quad \textbf{(5)}$$

Thus, accurate estimation of the peak index ξ_P from the DFT spectra of experimental data is key to determine the OPD l and dynamic strain exerted to the IFPI sensor. For the DFT data, there are two scenarios depicted in Fig. 2 to estimate ξ_P. First, the peak index ξ_P falls between two adjacent points (spectral components) of the DFT spectrum depicted in Fig. 10-6a. In this case, phase difference φ_{m+1}-φ_m of these two points are close to -π (φ_{m+1}-φ_m=-π±1/5|π|). The demodulation scheme for this case has been reported before.

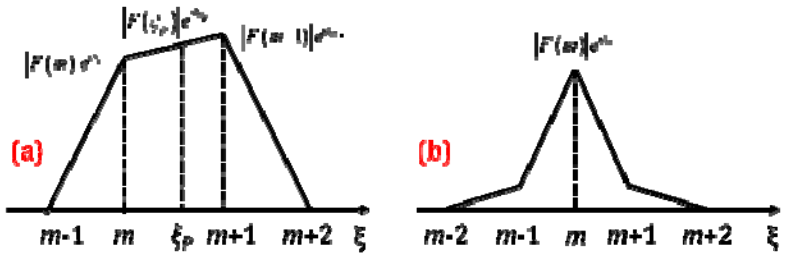

Figure 10-6. Schematic of the positive DFT peak of the processed interference spectrum. (a) First case that the peak index falls between two adjacent points. (b) Second case that the peak index is close to an integer *m*.

To avoid phase jump problem, we also consider the second case where the peak of the DFT spectrum approaches to one of the frequency components of the DFT spectrum, $\xi = l\Delta k/2\pi = m$, where m is an integer as depicted in Figure 10-6(b). In this case, phase difference φ_{m+1}-φ_m and φ_m-φ_{m-1} are not -π and beyond phase arranges incurred in Fig. 2a. For the second condition, the phase of the peak is

$$\varphi_{\xi p} \approx \varphi_m \tag{6}$$

where φ_m is the total phase of at the peak of the DFT spectrum $F(\xi)$, which was obtained from the measured data. Due to the wrapping nature of phase, we have

$$\varphi\left(\frac{l\Delta k}{2\pi}\right) = \varphi_{\xi p} + 2\pi a = \varphi_m + 2\pi a \tag{7}$$

where a is an integer. Using Eq. (5) and (7), a can be expressed as

$$a = \frac{k_0 m}{k_1 - k_0} + \frac{\varphi_0}{2\pi} - \frac{\varphi_m}{2\pi} \tag{8}$$

where the peak location index ξ_p in Eq. (5) equals to m in this case. In Eq. (8), the calculated a is generally not an integer due to the error induced by the DFT phase φ_m, calculated from experimental data. Thus, the value of a is rounded to its nearly integer expressed as $[a]$. Therefore, the real peak index ξ_P, for the second condition, can be calculated from Eq. (8) by substituting $[a]$ for a as

$$\xi_p = \frac{k_1 - k_0}{k_0}\left(\varphi_m - \varphi_0 + 2\pi[a]\right) \tag{9}$$

Eventually, the OPD can be calculated from the relationship with ξ_P and Eq. (4). Using the demodulation scheme and approach described in this paper, phase jump can be suppressed for high speed demodulation.

Part 10-5: Experiment validation of measurement sensitivity

The experimental setup for vibration testing is shown in Fig. 10-7. A superluminescent light emitting diode (SLED) (EXS210059-01, Exalos) was used as a white light source with 60-nm bandwidth (1510 nm – 1570 nm). The broadband light emitted from the SLED passes through a circulator and is split into the REIFPI sensor and the free-space FP cavity by a 50:50 optical coupler, respectively. The free-space FP cavity is built to measure the displacement of the piezo stage in order to determine the absolute distance changes between two epoxy points [**Error! Reference source not found.**]. This serves as calibration to gauge the cavity length change measured by the IFPI sensor. The backscattered interference light was then captured by a high-speed spectrometer (FBGA, Bayspec) with 512 pixels and 5kHz maximum frame rate for demodulation. Two sides of the IFPI are glued between a stationary stage and a piezo-actuated stage using epoxy, respectively. The piezo actuator was driven a function generator at various frequency.

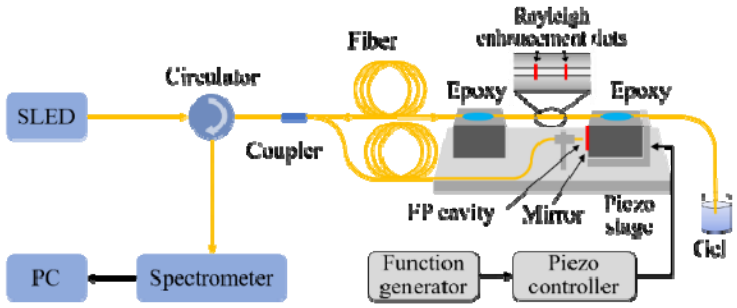

Figure 10-7: Experiment setup to validate IFPI sensor's sensitivity

In order to test the performance of the demodulation algorithm, two sensors with cavity length of ~530 µm and ~972 µm were tested when the frame acquisition rates of spectrometer were set at 500 Hz, 1 kHz, 2kHz and 4 kHz, respectively. Fig. 4(a) shows the static interference spectra of the IFPI with the cavity length of 972 µm. It is evident that shorter integration time of the spectrometer at higher sampling frequency yields poorer fringe visibility due to shorter detection integration time. Fig. 10-8 (b)-(e) shows the demodulated static cavity length when the frame rate of the spectrometer was set at 500Hz, 1kHz, 2kHz, and 4kHz, respectively. The standard deviations (SD) of the measurements were found to be 0.09 nm, 0.2 nm, 0.4 nm and 0.8 nm as shown in Fig. 4 (b)-(e). The optical cavity length also has impacts on SNR. Fig. 4 (f) show the demodulated results on static measurements for the IFPI with cavity length of ~530 □m. At 1 kHz acquisition rate, the SD is 0.034 nm (or 64 nε).

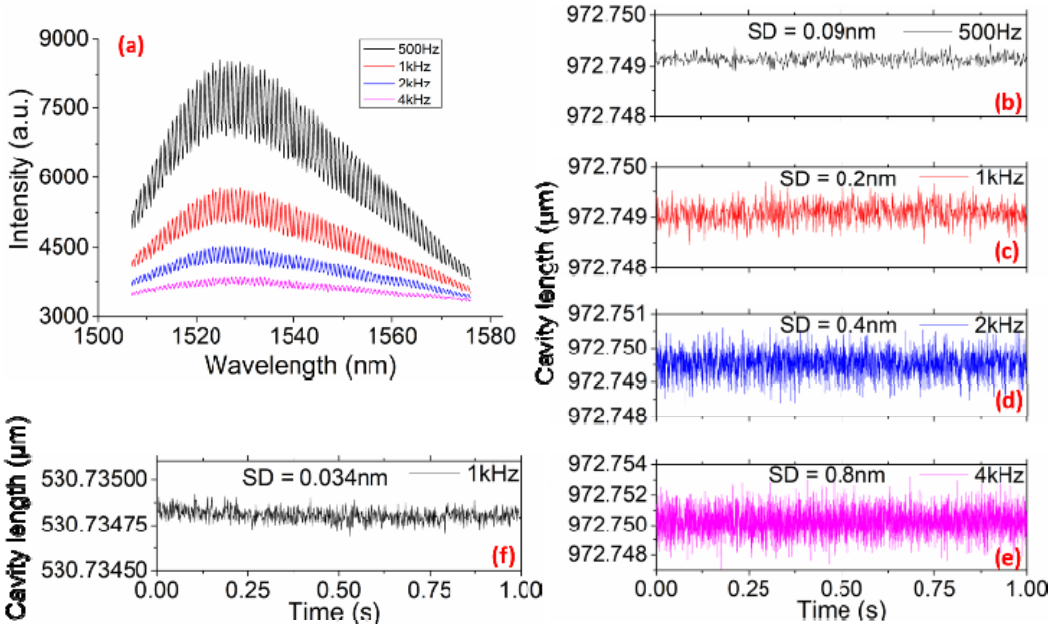

Fig. 10-8. (a) The interference spectrums for different frame rates of spectrometer. Static cavity length measurement results of a ~972 µm REIFPI for the spectrometer frame rates of (b) 500 Hz, (c) 1 kHz, (d) 2 kHz and (e) 4 kHz, respectively. (f) Static cavity length measurements of another ~530 µm REIFPI at a 1 kHz frame rate.

Summary of Efforts

In summary, this research period demonstrates that femtosecond laser direct writing can be a simple manufacturing tool to produce multiplexable IFPI sensors that can perform high-sensitivity strain measurement. Weak Rayleigh scattering points induced by the femtosecond laser can be sufficient to produce high-temperature stable IFPI sensor arrays for high-frequency vibration measurements. Using an improved fast white light demonstration scheme, absolute cavity length of IFPI sensors can be rapidly determined to achieve minimal strain measurement 64-nε. The minimum vibration strain measurement is 27 nε/√Hz for the vibration frequency of 100Hz and 2 kHz respectively. The vibration strain can also be detected in high temperature environment of 800 °C. These new IFPI sensors provide new and cost-efficient tools for harsh environment vibration measurements for energy and aerospace industry. Using this new fiber devices, we will perform hydrogen measurements for the next studies.

Efforts on Developing IFPI based Hydrogen Sensor Arrays

In this period, we present optical hydrogen sensor based on Fabry-Perot interferometer at room temperature. The intrinsic sensing cavity was fabricated through femtosecond laser manufacturing process. The sensor performs repetitive and reversible response with high detection limit of 0.25% and 1 % for point and distributed measurement, respectively.

Based on IFPI sensors fabricated in the last quarter, we demonstrate in Q3 of 2019, for the first time, to our best knowledge, multiplexable fiber IFPI devices for chemical sensing. Through coating of Palladium on fiber, functionized fiber IFPI devices can perform hydrogen measurements at six different location along a single fiber simultaneously. Through selection of length of optical cavities, hydrogen-induced swelling of Pd-coating and change of IFPI cavity length can be measured with 20-pm sensitivity. This results in highly sensitive measurement of hydrogen concentrations.

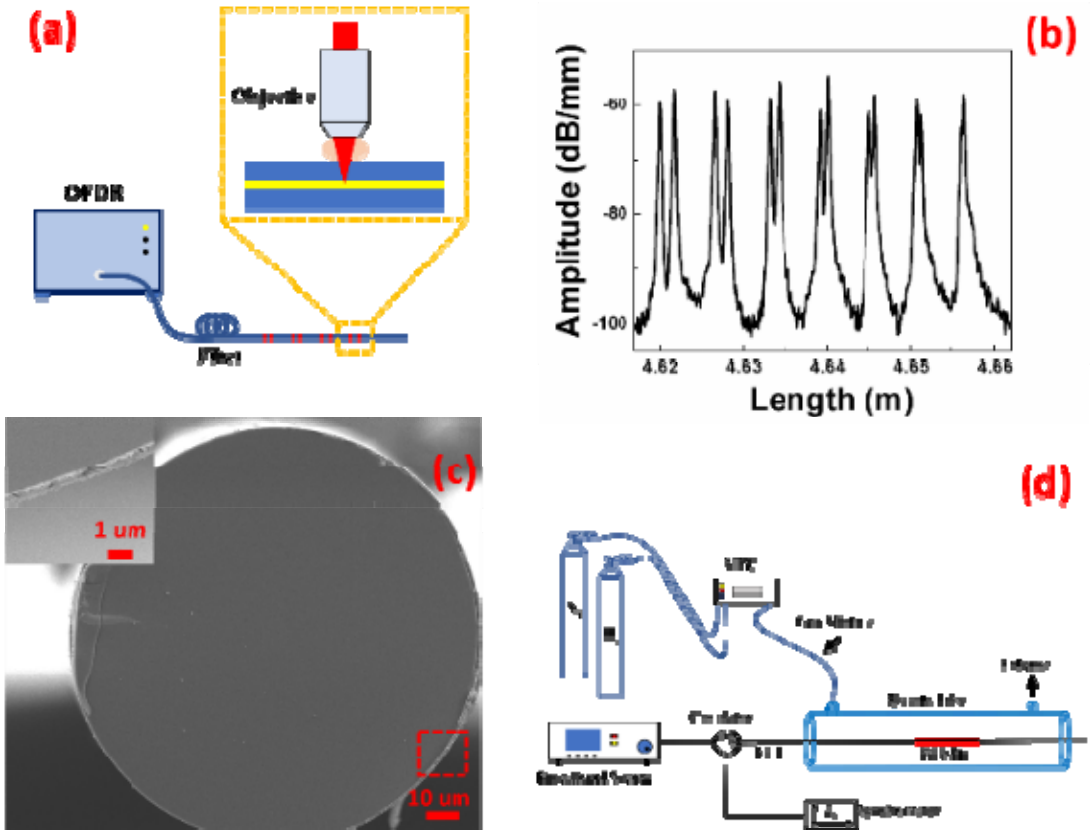

Fig. 11-1. (a) Schematic of laser fabrication process showing the cavity fabrication process by femtosecond laser irradiation, (b) OFDR spectrum of FPI formed by Rayleigh enhanced points in an optical fiber, (c) cross-sectional view of optical sensor, inset is magnified area of the Palladium-coated fiber, (d) schematic of experimental setup.

Standard single mode fibers (Corning SMF-28e+) was utilized in the experiment. The fiber was initially cleaned in the solvent (acetone, methane, and deionized water), and dried in nitrogen gas flow. The thoroughly cleaned optical fiber was then mounted on a motorized stage for IFPI device fabrications. The detailed fabrication process is depicted in Fig. 11-1 (a) and discussed in literature [20]. A Coherent RegA 9000 Ti:sapphire laser and amplifier system was used for device fabrication. It produces linearly

polarized laser beam of 800-nm, 270-fs at 250-kHz repetition rate. To generate the Rayleigh scattering defect centers, femtosecond laser pulses were tightly focused inside the core of a single-mode silica-core optical fiber using a 100× oil-immersion lens (N.A. 1.25). The laser focus was aligned in the middle of the fiber core to produce artificial scattering centers. Fourteen Rayleigh enhanced points were inscribed onto optical fiber to form 7 FPI cavities. The distance between each cavity is around 5-mm and the cavity length increase from 489 nm to around 1.7 mm with a step of 200 μm. The profiler of Rayleigh enhanced points in optical fiber was characterized by an optical frequency domain reflectometry OFDR system (LUNA OBR 4600), and the result Rayleigh backscattering profile is shown in the Fig. 11-1 (b).

In the figure, the Rayleigh enhancement appears to be uniform with a backscattered enhancement of 45 dB on average. The laser-processed optical fiber was then transferred into an e-beam evaporation chamber (Thermionics) for the Palladium functional film coating. A thin layer of Cr (10 nm) was first deposited on the fiber surface followed by the by 500-nm Pd deposition. After the initial deposition, the fiber was rotated by 180º and the same coating were deposited onto the other side of the optical fiber. In addition, to study hydrogen sensing performance, the FPI sensor was fabricated with cavity length 1186 μm. Once the hydrogen sensing calibration were completed on Pd-coated FPI sensors, a multiplexing sensor string consists of 5 Pd-coated FPI sensors for hydrogen measurements and 2 uncoated FPI sensors for temperature measurements. Using a scanning electron microscope (SEM), the cross-section view of the Pd-coated fiber is shown in Fig. 11-1(c). Although the coating thickness is not uniform across the fiber, most of the area has been covered by the Pd thin film with the thickness around 500 nm.

The experimental setup is shown in the Fig. 11-1 (d). A broadband source (Exalos) with a center wavelength of 1550 and tunable range of 60 nm was utilized as the light input. The light was coupled into the optical fiber under test with a circulator, and the backscattered light was collected and analysis by a spectrometer (BaySpec). The hydrogen gas was introduced to gas tube with the concentration ranging from 0.25% to 10% at room temperature. The gas flow was fixed to be 20 sccm.

The interference spectrum of the backscattered light is recorded by the spectrometer and shown in Fig. 11-2(a). The spectrum consists of interference fringes were acquired from 1505-nm and 1590-nm produced by Pd-coated FPI trace. The interference fringes are clearly visible showing inference of the backscattered light resulted from laser-enhanced Rayleigh scattering points. The spectral demodulation process was implemented by fast Fourier transform and Buneman frequency estimation to determine the cavity length of both FPIs in real times [21, 22]. Cavity length of Pd-coated IFPI sensors can be obtained from the demodulated IFPI spectrum as shown in Fig. 11-2(b) as 1186 μm.

The time-dependent response of the sensor to various hydrogen concentrations from 0.25% to 10% is shown in the Fig. 11-2(c). Cavity length of Pd-coated FPI sensor increases when exposed to the hydrogen gas at the room temperatures. The cavity length expansion was in proportional to the gas concentrations. A significant elongation of 60 nm was obtained for the cavity when exposed to 10% hydrogen gas. This is correspondence to 50 με tensile strain exerted by Pd film absorption to hydrogen. The smallest hydrogen concentration tested in this experiment was 0.25%, while cavities lengths of FPI sensors expands 9.4 με. Using the Bunemen frequency estimation, a minimal cavity length change of 64 nε can be demodulated using the current set up. Therefore, FPI hydrogen sensors demonstrated in this paper could measure hydrogen concentration significantly lower than 0.25%. However, the ultimate sensitivity of the sensors also depends on sensory film (Pd coating).

The repeatability and reversibility of the FPI sensor was also investigated by introducing multiple cycles of the hydrogen gas followed by the nitrogen flux. The gas flow was also fixed at 20 sccm, and the experiment was carried out at room temperature. The response of sensor to the multiple cycles of gas

exposure with concentrations of 0.5% and 2% are shown in the Fig. 11-2(d). The IFPI hydrogen sensor response time depends on absorption and desorption of hydrogen into Pd films. Fig.11-2(d) shows that the sensor responds to hydrogen absorption into Pd film much more rapidly than when hydrogen was removed from the test chamber. The IFPI sensor response to hydrogen desorption involves two different process as revealed by Fig. 11-2(d), which is due to the phase transition of the palladium hydride.

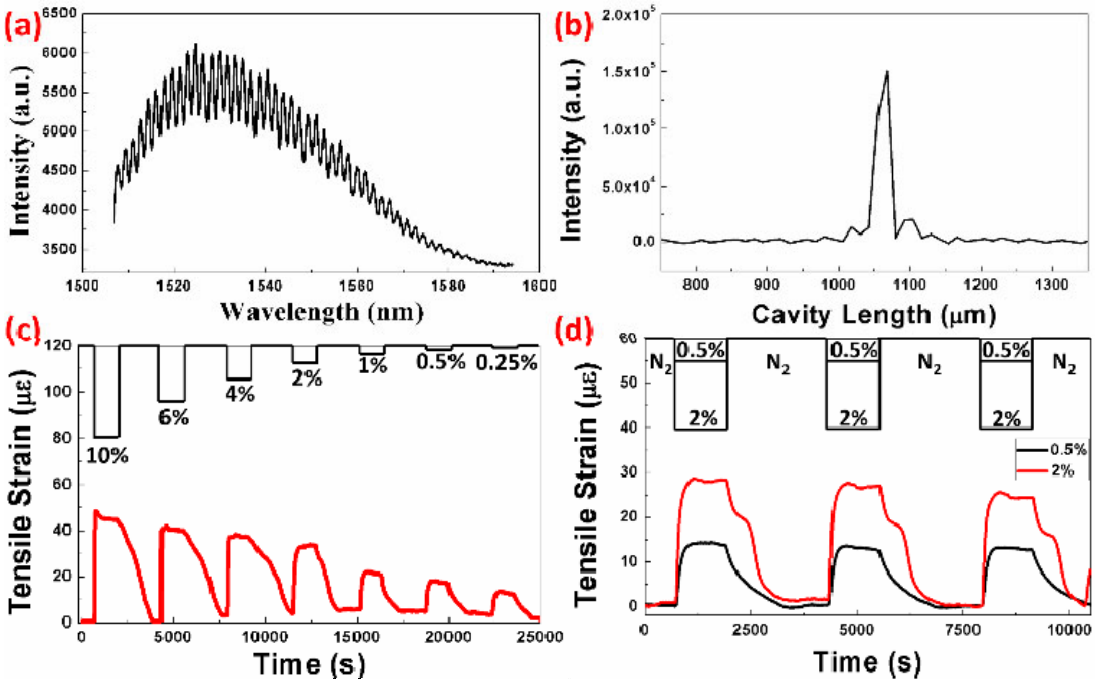

Fig. 11-2. (a) Interference spectrum of the point sensor, (b) demodulated spectrum of the cavity length, (c) time-dependent response of the sensor to various hydrogen concentrations, (d) response of the sensor to multiple cycles of hydrogen exposure with concentration of 0.5% and 2%.

In the figure, a good reproduction of the trace was obtained for both concentrations upon multiple cycles of the hydrogen exposure. For example, the tensile strain change varies within 1.5% when the sensor is characterized under hydrogen gas of 2%, indicating a highly reproducible response. When reduced the gas concentration to 0.5%, a slightly increase of the tensile strain variation to 3% occurs, which still performs repeatable response. Meanwhile, the sensor can be reset back to its initial status in terms of the cavity length for both traces after the introduction of the nitrogen gas, which confirms the reversibility of the FPI sensor.

The underlying mechanism of the enlarged cavity length and its corresponding tensile strain can be explained by the Pd lattice constant expansion when functional coating was exposed to the hydrogen gas. The lattice constant change as well as the volume increase has been observed and quantify in many literatures [23, 24, 25, 26]. The expansion of the fiber and sensory film introduces an axial tensile stain and will be balanced by the shear stress at one point. The tensile strain is a function of the hydrogen partial pressure and can be described by Sievert's law [27]:

$$\varepsilon = \frac{0.026\sqrt{p}}{k}$$

where, p is the hydrogen partial pressure, and k stands for Sievert coefficient (350 $Torr^{1/2}$).

According to the equation, the tensile strain is protentional to the square root of the hydrogen gas partial pressure. To investigate the relationship of tensile stain ε generated by our sensor and the gas levels C, the ratio of the calculated tensile strain of the sensor is plotted in Fig. 11-3(a). The black trace depicts the square root function of the gas concentrations. The gas concentration of 0.25% $C_{0.25\%}$ and its corresponding tensile strain $\varepsilon_{0.25\%}$ were utilized in the experiment as the reference.

In the figure, a good agreement of black trace with the calculated strain ratio of sensory cavity (red square) was observed during the measurement upon all the hydrogen levels, which matches very well the description of the equation 1 and indicates an elastic response of the fabricated sensor. The response speed is also crucial in evaluating the performance of the optical sensor, especially for the monitoring of explosive gas. In this work, the response time of the FPI sensor to various gas concentrations was plotted Fig.11-3(b), and it was defined as the time duration when the tensile strain change of the sensor reached 90% of its maximum value.

In the figure, the response time increases gradually when the hydrogen concentration decreases from 10% to 0.25%, to be more specific, the response required for sensor upon 10% hydrogen exposure is 24 s. However, sensory speed starts to slow down as the response time required for hydrogen gas with the concentration of 0.25% increases to 170 s. Meanwhile, the error ranges also bump from around 4 s to more than 15 s, which can be explained as the less well-defined response of the sensor to the lower hydrogen concentrations. The accelerated response of the sensor referring to the enlarged gas concentrations can be easily understood by the gas diffusion process. The more concentrated gas provides the enlarged hydrogen partial pressure, which facilitates the gas diffusion into the Pd film to form PdH, resulting an increased response speed.

It is also worth noting that the time required for the hydrogen desorption is significantly longer than the response time. This could be explained by the variation of activation energy needed to break the bonds. During the absorption cycle, hydrogen molecules dissociated to H atoms and forms α-phase, which was then transferred into β-phase. The energy required to break the Pd and H atoms during the sensor desorption process is sufficient higher than the force required to break H-H bonding, delays the recovery process of the PFI sensor [28].

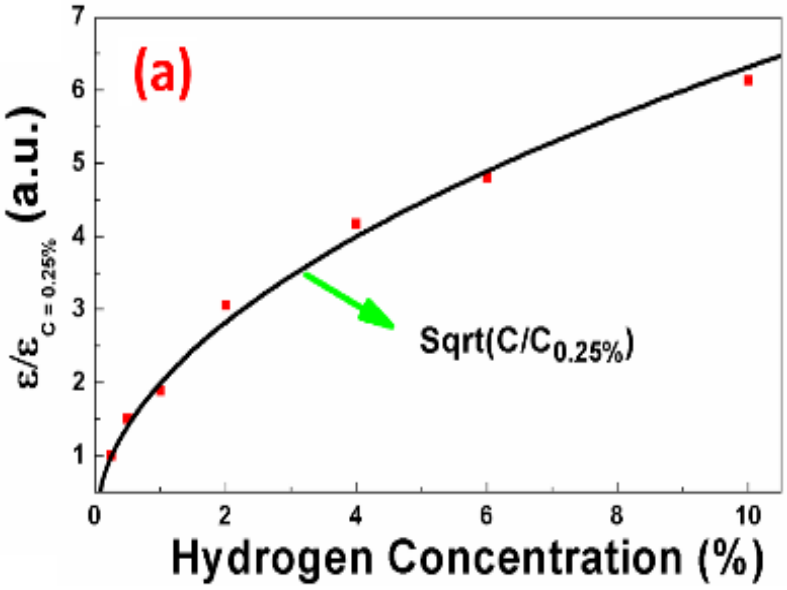

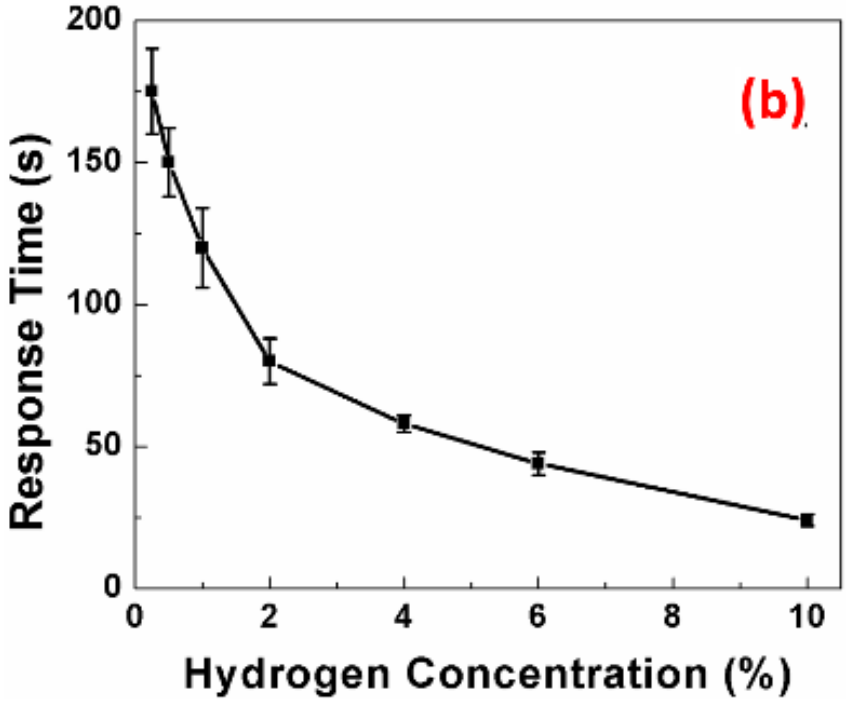

Fig. 11-3. (a) Tensile strain ratio as compared with gas concentration ratio, (b) response speed of the sensor under test.

After thoroughly understanding of the point sensor behavior, the response of IPFI sensor with multiple sensing cavities is also worth investigating. In this case, a multipixel FPI sensor with 7 sensory cavities is fabricated and the response of the sensor is shown in the Fig. 11-4. Interference spectrum and demodulated cavity length of the sensor are shown in the Fig. 11-4(a) and Fig. 11-4(b), respectively. Seven cavities were detected with the length ranging from 489 μm to 1875 μm in the spectrum. Two sensory cavities (cavity 1 and 2) with the length of 489 nm and 684 nm were utilized as the reference points since there is no Pd thin film coated on top of those two cavities.

To characterize the response of the multipixel sensor, a mixture hydrogen gas with concentration ranging from 1% to 8% was introduced into the chamber at room temperature with fixed flow of 20 sccm. The time-dependent behavior of the sensor was characterized, and the relationship of tensile strain from the sensing cavities versus the gas concentrations is plotted in Fig. 11-4(c). In the figure, an increasing level of tensile strain was observed for all the sensory cavities as the level of hydrogen gas elevates, which is within expectation of Sievert's law. Meanwhile, a relatively uniform tensile distribution was observed for all the cavities with functional coating across all the hydrogen levels, indicating a fairly uniform coating of the Pd film. The time-dependent response of sensory cavity 7 is shown in the upper figure of Fig. 11-4(d)with well-defined response. Moreover, the response of the reference sensory point (cavity 2) is also shown in the figure (bottom). No significant response was observed for the reference cavity under all hydrogen levels. This result not only confirms the functionality of the Pd thin film but also eliminates the effect of other aspects in the sensing such as the temperature.

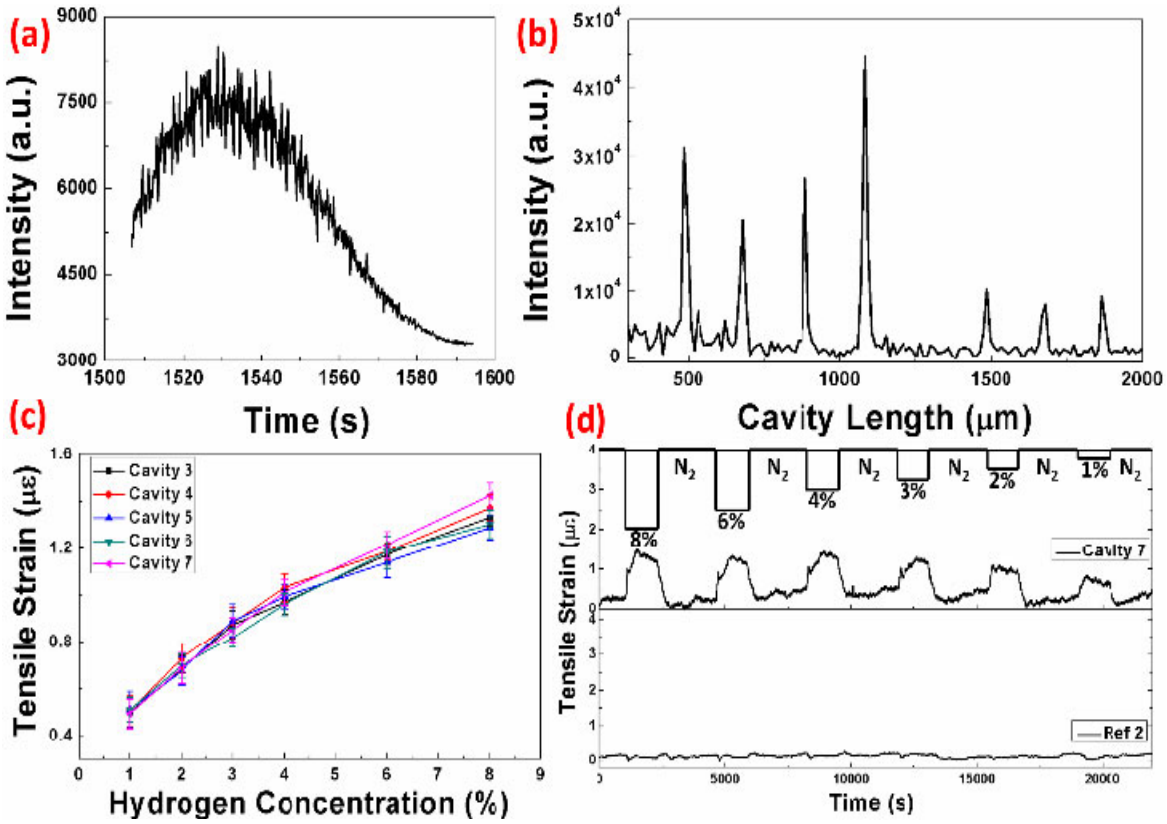

Fig. 11-4. (a) Interference spectrum of the sensor with multiplexing sensory point, (b) demodulated spectrum of the cavity length, (c) tensile strain variation of sensory points upon gas exposure, (d) time-dependent response of the cavity 7 and reference cavity to various hydrogen concentrations.

Summary and Outlook

Summary, we have demonstrated fiber optic hydrogen sensor based on the Fabry-Perot interferometer. The sensing cavity was fabricated through ultrafast laser irradiation, and the variation of demodulated cavity length can be utilized as the indicator for gas levels. The IFPI sensor also show repetitive and reversible response for both point and multipixel sensing applications. The spatial resolution of 5-mm was achieved for multipixel sensor, providing low-cost and easy solution for gas distribution monitoring with high resolutions. In the next quarter, we will perform high temperature sensor testing and proceed to fuel cell tests.

References

1 Yokokawa, H., Tu, H., Iwanschitz, B. & Mai, A. Fundamental mechanisms limiting solid oxide fuel cell durability. *Journal of Power Sources* **182**, 400-412, doi:http://dx.doi.org/10.1016/j.jpowsour.2008.02.016 (2008).

2 Dikwal, C. M., Bujalski, W. & Kendall, K. The effect of temperature gradients on thermal cycling and isothermal ageing of micro-tubular solid oxide fuel cells. *Journal of Power Sources* **193**, 241-248, doi:http://dx.doi.org/10.1016/j.jpowsour.2009.01.097 (2009).

3 Razbani, O., Wærnhus, I. & Assadi, M. Experimental investigation of temperature distribution over a planar solid oxide fuel cell. *Applied energy* **105**, 155-160 (2013).

4 Aydın, Ö., Nakajima, H. & Kitahara, T. Reliability of the numerical SOFC models for estimating the spatial current and temperature variations. *International Journal of Hydrogen Energy* **41**, 15311-15324, doi:http://dx.doi.org/10.1016/j.ijhydene.2016.06.194 (2016).

5 Bedogni, S., Campanari, S., Iora, P., Montelatici, L. & Silva, P. Experimental analysis and modeling for a circular-planar type IT-SOFC. *Journal of Power Sources* **171**, 617-625 (2007).

6 Kreger, S. T., Sang, A. K., Gifford, D. K. & Froggatt, M. E. Distributed strain and temperature sensing in plastic optical fiber using Rayleigh scatter. *Proceedings of SPIE - The International Society for Optical Engineering* **7316**, 73160A-73160A-73168 (2009).

7 Loranger, S., Gagné, M., Lambin-Iezzi, V. & Kashyap, R. Rayleigh scatter based order of magnitude increase in distributed temperature and strain sensing by simple UV exposure of optical fibre. *Scientific Reports* **5**, 11177, doi:10.1038/srep11177 (2015).

8 Buric, M., Ohodnicki, P., Yan, A., Huang, S. & Chen, K. P. in *SPIE Optical Engineering + Applications*. 997708.

9 Smelser, C. W., Mihailov, S. J. & Grobnic, D. Formation of Type I-IR and Type II-IR gratings with an ultrafast IR laser and a phase mask. *Opt. Express* **13**, 5377-5386, doi:10.1364/OPEX.13.005377 (2005).

10 Soller, B. J., Gifford, D. K., Wolfe, M. S. & Froggatt, M. E. High resolution optical frequency domain reflectometry for characterization of components and assemblies. *Opt. Express* **13**, 666-674, doi:10.1364/OPEX.13.000666 (2005).

11 Liao, Y. *et al.* Formation of in-volume nanogratings with sub-100-nm periods in glass by femtosecond laser irradiation. *Opt. Lett.* **40**, 3623-3626, doi:10.1364/OL.40.003623 (2015).

12 Liang, F., Vallée, R. & Chin, S. L. Mechanism of nanograting formation on the surface of fused silica. *Opt. Express* **20**, 4389-4396, doi:10.1364/OE.20.004389 (2012).

13 Rudenko, A., Colombier, J.-P. & Itina, T. E. From random inhomogeneities to periodic nanostructures induced in bulk silica by ultrashort laser. *Physical Review B* **93**, 075427 (2016).

14 Hnatovsky, C. *et al.* Fabrication of microchannels in glass using focused femtosecond laser radiation and selective chemical etching. *Appl Phys A* **84**, 47-61 (2006).

15 Shimotsuma, Y., Kazansky, P. G., Qiu, J. & Hirao, K. Self-Organized Nanogratings in Glass Irradiated by Ultrashort Light Pulses. *Physical Review Letters* **91**, 247405 (2003).

16 Kazansky, P. G. *et al.* Anomalous Anisotropic Light Scattering in Ge-Doped Silica Glass. *Physical Review Letters* **82**, 2199-2202 (1999).

17 Beresna, M. & Kazansky, P. G. Polarization diffraction grating produced by femtosecond laser nanostructuring in glass. *Opt. Lett.* **35**, 1662-1664, doi:10.1364/OL.35.001662 (2010).

18 Froggatt, M. E., Gifford, D. K., Kreger, S., Wolfe, M. & Soller, B. J. Characterization of Polarization-Maintaining Fiber Using High-Sensitivity Optical-Frequency-Domain Reflectometry. *Journal of Lightwave Technology* **24**, 4149-4154 (2006).

19 Lu, P., Grobnic, D. & Mihailov, S. J. Characterization of the birefringence in fiber Bragg gratings fabricated with an ultrafast-infrared laser. *Journal of lightwave technology* **25**, 779-786 (2007).

20 Boffa, V., Blank, D. H. A. & ten Elshof, J. E. Hydrothermal stability of microporous silica and niobia–silica membranes. *Journal of Membrane Science* **319**, 256-263, doi:http://dx.doi.org/10.1016/j.memsci.2008.03.042 (2008).

21 Wang, T., Shao, L.-Y., Canning, J. & Cook, K. Temperature and strain characterization of regenerated gratings. *Opt. Lett.* **38**, 247-249, doi:10.1364/OL.38.000247 (2013).

22 T. M. Monro, P. J. Bennett, N. G. R. Broderick, and D. J. Richardson, "Holey fibers with random cladding distributions," Opt. Lett. 25 (4), 206-208 (2000).

23 D. Kominsky, G. Pickrell, and R. Stolen, "Generation of random-hole optical fiber," Opt. Lett. 28 (16), 1409-1411 (2003).

24 M. Li, P. Tandon, D. C. Bookbinder, D. A. Nolan, S. R. Bickham, M. A. McDermott, R. B. Desorcie, J. J. Englebert, S. L. Logunov, V. Kozlov, and J. A. West, "Nano-Engineered Optical Fibers and Applications,"OFC2010, paper OWA2.

25 T. M. Monro, D. J. Richardson, N. G. R. Broderick, and P. J. Bennett, "Holey optical fibers: an efficient modal model," J. Lightwave Tech. 17 (6), 1093-1102 (1999).

26 P.E. Sanders, “Fiber-Optic Sensors: Playing Both Sides of the Energy Equation,” Opt. Photon. News 22 (1) 36-42 (2011).

27 T. Wijnands, L.K. DeJonge, J. Kuhnhenn, S.K. Hoeffgen and U. Weinand, “Optical absorption in commercial single mode optical fibers in a high energy physics radiation field,” IEEE Trans. Nucl. Sci. 55 (4), 2216-2222 (2008).

28 S. J. Mihailov, “Fiber Bragg grating sensors for harsh environments,” Sensors 12(2), 1898-1918 (2012).

29 S. J. Mihailov, D. Grobnic, C. W. Smelser, P. Lu, R. B. Walker, and H. Ding, "Bragg grating inscription in various optical fibers with femtosecond infrared lasers and a phase mask," Optical Materials Express 1 (4), 754-765 (2011).

30 S. J. Mihailov, C. W. Smelser, D. Grobnic, R. B. Walker, P. Lu, H. Ding, and J. Unruh, "Bragg Gratings Written in All-SiO 2 and Ge-Doped Core Fibers With 800-nm Femtosecond Radiation and a Phase Mask," J. Lightwave Tech. 22 (1), 94-100 (2004).

31 S. J. Mihailov, D. Grobnic, H. Ding, C. W. Smelser, and J. Broeng, "Femtosecond IR Laser Fabrication of Bragg Gratings in Photonic Crystal Fibers and Tapers," IEEE Photon. Technol. Lett., 18 (17), 1837-1839 (2006).

32 C. W. Smelser, S. J. Mihailov, and D. Grobnic, "Formation of Type I-IR and Type II-IR gratings with an ultrafast IR laser and a phase mask," Opt. Exp. 13 (14), 5377-5386 (2005).

33 A. Martinez, I. Y. Khrushchev, and I. Bennion, "Thermal properties of fibre Bragg gratings inscribed point-by-point by infrared femtosecond laser," Electron. Lett. 41 (4), 176-178 (2005).

34 D. Grobnic, C. W. Smelser, S. J. Mihailov, and R. B. Walker, "Long-term thermal stability tests at 1000 °C of silica fibre Bragg gratings made with ultrafast laser radiation," Meas. Sci. Tech. 17 (5), 1009-1013 (2006).

35 S. J. Mihailov, C. W. Smelser, P. Lu, R. B. Walker, H. Ding, D. Grobnic, G. Henderson, and J. Unruh, "Fiber Bragg gratings made with a phase mask and 800-nm femtosecond radiation," Opt. Lett. 28(12), 995-997 (2003).

36 A. Martinez, M. Dubov, I. Khrushchev, and I. Bennion, "Direct writing of fibre Bragg gratings by femtosecond laser," Electron. Lett. 40 (19), 1170-1172 (2004).

37 K. Zhou, M. Dubov, C. Mou, L. Zhang, V. K. Mezentsev, and I. Bennion, "Line-by-Line Fiber Bragg Grating Made by Femtosecond Laser," IEEE Photon. Technol. Lett., 22 (16), 1190-1192 (2010).

38 R. J. Williams, R. G. Krämer, S. Nolte, and M. J. Withford, "Femtosecond direct-writing of low-loss fiber Bragg gratings using a continuous core-scanning technique," Opt. Lett. 38 (11), 1918-1920 (2013).

39 S. C. Warren-Smith, L. V. Nguyen, C. Lang, H. Ebendorff-Heidepriem, and T. M. Monro, "Temperature sensing up to 1300°C using suspended-core microstructured optical fibers," Opt. Express 24 (4), 3714-3719 (2016).

40 P. Tandon, M.-J. Li, D. C. Bookbinder, S. L. Logunov and E.J. Fewkes, "Nano-engineered optical fibers and applications," Nanophotonics 2 (5-6), 383-392 (2013).

41 C. Hnatovsky, D. Grobnic, and S. J. Mihailov, "Nonlinear photoluminescence imaging applied to femtosecond laser manufacturing of fiber Bragg gratings," Opt. Express 25 (13), 14247-14259 (2017).

42 C. W. Smelser, D. Grobnic, and S. J. Mihailov, "Generation of pure two-beam interference grating structuresin an optical fiber with a femtosecond infrared source anda phase mask," Opt. Lett. 29 (15), 1730-1732 (2004).

43 F. Liu, K. M. Yoo, and R. R. Alfano, "Speed of the coherent component of femtosecond laser pulses propagating through random scattering media," Opt. Lett. 16 (6), 351-353 (1991).

44 C. Hnatovsky, D. Grobnic, D. Coulas, M. Barnes, and S. J. Mihailov, "Self-organized nanostructure formation during femtosecond-laser inscription of fiber Bragg gratings," Opt. Lett. 42 (3), 399-402 (2017).

45 C. Hnatovsky, R. S. Taylor, P. P. Rajeev, E. Simova, V. R. Bhardwaj, D. M. Rayner, and P. B. Corkum, "Pulse duration dependence of femtosecond-laser-fabricated nanogratings in fused silica," Appl. Phys. Lett. 87 (1), 014104 (2005).

46 E. Bricchi and P. G. Kazansky, "Extraordinary stability of anisotropic femtosecond direct-written structures embedded in silica glass," Appl. Phys. Lett. 88 (11), 111119 (2006).

47. Z. Zhao and M. A. Carpenter, "Annealing enhanced hydrogen absorption in nanocrystalline PdAu sensing films," *J. Appl. Phys.*, vol. 97, no. 12, 2005.

Efforts on Developing Reel-to-Reel Fabrication Schemes to Produce Fiber Sensors with Exceptional High Temperature Stability

In this period, we developed a method of reel-to-reel femtosecond laser direct writing that enables the continuous inscription of low-loss and high-temperature stable Rayleigh scattering centers inside the core of single-mode optical fibers for distributed temperature sensing up to 1000°C. By examining the correlation between the Rayleigh backscattering profile and the cross-section morphology of femtosecond laser-induced nanograting in fiber cores, this report reveals the mechanisms that underlie the fabrication of high-temperature stable distributed fiber sensors with low loss. By fine-tuning laser exposure conditions, the femtosecond laser-fabricated Rayleigh scattering enhanced section could achieve an optimized propagation loss of 0.01 dB/cm with an increased signal-to-noise ratio of over 35 dB for meters of lengths.

Section 12-1: Previous Efforts and Challenges

Otical fibers serve as excellent sensor platforms due to their exceptional stability at extreme temperatures, robust immunity to electromagnetic interference and chemical pollution, as well as resilience to radiation. These desirable traits enable the development of optical fiber sensors for use in harsh environment conditions.

Utilizing the intrinsic Rayleigh scattering processes in unmodified optical fibers, optical fibers can be used as distributed fiber sensors to monitor physical parameter changes along the fiber with high spatial resolution. Using Rayleigh scattering-based Optical Frequency-Domain Reflectometry (OFDR), distributed temperature and strain measurements can be performed to achieve sub-cm spatial resolution on standard telecommunication fibers. However, for commercial optical fibers, scattering is minimized by optimized processes of fiber fabrication, as it induces undesired loss in fiber communication. As a result, the performance of Rayleigh scattering-based distributed fiber sensors is limited by the weak signals generated from Rayleigh scattering [1-8]. To address this challenge, Ultraviolet (UV) laser was used to create artificial Rayleigh scattering centers in photosensitized or photosensitive optical fibers. Previous work has demonstrated that increased Rayleigh scattering signal led to improved performance in OFDR-based distributed temperature and strain sensing [2, 3]. The UV-enhanced distributed fiber strain sensors have also been used in medical applications for shape sensing [4]. Despite these improvements, the UV inscription process requires specialty photosensitive fibers or additional pre-processing steps such as hydrogen loading. Moreover, the performance of the UV sensor would degrade at extreme temperatures, making it less suitable for applications in harsh environments.

The femtosecond laser has emerged as a promising technique in the fabrication of fiber sensors, especially for use in harsh environments [5]. Random gratings induced by femtosecond laser direct writing have been reported to enhance the scattering signal for application in OFDR-based distributed temperature sensing. By varying either the fiber writing speed or laser repetition rate, random gratings can be generated to increase the sensing accuracy [6, 7]. However, the random grating with ultra-low loss [6] was generated by the femtosecond laser-induced homogeneous refractive index change (Type-I-fs), and thus is not suitable for long-term

monitoring of a temperature range larger than 500°C [8, 9]. Meanwhile, at a higher inscription pulse energy, another femtosecond laser-material interaction regime takes place, characterized by the formation of high-temperature stable nanostructures (Type-II-fs) [9-11], that has exhibited exceptional harsh environment endurance over 1000°C [12]. First observed in 2003, the femtosecond laser induced nanograting is widely used for femtosecond laser selective etching for microfluidic channels [13] and FBGs for harsh environment applications [14, 15].

Supported by this research grant, high-temperature stable sensors that exploit femtosecond laser-induced nanograting as Rayleigh scattering centers, were tested in a reactive hydrogen gas environment with temperatures up to 800°C. These efforts have been documented in this reports as part of our preivous efforts.

The Rayleigh enhanced section has proven to be functional in both nuclear reactor cores [16] and internal to solid oxide fuel cells [17]. However, the sensors suffer from high propagation loss of 0.15 dB/cm, thus, the sensing range is limited.

In this period, we carried out a reel-to-reel femtosecond laser direct writing technique to inscribe Rayleigh scattering centers, that are low-loss and thermally stable at high temperatures up to 1000°C, in optical fiber cores for OFDR-based distributed temperature sensing. **We found that by precisely tuning the laser exposure conditions, a signal-to-noise ratio (SNR) enhancement between 35 dB to 55 dB in Rayleigh backscattering signal and low propagation loss of 0.01 dB/cm was achieved.** Cross-section morphology was observed under the Scanning Electron Microscope (SEM) to reveal the correlation between Rayleigh enhancement and the morphology of laser-induced nanograting formed in fiber cores. Using a reel-to-reel setup, meters of Rayleigh enhancement were conveniently fabricated in the core of single-mode silica optical fiber for distributed fiber sensors, demonstrating improved thermal stability, signal-to-noise ratio, and measurement resolution.

Section 12-2: Sensor Fabrication:

Similar to our previous studies, a Coherent Ti:sapphire regenerative femtosecond laser system was used for fiber sensor fabrication, focusing 800-nm, 270-fs, and 250-kHz light through a 100X 1.25-NA oil-immersion objective. The spot of laser focus was aligned with the center of the optical fiber core with the help of a high-precision motorized stage (Aerotech ABL2000). To achieve continuous femtosecond laser inscription, the fiber was translated using a customized reel-to-reel setup at a constant speed. Laser beam is linearly polarized, with its direction of polarization perpendicular to the direction of fiber translation. The backscattering behavior of the fiber sample was probed using a commercial Optical Backscattering Reflectometer (OBR, Luna 4600), as illustrated schematically in Fig. 12-1(a). An example of the OBR backscattering profile of a Rayleigh enhanced section that is over 3 meters long is presented in Fig. 12-1(b).

For the reel-to-reel fabrication setup, a compact fiber mount made by a 3-D printer was used to maintain the laser focus spot in the center of the fiber core during continuous Rayleigh scattering center writing (Fig. 12-1(c)). Altogether a customized pulley system and a motorized rotation stage, the inscription of meters of fiber sensor were enabled with simple alignment procedure. Fig.12-1(d) shows the sideview of the Rayleigh enhanced section under the optical microscope, with a continuous modification track in the center of the fiber core. Afterwards, the

fiber was cleaved at the section of femtosecond laser modification to examine its cross-section morphology using the SEM. The SEM photo in Fig. 12-1(e) shows the formation of a self-organized nanostructure with sub-wavelength period at the fiber core, whose morphology is consistent with previous observation of the femtosecond laser-induced self-organized nanograting [8, 18].

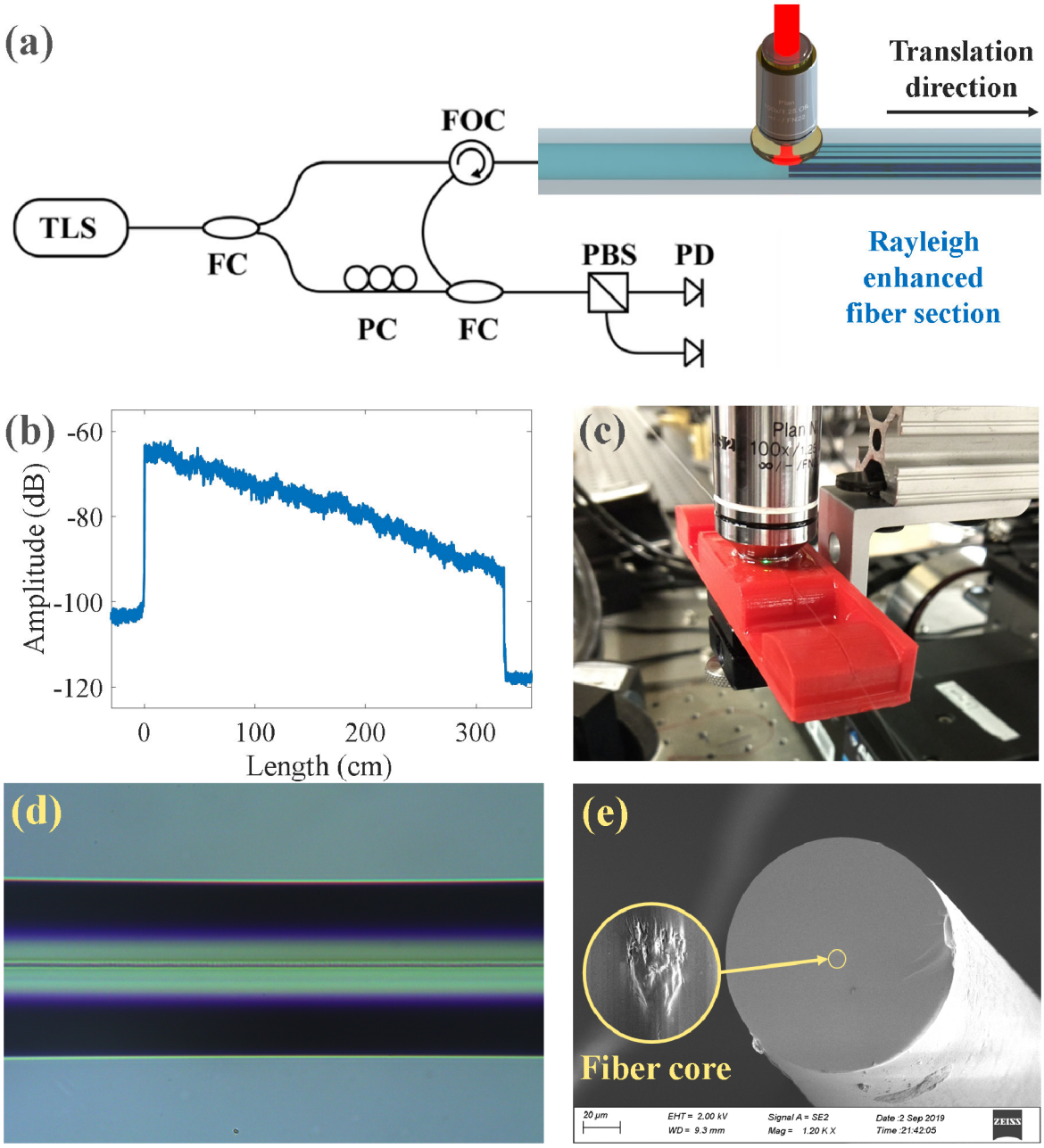

Fig. 12-1. (a) Schematic of the fabrication setup, (b) the Rayleigh backscattering profile of a 325-cm Rayleigh enhanced section, (c) photo of a segment of the reel-to-reel setup, (d) the microscopic photo of the fiber sideview, and (e) the SEM photo of the fiber cross-section; inset shows the zoomed-in image with nanograting in the fiber core.

Section 12-3: Nanograting Engineering and Optimization:

SEM studies of nanograting formation in correlation to the Rayleigh backscattering profile provide tell-tale clues on how to further optimize the fabrication process. Fig. 12-2(a-e) show the OBR measured backscattering profiles of Rayleigh enhanced sections on a standard silica-core single-mode optical fiber (Corning SMF28e+) written with 160, 140, 120, 100, and 80-nJ inscription laser pulse energies, at a constant speed of 0.5 mm/s, while their SEM photos in Fig. 12-2(f-j) revealed significant cross-section morphology variations in correlation to the OBR profiles. At a pulse energy below 60-nJ, no change in the Rayleigh backscattering profile could be measured, since the pulse energy is lower than the threshold of making Type I refractive index change in the fiber. At a pulse energy between 60 nJ and 100 nJ, an increase in the backscattering signal occurred, while there was no visible morphology modification (Fig. 12-2(j)). This is the regime where the multiphoton absorption process induces a low-loss homogeneous refractive index modification, that is typically used to fabricate waveguide for integrated photonic circuit [10, 11]. Loss can be identified in Fig. 2(e). This can be explained by the localized refractive index change modification region with the size much smaller than the fiber core, resulting in a coupling loss due to the mismatch between the femtosecond laser induced waveguide-like structure and the fundamental mode of the optical fiber. When pulse energy was higher than 100 nJ, an anisotropic nanostructure was observed in the fiber core (Fig. 12-2(f-i)), indicating the regime of laser-induced nanograting formation.

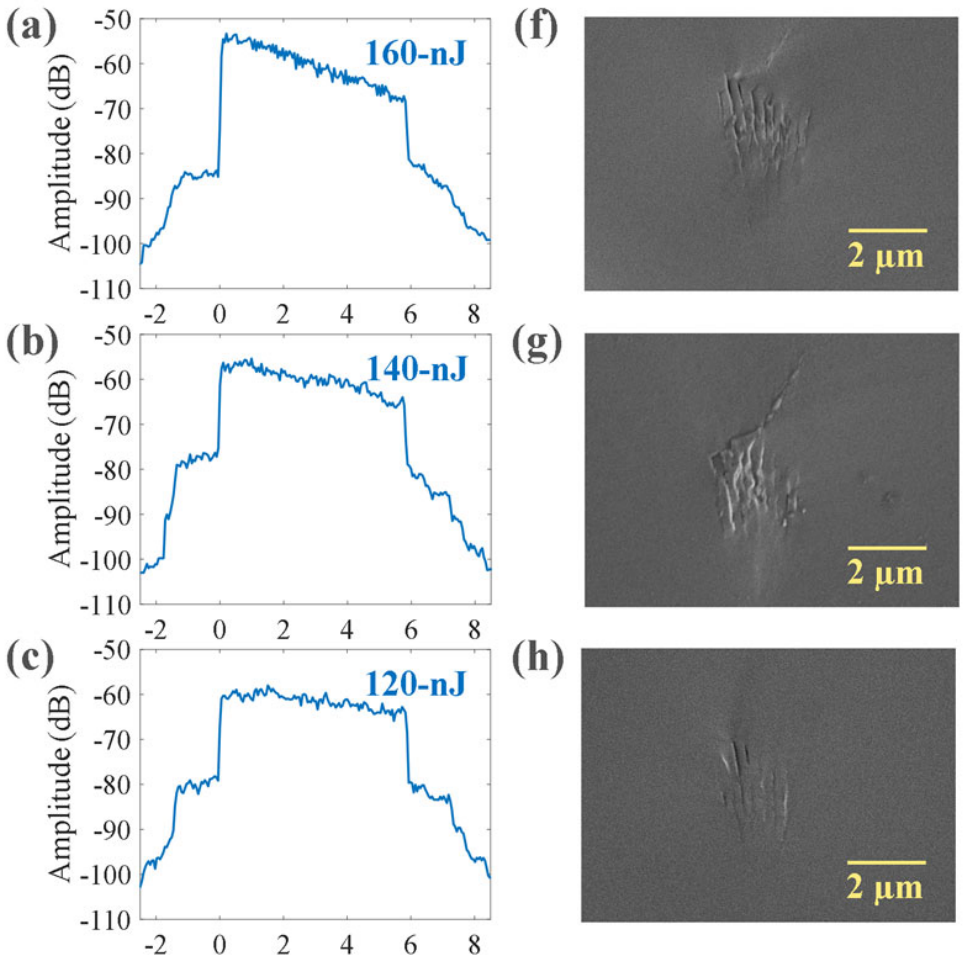

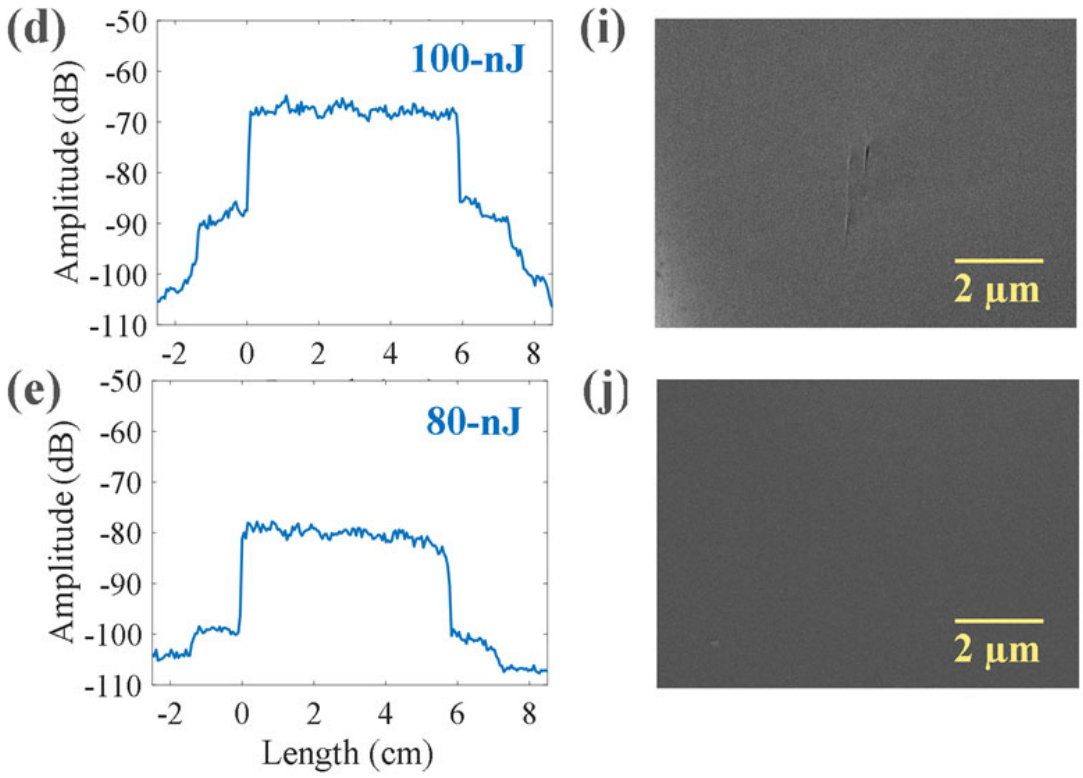

Fig. 12-2: (a-e) Rayleigh backscattering profiles and (f-j) SEM photos of fiber core cross-section morphology of the Rayleigh enhanced sections fabricated using 160, 140, 120, 100-nJ, and 80-nJ pulse energies, respectively.

Fig. 12-3 summarizes the dependence of OBR-measured propagation loss and SNR enhancement on the fabrication pulse energy at the pulse energies that allows the formation of high-temperature stable nanograting. The propagation loss is calculated from the linear fit of the optical OBR measured return loss [19, 20], and the SNR enhancement is measured from the increase in returned backscattering signal of the Rayleigh enhanced fiber section as compared to the unmodified fiber section, where only intrinsic Rayleigh scattering exists [21]. A general relationship that is revealed from the OBR profile suggests that with an increase in laser pulse energy, both the SNR enhancement and the propagation loss increase. This is consistent with the SEM observations (Fig. 12-2(f-i)), showing an increased size of the nanograting with increasing pulse energy [22, 23]. The controllability of loss and enhancement on pulse energy is a result of the distortion-free oil-immersion objective used during the fabrication process. Because of the high Numerical Aperture of the objective, the laser-induced nanograting size is much smaller than the size of the fiber core, and thus, the larger physical modification caused by nanograting increases the size of inhomogeneity inside the fiber core, resulting in a higher Rayleigh backscattering signal and scattering loss measured at the interrogator [24, 25]. As such, precise tuning of the Rayleigh enhanced section is enabled. By optimizing the conditions of laser exposure, the optimized exposure condition in SMF28e+ was found at 100-nJ, with a minimum loss of 0.01-dB/cm and an SNR enhancement of over 35-dB. This can be explained by the relatively small nanograting size formed at 100-nJ pulse energy (Fig. 12-2(i)), especially since 100-nJ is close to the threshold energy between the femtosecond laser-induced refractive index modification regime and the nanograting formation regime.

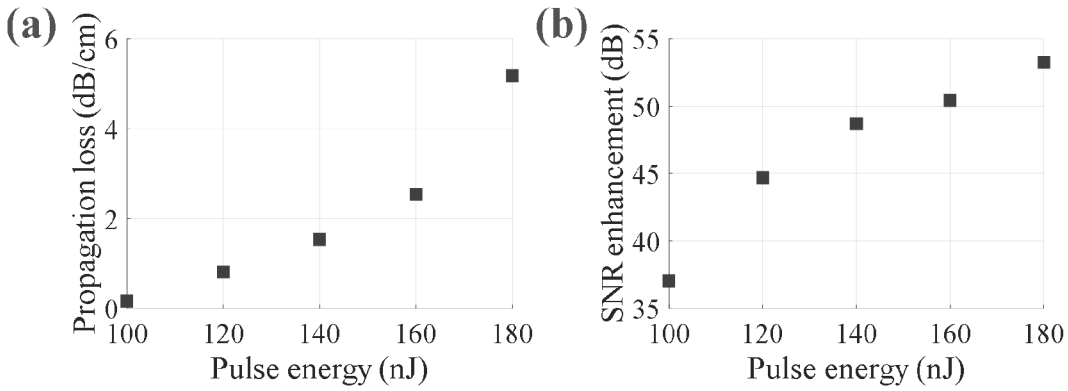

Fig. 12-3. Dependence of (a) propagation loss and (b) SNR enhancement on the exposure pulse energy.

Due to its asymmetric morphology, birefringence is introduced in optical fiber during the formation of nanograting. By simultaneously monitoring the two orthogonal s and p polarization states in the OBR-measured Rayleigh backscattering profile, the formation of nanograting can be identified using a non-invasive approach during fabrication [15, 21]. Fig. 12-4(a-d) show polarization states of the Rayleigh enhanced section written with a pulse energy of 140, 120, 100, and 80-nJ, respectively. No preference in polarization can be seen at 80-nJ (Fig. 4(d)), indicating the material modification is in the regime of isotropic positive refractive index change, consistent with the SEM observation in Fig. 12-2(j). Meanwhile, as pulse energy reaches 100-nJ and beyond, beating occurs in the two polarizations. The birefringence of 140, 120, and 100-nJ profiles (Fig. 4(a-c)) were calculated to be 9.9×10^{-4}, 2.7×10^{-4}, and 0.8×10^{-4}, respectively, which is due to the increased birefringent nanograting size (Fig. 12-2(g-i)). Compared to the low birefringence of $\sim 10^{-7}$ for unmodified single-mode optical fiber (Corning SMF28e+), the scattering centers produce an approximate increase of three orders of magnitude in the in-fiber birefringence, which is consistent with previous descriptions of the in-fiber birefringence induced by nanograting [26, 27].

Section 12-4: Summary

By examining the correlation between the Rayleigh backscattering profile and the cross-section morphology of femtosecond laser-induced nanograting in fiber cores, research finding here reveals the mechanisms that underlie the fabrication of high-temperature stable distributed fiber sensors with low loss. By fine-tuning laser exposure conditions, the femtosecond laser-fabricated Rayleigh scattering enhanced section could achieve an optimized propagation loss of 0.01 dB/cm with an increased signal-to-noise ratio of over 35 dB for meters of lengths. Through combined research efforts on microstructure studies and laser processing parameter tuning, we show that distributed fiber sensors can be fabricated with exceptionally low loss.

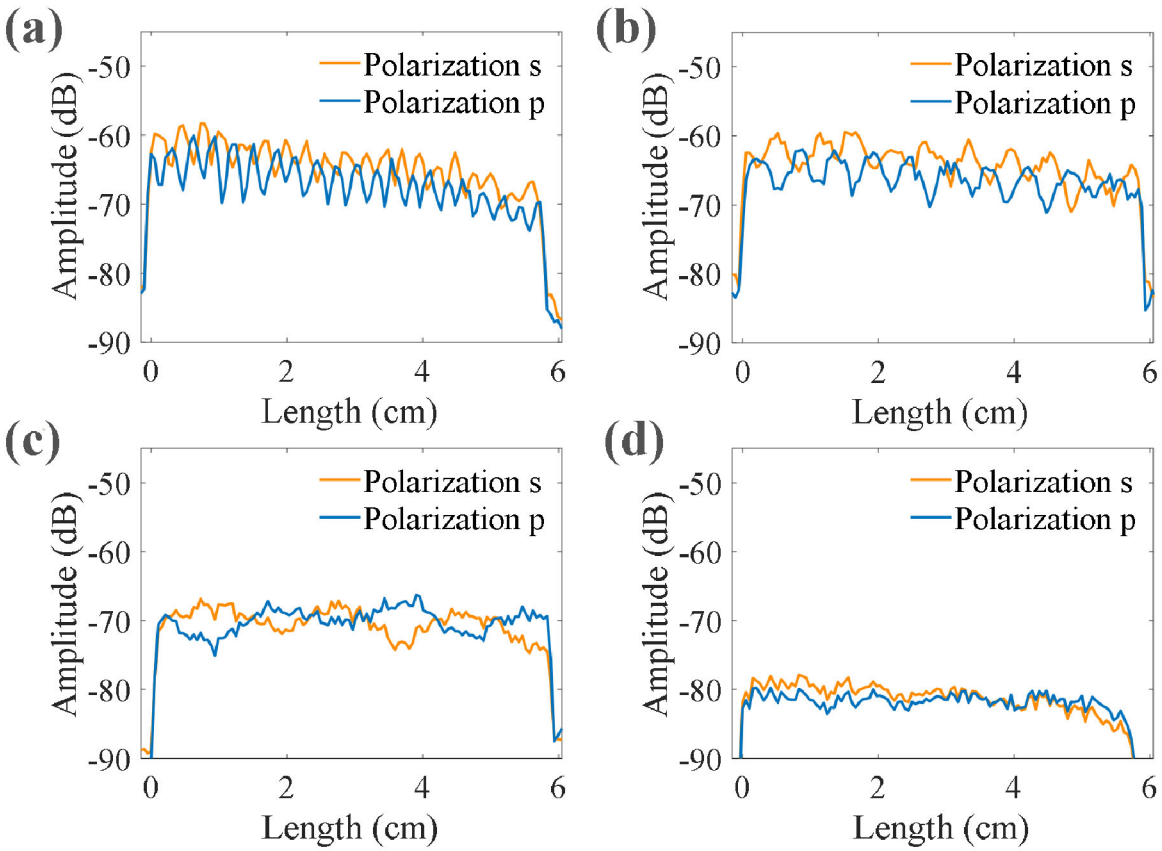

Fig. 12-4. The s and p polarization states of the OBR-measured Rayleigh backscattering profiles, written with pulse energies of (a) 140 nJ, (b) 120 nJ, (c) 100 nJ, and (d) 80 nJ, respectively.

Section 13-1: Studies of High Temperature Stabilities

For high-temperature stability tests, a Rayleigh enhanced section fabricated with 100-nJ pulse energy and 1-mm/s speed was first annealed at 1000°C for 20-hours and subjected to repeated heating and cooling cycles. Each cycle started from the ambient temperature, then rose to 1000°C at a rate of 5°C/min, remaining stable at each step of 100°C for 1-hour, followed by cooling at the natural rate from 1000°C back to the ambient. The temperature inside the box furnace was monitored with a Type-K thermocouple, and the Rayleigh enhanced sample was examined using the OBR every 10 minutes with 0.5-cm spatial resolution. Fig. 13-(a) shows the profile change right after the fabrication, after annealing, and during each heating and cooling cycle. The characteristic curve for each cycle was calculated (Fig. 13-1(b)), as the sensitivity was measured to be -0.66 GHz/°C. The sensor was thermally stable throughout the temperature cycling, with no obvious change in the backscattering profile. Afterwards, the Rayleigh enhanced section was kept at a constant temperature of 1000°C for 16 hours, in order to verify the long-term thermal stability of the sensor. After 16 hours, it was still able to keep deriving

correct temperature measurements from the Rayleigh enhanced section, using the ambient temperature profile as a reference, while the performance of the unmodified optical fiber degraded at 1000°C (Fig. 13-1(c)). This is probably due to the nanograting induced permanent physical modification exhibits better thermal stability at 1000°C than the intrinsic Rayleigh backscattering signal caused by inhomogeneities in fiber core. Fig. 13-1(d) represents the averaged spectral shift quality of both the Rayleigh enhanced fiber section and the unmodified fiber section over the time period of 16 hours at 1000°C, using the profile at the 0 hour at 1000°C as a reference. The range of spectral quality is a number between 0 and 1, which evaluates the quality of the cross-correlation in OFDR-based sensing [28, 29]. Overall, the Rayleigh enhanced section exhibited significantly improved high-temperature stability over a long term.

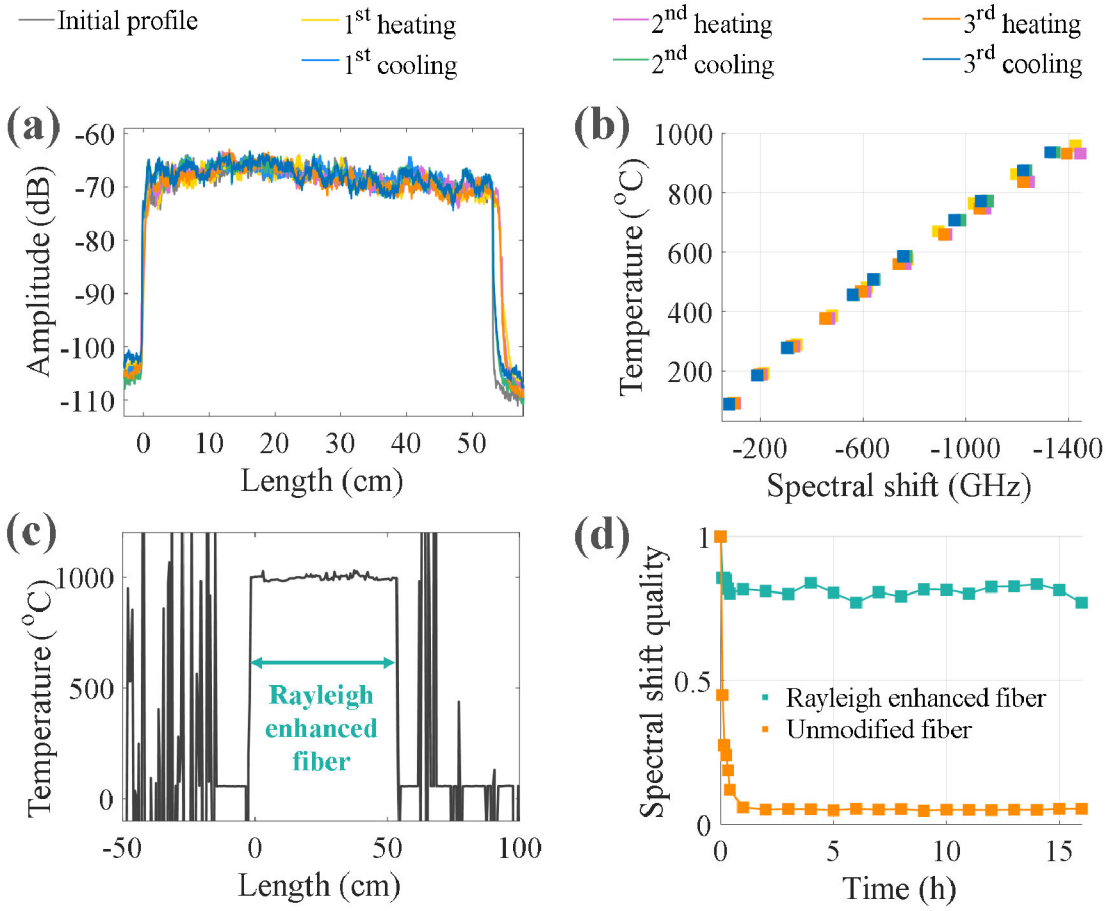

Fig. 13-1. (a) The Rayleigh backscattering profile change and (b) the characterization curve during high-temperature test cycles, and (c) the temperature measurement after three temperature cycles and 16 hours at 1000°C, and (d) the spectral shift quality change of the Rayleigh enhanced fiber section and unmodified fiber during 16 hours at 1000°C.

With a combination of laser exposure tuning and reel-to-reel fabrication, a 137-cm Rayleigh enhancement section was written with 35-dB Rayleigh backscattering enhancement and 0.01-

dB/cm loss (Fig. 13-2(a)). The fiber sample was placed inside a thermally insolated container for 12 hours. Spectral shift quality of the Rayleigh enhanced section exhibits superior performance and the RMS noise was measured to be 0.012°C with a spatial resolution of 1-cm, that is about four times better than the unmodified sections measured to be at 0.054°C (Fig. 13-2(b)).

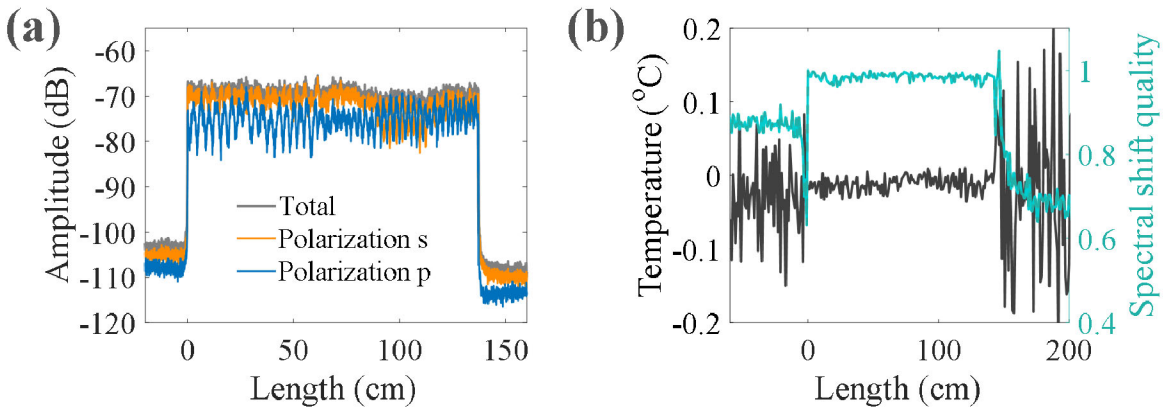

Fig. 13-2 (a) The Rayleigh backscattering profile of a 137-cm Rayleigh enhanced section and (b) the OBR-measured temperature variation (right) and spectral shift quality (left) at room temperature.

The fabrication process is highly flexible and can be used for other fiber geometries. The random airline-cladding (RAL) pure-silica core optical fiber is a promising candidate for application in harsh environments. Compared to the commercial single-mode fibers with Ge-doped silica fiber core, the RAL fiber is pure silica as with a cladding region composed of thousands of air holes [30, 31]. Similarly, continuous Rayleigh scattering centers were induced in RAL fiber and the propagation loss and SNR enhancement dependency on pulse energy were characterized in Fig. 13-1(a). The pulse energy was increased to compensate for distortion of the laser focus from scattering in the random air hole cladding. Despite the scattering at the random airlines, the fabrication process was able to inscribe a highly localized modification area inside the fiber core with no damage to the fiber cladding, as presented in the SEM photo in Fig. 13-2(b).

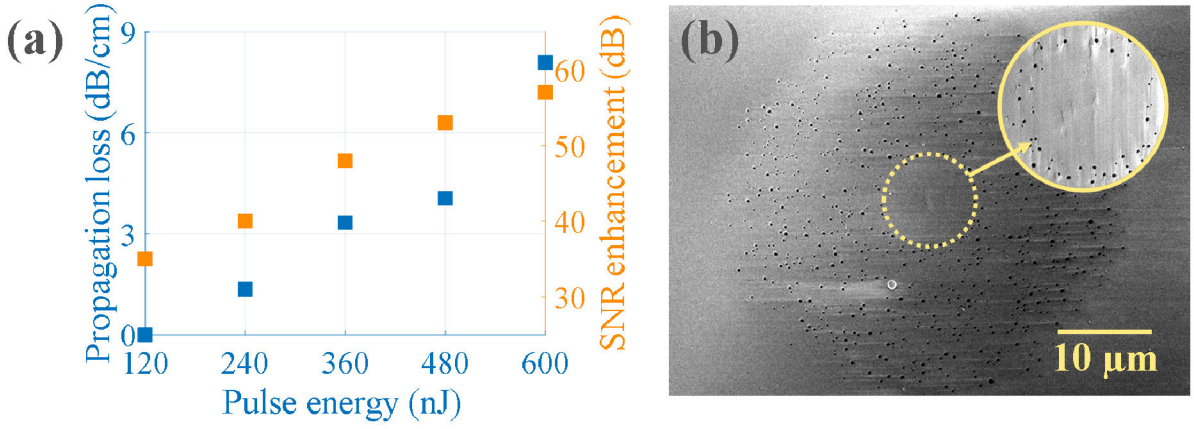

Fig. 13-3: (a) Dependence of pulse energy and loss of Rayleigh enhanced section in RAL fiber and (b) SEM photo of RAL fiber cross-section; inset is a zoomed-in image showing nanograting formation in the fiber core.

Summary

In conclusion, resaerch works carried out in 2020 present a novel method of reel-to-reel femtosecond laser direct writing that enhances Rayleigh scattering on silica optical fiber for distributed temperature sensing. By studying the correlation between the Rayleigh scattering profile and the femtosecond laser-induced high-temperature stable nanograting in fiber core at the Rayleigh enhanced section, this paper outlines a method to fine-tune the fabrication conditions to produce meters of optical fibers with an enhanced Rayleigh scattering profile and low propagation loss. We demonstrated improved high-temperature stability and signal-to-noise ratio in repeated cycles for temperature up to 1000°C. Furthermore, by monitoring the birefringence, formation of high-temperature stable nanograting can be verified non-invasively. We also demonstrate the flexibility of the laser fabrication method in both standard telecommunication fiber and random airline-cladding fiber. The research presented in this paper opens powerful perspectives to fabricate high-quality and high-temperature stable optical fiber sensors with extended lengths for sensing applications in harsh environment.

REFERENCES

[1] X. Bao, and L. Chen, "Recent progress in distributed fiber optic sensors," Sensors, vol. 12, no. 7, pp. 8601-8639, Jul. 2012.

[2] F. Monet, S. Loranger, V. Lambin-Iezzi, A. Drouin, S. Kadoury, and R. Kashyap, "The ROGUE: a novel, noise-generated random grating," Opt. Express, vol. 27, no. 10, pp. 13895-13909, May 2019.

[3] S. Loranger, F. Parent, V. Lambin-Iezzi, and R. Kashyap, “Enhancement of Rayleigh scatter in optical fiber by simple UV treatment: an order of magnitude increase in distributed sensing sensitivity,” in Opt. Components and Mat. XIII, Feb. 2016, pp. 97440E.

[4] F. Parent, S. Loranger, K. K. Mandal, V. Lambin-Iezzi, J. Lapointe, J. Boisvert, M. D. Baiad, S. Kadoury, and R. Kashyap, "Enhancement of accuracy in shape sensing of surgical needles using optical frequency domain reflectometry in optical fibers," Bio. Opt. Express, vol. 8, no. 4, pp. 2210-2221, Apr. 2017.

[5] S. J. Mihailov, "Fiber Bragg grating sensors for harsh environments," Sensors, vol. 12, no. 2, pp. 1898-1918, Feb. 2012.

[6] P. Lu, S. Mihailov, D. Coulas, H. Ding, and X. Bao, "Low Loss Random Fiber Gratings Made with an fs-IR Laser for Distributed Fiber Sensing," J. Lightwave Technol., vol. 37, no. 18, pp. 4697-4702, Sep. 2019.

[7] Y. Xu, P. Lu, S. Gao, D. Xiang, S. Mihailov, and X. Bao, "Optical fiber random grating-based multiparameter sensor," Opt. Lett., vol. 40, no. 23, pp. 5514-5517, Dec. 2015.

[8] E. Bricchi, and P. G. Kazansky, "Extraordinary stability of anisotropic femtosecond direct-written structures embedded in silica glass," Appl. Phys. Lett., vol. 88, no. 11, pp. 111119, Mar. 2006.

[9] C. W. Smelser, S. J. Mihailov, and Dan Grobnic, "Formation of Type I-IR and Type II-IR gratings with an ultrafast IR laser and a phase mask," Opt. Express, vol. 13, no. 14, pp. 5377-5386, Jul. 2015.

[10] R. Osellame et al, “Femtosecond laser micromachining: photonic and microfluidic devices in transparent materials,” in Applied Physics, vol.123. Berlin, Germany: Springer Science & Business Media, 2012.

[11] K. Itoh, W. Watanabe, S. Nolte, and C. B. Schaffer, "Ultrafast processes for bulk modification of transparent materials," MRS Bull, vol. 31, no. 8, pp. 620-625, Aug. 2016.

[12] D. Grobnic, C. W. Smelser, S. J. Mihailov, and R. B. Walker, "Long-term thermal stability tests at 1000° C of silica fibre Bragg gratings made with ultrafast laser radiation," MST, vol. 17, no. 5, pp. 1009, Apr. 2006.

[13] M. Haque, K. Lee, S. Ho, L. A. Fernandes, and P. R. Herman, "Chemical-assisted femtosecond laser writing of lab-in-fibers," LOC, vol. 14, no. 19, pp. 3817-3829, Jul. 2014.

[14] S. J. Mihailov, D. Grobnic, C. Hnatovsky, R. B. Walker, P. Lu, D. Coulas, and H. Ding, "Extreme environment sensing using femtosecond laser-inscribed fiber Bragg gratings," Sensor, vol. 17, no. 12, pp. 2909, Dec. 2017.

[15] C. Hnatovsky, D. Grobnic, D. Coulas, M. Barnes, and S. J. Mihailov, "Self-organized nanostructure formation during femtosecond-laser inscription of fiber Bragg gratings," Optics Letters, vol. 42, no. 3, pp. 399-402, Feb. 2017.

[16] M. Wang, M. Zaghloul, S. Huang, A. Yan, S. Li, R. Zou, P. Ohodnicki et al.. “Ultrafast Laser Enhanced Rayleigh Backscattering on Silica Fiber for Distributed Sensing under Harsh Environment,” in CLEO: Applications and Technology, May 2018, pp. ATh3P-4.

[17] A. Yan, S. Huang, S. Li, R. Chen, P. Ohodnicki, M. Buric, S. Lee, M. Li, and K. P. Chen, "Distributed Optical Fiber Sensors with Ultrafast Laser Enhanced Rayleigh Backscattering Profiles for Real-Time Monitoring of Solid Oxide Fuel Cell Operations," Sci. Rep., vol. 7, no. 1, pp. 9360, Aug. 2017.

[18] R. Taylor, C. Hnatovsky, and E. Simova, "Applications of femtosecond laser-induced self-organized planar nanocracks inside fused silica glass," Laser Photonics Rev., vol. 2, no. 2, pp. 26-46, Apr. 2008

[19] J. F. Bauters, M. J. R. Heck, D. John, D. Dai, M. Tien, J. S. Barton, A. Leinse, R. G. Heideman, D. J. Blumenthal, and J. E. Bowers, "Ultra-low-loss high-aspect-ratio Si 3 N 4 waveguides." Opt. Express, vol. 19, no. 4, pp. 3163-3174, Feb. 2011.

[20] S. Huang, M. Li, S. M. Garner, M. Li, and K. P. Chen, "Flexible photonic components in glass substrates," Opt. Express, vol. 23, no. 17, pp. 22532-22543, Aug. 2015.

[21] B. J. Soller, D. K. Gifford, M. S. Wolfe, and M. E. Froggatt, "High resolution optical frequency domain reflectometry for characterization of components and assemblies," Opt. Express, vol. 13, no. 2, pp. 666-674, Jan. 2005.

[22] Y. Liao, W. Pan, Y. Cui, L. Qiao, Y. Bellouard, K. Sugioka, and Y. Cheng, "Formation of in-volume nanogratings with sub-100-nm periods in glass by femtosecond laser irradiation," Opt. Lett., vol. 40, no. 15, pp. 3623-3626, Jul. 2015.

[23] M. Beresna, M. Gecevičius, and P. G. Kazansky, "Polarization sensitive elements fabricated by femtosecond laser nanostructuring of glass," Opt. Mat. Express, vol. 1, no. 4, pp. 783-795, Aug. 2011.

[24] S. Eaton, W. Chen, H. Zhang, R. Iyer, J. Li, M. L. Ng, S. Ho, J. S. Aitchison, and P. R. Herman, "Spectral loss characterization of femtosecond laser written waveguides in glass with

application to demultiplexing of 1300 and 1550 nm wavelengths," J. Lightwave Technol., vol. 27, no. 9, pp. 1079-1085, May. 2009.

[25] L. Tong, R. R. Gattass, I. Maxwell, J. B. Ashcom, and E. Mazur, "Optical loss measurements in femtosecond laser written waveguides in glass," Opt. Comm., vol. 259, no. 2, pp. 626-630, Mar. 2006.

[26] P. Lu, D. Grobnic, and S. J. Mihailov, "Characterization of the birefringence in fiber Bragg gratings fabricated with an ultrafast-infrared laser," J. Lightwave Technol., vol. 25, no. 3, pp. 779-786, Mar. 2007.

[27] L. A. Fernandes, J. R. Grenier, P. Marques, S. Aitchison, and P. R. Herman. "Strong birefringence tuning of optical waveguides with femtosecond laser irradiation of bulk fused silica and single mode fibers." J. Lightwave Technol., vol. 31, no. 22, pp. 3563-3569, Nov. 2013.

[28] M. Froggatt, and J. Moore, "High-spatial-resolution distributed strain measurement in optical fiber with Rayleigh scatter," Appl. Opt., vol. 37, no. 10, pp. 1735-1740, Apr. 1998.

[29] S. T. Kreger, A. K. Sang, D. K. Gifford, and M. E. Froggatt, "Distributed strain and temperature sensing in plastic optical fiber using Rayleigh scatter," In Fiber Optic Sensors and Applications VI, vol. 7316, pp. 73160A. SPIE, Apr. 2009.

[30] M. A. S. Zaghloul, M. Wang, S. Huang, C. Hnatovsky, D. Grobnic, S. Mihailov, M. Li et al, "Radiation resistant fiber Bragg grating in random air-line fibers for sensing applications in nuclear reactor cores," Opt. Express, vol. 26, no. 9, pp. 11775-11786, Apr. 2018.

[31] S. J. Mihailov, C. Hnatovsky, D. Grobnic, K. Chen, and M. Li, "Fabrication of bragg gratings in random air-line clad microstructured optical fiber," IEEE Photon. Technol. Lett., vol. 30, no. 2, pp. 209-212, Dec. 2017.